Alma Mater Studiorum – Università di Bologna

DOTTORATO DI RICERCA IN

MECCANICA E SCIENZE AVANZATE DELL'INGENERIA

Ciclo 31°

Settore Concorsuale: 09/A2

Settore Scientifico Disciplinare: ING-IND-13

On the Lifetime Characterization of Dielectric Elastomer Transducers

Presentata da: **Chen Yi**

Coordinatore Dottorato	Supervisore
Prof. Marco Carricato	**Prof. Rocco Vertechy**

Esame finale anno 2019

Abstract

Dielectric Elastomer Transducers (DETs) are deformable capacitors that are capable to transform electrical energy into mechanical energy and vice versa. DETs are generally considered as light, flexible structures with good energy density, and have been utilized in variety of applications as actuators, generators and sensors. The main component in a DET system is the compliant Dielectric Elastomer (DE) material, which is a highly elastic dielectric polymer. To verify the feasibility of DET applications, electromechanical properties of DE materials and reliability of DET systems should be thoroughly explored.

This thesis focused on the investigation of electromechanical properties of DE materials and lifetime characterization of DET specimens. Three DE materials have been considered for electromechanical characterization: THERABAND YELLOW 11726 styrenic rubber, OPPO BAND GREEN 8003 natural rubber and VHB 4905 acrylic elastomer. DET specimens based on two DE materials have been considered for lifetime characterization: THERABAND YELLOW 11726 as mentioned previously and WACKER ELASTOSIL® 2030, a commercialized silicone elastomer.

Electromechanical characterization has been conducted according to existing standards, while for lifetime characterization, a novel experimental setup and procedure have been proposed. This proposed methodology makes it possible to perform reliable and efficient lifetime experiments on standardized custom-prepared DET specimens under high voltage operating condition.

A series of tests have been conducted following the proposed methodologies and the obtained results have been collected and analyzed. In particular, comparison has been made between the three DE materials considering dielectric and mechanical behaviors. A Gent-Gent model has been found to be able to describe precisely the observed mechanical behavior of considered DE materials. Lifetime results on the styrenic DET specimens have shown, for the first time, how operating conditions and system configuration affect the lifetime behavior of DET systems. For silicone DET specimens, promising lifetime values (over 2 million operating cycles) have been observed under an operating condition with energy density larger than $300 J/kg$.

Contents

List of Figures

List of Tables

Chapter 1

Introduction

1.1 Dielectric Elastomer Transducer (DET) application

Dielectric elastomer transducer (DET) technology has become a popular topic since 1990s. DETs are basically electrostatic devices that can convert electrical energy into mechanical energy and vice versa, i.e. electromechanical transducers. The crucial components in a DET system are the dielectric elastomer (DE) materials. Some typical examples of DE materials are: acrylic elastomers [1], silicone elastomers [2], natural and styrene-based rubbers [3]. DE materials belong to polymer category, thus DETs are also referred as a type of Electroactive polymer (EAP) transducers. From the electrical point of view, DETs are essentially deformable capacitors which typically work under high voltage and low current (compatibly with the overall power output requirements).

Compared to other electromechanical transducers, DET are usually considered to possess advantages such as high compliance, large energy density, low cost, ease of manufacturing and integration, silent operation etc.

Currently, many research works have exploited the electro-mechanical coupling behavior of DETs in actuator, generator and sensor applications. In particular, possible actuator applications are as micro-fluidic pumps and valves [4], [5], loudspeakers [6], braille displays [7], tunable lenses [8], [9], soft actuators for robots interacting with humans and the environment [10], self-sensing actuators [11]–[14].

Possible generator applications are energy harvesters from human motion [15] as well as from natural resources, like wind energy [16] or ocean waves [17]–[20].

1.2 Motivation

To make a step forward from the DET demonstrators to products of practical value, there are still issues related to the DETs to be thoroughly explored.

In an on-going research project that is supported by Wave Energy Scotland (WES), a Power Take Off (PTO) device based on DETs has been developed for harvesting energy from ocean waves (reported in [21]). But the proposed wave energy harvester should endure a relatively long lifespan (typically from 5 to 25 years) with an acceptable level of performance (for instance, an energy density above 100 J/kg) to ensure practical viability and economic feasibility of the application. This consideration also holds for all DET applications, which requires a good understanding of the reliability and lifetime characteristics of DET systems working under their near-limit conditions.

During operation, the previously mentioned DET generator will suffer from cyclical electrical and mechanical loading due to the energy harvesting cycle, humidity, corrosion and shocks due to the harsh ocean environment. All these factors might influence the lifetime behavior of a DET system, which makes this topic very broad and difficult.

So far, the only existing evidence on the lifetime characterization of DET systems is reported in [22], where the lifetime characteristic of DETs based on acrylic elastomers has been studied. The results highlight that:

- DET systems with a variety of configurations (such as roll, expanding circle/square etc.) based on acrylic elastomer have been tested under different working conditions. Lifespans in the range of millions of working cycles have been observed in a number of specimens;
- Electrode formulation have considerable influence on the lifetime of DET systems: carbon black based electrode has shown longer lifetime than graphite fibril-loaded electrode;
- Humidity influences significantly the lifetime of the DET systems: a difference of more than 20 times has been observed between DET actuators working under dry and open-air conditions;
- The average lifetime is highly affected by the operating electric field level;
- Actuation strain for DET actuator seems to have a mild effect on the lifetime characteristics.

Though the results are impressive and interesting, the work [22] only considered DETs based on acrylic elastomer. Acrylic elastomer, though popular in the field, might not be optimal for DET applications. In fact, acrylic elastomer has in general larger viscoelasticity than other DE material such as silicone elastomer ([2]), hence the power loss and heat generation during the operation are relatively large. Viscoelasticity also lowers the dynamic response of the transducers. Lifetime characterization considering other DE material is thus important for a comprehensive comparison between the performance of different materials. In addition, in [22] the DET sample quantities were too small for certain tested conditions, the tested DET devices were also in different shapes and structures. Characterizing the lifetime behavior of DETs instead requires testing on standardized DET specimens.

In this work:

- Electromechanical characterizations on three typical DE materials (natural rubber, styrenic rubber and acrylic elastomer) have been performed and analyzed.
- Four test benches have been designed and implemented to perform lifetime characterization on the DET specimens. DET specimens based on two types of DE material (styrenic rubber and silicone elastomer) have been prepared and tested. Results have been collected and analyzed.

In particular, Chapter 2 introduces the basic working principles of DETs and presents some interesting applications in current research field; Chapter 3 discusses the general failure mechanisms and the stochastic procedure for studying the lifetime characteristics of polymers; Chapter 4 reports results of the electromechanical characterization on three typical DE materials: styrenic rubber, natural rubber and acrylic elastomer; Chapter 5 reports results of the lifetime characterization on DETs based on styrenic rubber and silicone elastomers.

Chapter 2

Introduction on Dielectric Elastomer Transducers (DETs) Applications

DETs have been utilized in many applications in innovated material research field. Their deformability offers new possibilities in designs of applications as actuators, generators and sensors. At present DET applications generally appear in forms different from each other in the aspect of geometry configurations, materials, functionalities etc. Hence universal rules or routines in designing and validating the DET applications are still under developing.

In this chapter, only basic DET working principles will be elaborated. In particular, we will focus on the relation between performance and operating conditions of DETs. After a brief introduction on principles of DETs (Section 2.1), notable applications of DETs working as generator, actuator and sensor will be introduced in Section 2.2, 2.3 and 2.4 respectively.

2.1 General working principles of DETs

To elaborate the operation principles of DET, a very basic configuration of DET is introduced as a simple example in Fig. 2.1. It is essentially a compliant plate capacitor with the key elements comprises:

- A thin membrane made of Dielectric Elastomer (DE) material
- Compliant electrodes applied to top and bottom of the DE membrane

Assume there is no resistance on the electrodes, no leakage current through the DE material and the DE material has a linear, isotropic and uniform dielectric properties, the considered system has a capacitance that can be expressed as,

$$C = \frac{\varepsilon_0 \varepsilon_r A}{z} \tag{2.1}$$

with A and z the area and the thickness of the DE membrane, ε_0 the vacuum permittivity and ε_r the relative permittivity of the DE material. When this DET system is charged via outer circuit, the electrical energy U_e held by the capacitor can be written as,

$$U_e = \frac{1}{2}\frac{Q^2}{C} = \frac{1}{2}CV^2 = \frac{1}{2}\varepsilon_0\varepsilon_r E^2 Vol \tag{2.2}$$

with Q the charge retained on the capacitor, V the applied voltage, E the electric field across the DE material and Vol the volume of the DE material ($Vol = Az$). DE materials are usually considered as incompressible, thus $Vol = Az = const.$.

The applied electric potential will generate stress within the DE material according to electrodynamic theory. The effective Maxwell stress inside the DE material can be deduced from an energy point of view, as introduced in [23]. Assume no electrical energy could enter or leave the capacitor via charge flowing through outer circuit, i.e. the constant charge condition, the mechanical work done by the effective Maxwell stress is equal to the loss of electrical energy stored in the capacitor. For an infinitesimal displacement in z direction, the energy balance equation can be written as (from Eq. 2.1, 2.2 and incompressible assumption),

$$\sigma_e A dz = -dU_e = -\frac{d}{dz}(U_e)dz = -\frac{d}{dz}\left(\frac{1}{2}\frac{Q^2 z^2}{\varepsilon_0\varepsilon_r Vol}\right)dz \tag{2.3}$$

Solving this equation for σ_e, the effective Maxwell stress along the z direction, we have,

$$\sigma_e = -\varepsilon_0\varepsilon_r E^2 \tag{2.4}$$

This expression is a well-known result in DET research field. The negative sign indicates that the Maxwell stress is opposite to the thickness direction, i.e. the stress will always try to compress the DE membrane.

Geometry of DET systems can be largely deformed due to the high compliance of DE materials. The variation on system geometry will change also the capacitance C according to Eq. 2.1, hence the stored electrical energy. The Maxwell stress will compress the system, increase the area A and shrink the thickness z. In this case the Maxwell stress does work to the ambient mechanisms that coupled with the system: the DET system is working in actuator mode. By applying additional stresses, system geometry might be contracted in area and thus increased in thickness due to incompressibility. This contraction will increase the capacitance C according to Eq. 2.1, so as the electrical energy stored in the system. In this case the geometry deformation is against the Maxwell stress and mechanical energy from outer mechanical sources is converted into electrical energy: the DET system is working in generator mode. As can be seen, in both cases the performance of energy conversion is directly related to the Maxwell stress. According to Eq. 2.4, the applied electric field level and the relative permittivity of DE material define generally the Maxwell stress, hence they are also directly related to the performance of DET actuators and generators. DE materials with large relative permittivity and high dielectric strength are thus preferred for DET applications. In particular, the dielectric strength has a quadratic effect in Eq. 2.4.

By adopting methods from capacitive sensing field, the capacitance of DET system can be measured by various of techniques. Based on the measured capacitance, the current geometry of the system can also be estimated through Eq. 2.1: the DET system can now work as sensors.

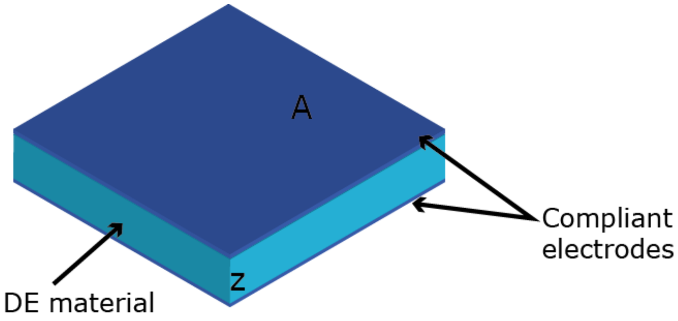

Figure 2.1. Basic DET configuration: a layer of DE material is sandwiched by two compliant electrodes.

2.2 DET generator

2.2.1 Basic working principle

In generator application, the DETs are usually working cyclically, with each cycle can be referred as an energy conversion cycle ([19]). Within each cycle, the DET system switches between stretched and contracted geometry states. During this procedure, the mechanical energy is transduced to electrical energy and then taken off from the system. The DET system will operate under both external mechanical input and electrical stress during the working cycle. To elaborate the correlation between the performance of DET generator and the applied electrical field, a simple example is introduced here as a square-shape DET generator with initial side length L and thickness z. The DET system is shown in Fig. 2.2.

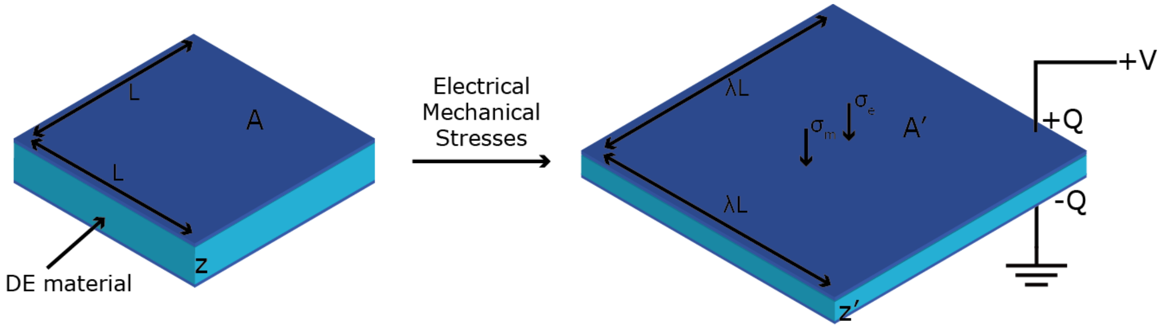

Figure 2.2. A square shape DET generator is compressed by both electrical and mechanical stresses, resulting an equi-biaxial stretching. The outer circuit provides an electric potential of V onto the DET and the DET system retains a charge of Q.

The DET generator is powered up by an outer circuit with voltage V and the transducer retains a charge of Q. Here we assume a simple uniaxial stress σ_m is externally applied to the system along the z direction. The geometry will be stretched equi-biaxially with a stretch ratio λ in x and y directions (in-plane). From the incompressibility assumption ($\lambda_x\lambda_y\lambda_z = 1$) the stretch ratio in the z direction is $\lambda_z = \frac{1}{\lambda^2}$, hence the current thickness of the system is $z' = \lambda_z z = \frac{z}{\lambda^2}$. In constant voltage case, the resultant Maxwell stress σ_e can be written as (based on Eq. 2.4),

$$\sigma_e = -\varepsilon_0\varepsilon_r\left(\frac{V}{z'}\right)^2 = -\varepsilon_0\varepsilon_r\left(\frac{V}{z}\right)^2\lambda^4 \tag{2.5}$$

The current capacitance C' of DET can be calculated as,

$$C' = \frac{\varepsilon_0\varepsilon_r A'}{z'} = \frac{\varepsilon_0\varepsilon_r\lambda^2 L^2}{\frac{z}{\lambda^2}} = \frac{\varepsilon_0\varepsilon_r L^2\lambda^4}{z} \tag{2.6}$$

The Q-V relationship now becomes,

$$Q = C'V = \frac{\varepsilon_0 \varepsilon_r L^2 \lambda^4}{z} V \tag{2.7}$$

For stationary scenario, the force balance equation can be expressed as,

$$\sigma_m + \sigma_e = \sigma_m - \varepsilon_0 \varepsilon_r \left(\frac{V}{z}\right)^2 \lambda^4 = \sigma_{DE}(S_z) \tag{2.8}$$

with $\sigma_{DE}(S_z)$ the strain-stress characteristics of the DE material along the z direction under simple extension, with the strain $S_z = \lambda_z - 1$. This stress can be viewed as a recovery stress by the elastomer itself to compensate the compression stresses.

For an ideal DET generator as shown above, the state can be completely described by Q, V, σ_m and λ ([24]). To illustrate the performance of an energy conversion cycle, a common way (as mentioned also in [24]) is to present a state of the DET generator as a point on Q-V plane or on λ-σ plane as shown in Fig. 2.3. For instance, when a DET system has its geometry fixed, i.e. its capacitance is fixed, the state set of the DET generator is a straight line passing the origin on Q-V plane. While geometry deformations might be difficult to be reflected on Q-V plane, they can be easily observed on λ-σ plane as stretch-stress curves.

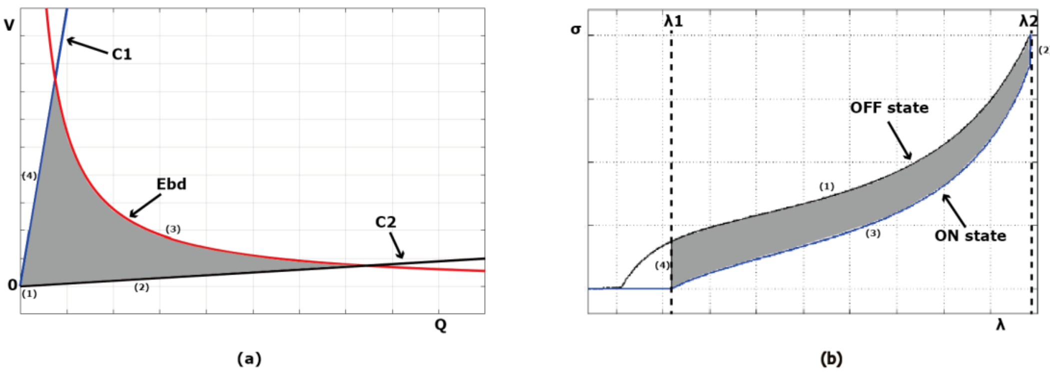

Figure 2.3. Example of a simple energy conversion cycle with maximum electric field control law plotted in (a) Q-V plane and in (b) λ-σ plane.

The range of state of a DET generator during the operation is limited by many factors. The most significant ones are the electrical breakdown field E_{bd}, the maximum principal stretch λ_{max} and the electromechanical instability of the DET configuration.

When the applied electric field reaches the dielectric strength E_{bd} of the material, electrical breakdown might occur in the DE material. During the electrical breakdown, conductive paths will form across the material, resulting short-circuit and dysfunctional of the DET system.

Assume the DE material has a fixed dielectric strength E_{bd}, from the electrical energy expression Eq. 2.2, the Q-V relationship is limited by the function,

$$VQ = 2U_e = \varepsilon_0 \varepsilon_r Vol E_{bd}^2 \tag{2.9}$$

which represents a hyperbola on the Q-V plane (an example is plotted in Fig. 2.3a). The permissible range for states is the area below this hyperbola curve. From [24], the dielectric strength is in fact correlated to the stretch (for example, in VHB DE material the dielectric strength increases when the applied stretch is increased), the actual curve might only be approximate to a hyperbola.

For maximum principal stretch λ_{max}, the simplest fracture criterion is the Kawabata's criterion [25], which postulates that rupture will not happen in the i-th principle direction if $\lambda_i < \lambda_{max}$ (for $i = 1,2,3$). According to Eq. 2.6, capacitance is dependent solely on the stretch λ. Hence λ_{max} is actually associated to a straight line that passes origin on Q-V plane, with a relatively small slope (the reciprocal of capacitance). The permissible range for states is the area above this line. On λ-σ plane, this limitation can be shown straightforwardly as $\lambda_2 < \lambda_{max}$, with λ_2 the largest stretch ratio that the DET generator will experience during an energy conversion cycle, as shown in Fig. 2.3b.

Since Maxwell stress will always try to compress the DE material, in constant voltage condition, decrease of thickness will increase the electric field across the DE material. This increased electric field will lead to an even larger Maxwell stress, which will compress further the DE material. At certain level of voltage, this procedure will lead to instability of the system.

Assume a linear material with a constant elastic modulus Y in z direction, the strain-stress characteristic $\sigma_{DE}(S_z)$ can be put as,

$$\sigma_{DE}(S_z) = YS_z \tag{2.10}$$

If there is no mechanical input applied to the system, Eq. 2.8 can be transformed as,

$$V = \sqrt{-\frac{z^2\lambda_z^2\sigma_{DE}(S_z)}{\epsilon_0\epsilon}} = \sqrt{-\frac{z^2\lambda_z^2Y(\lambda_z-1)}{\epsilon_0\epsilon}} = \sqrt{-\frac{z^2Y(1/\lambda^2-1)}{\lambda^4\epsilon_0\epsilon}} \tag{2.11}$$

which is referred as voltage-stretch curve in [26]. When $\frac{dV}{d\lambda}$ reaches zero, the voltage-stretch curve reaches a peak. If λ is continuously increasing, the curve will decrease accordingly. The decrease of voltage-stretch curve indicates that the DE material will not be able to compensate the Maxwell stress and shrink indefinitely. Hence this peak can be considered as the instability point and calculated (for λ_z) as,

$$\frac{dV}{d\lambda_z} = \sqrt{\frac{z^2Y}{\epsilon_0\epsilon}} \cdot \frac{2-3\lambda_z}{2\sqrt{-\lambda_z^2(\lambda_z-1)}} = 0 \tag{2.12}$$

in which the solution is simply $\lambda_z = \frac{2}{3}$. The strain S_z is equal to $\lambda_z - 1 = -\frac{1}{3}$, which is identical to the demonstrational result shown in [23]. $\lambda_z = \frac{2}{3}$ or $S_z = -\frac{1}{3}$ is only a theoretical instability point, under the assumptions that there is no external mechanical input and the material has linear strain-stress characteristic with constant modulus.

This so-called electromechanical instability (EMI) has been studied in the work [26]–[28], just to list a few. Common methods to avoid EMI include pre-stretching, calibrating DE material characteristic through fillers etc. In this work EMI is not considered since it is highly dependent on the DE material characteristic and is out of the scope of this thesis.

Limits introduced above constrain the state trajectory of DET generator during the energy conversion cycle. A simple control law of energy generation which maintains highest possible electric field is elaborated as an example here. This basic energy conversion cycle is composed of four phases of operations (as shown in Fig. 2.3):

(1) Starting from state with no applied electrical potential and charges (OFF state), the DET generator is stretched from initial stretch state λ_1 to λ_2 by external mechanical input. The capacitance of the DET generator is increased correspondingly from C_1 to C_2. This phase cannot be reflected on Q-V plane since all the related states locate within the origin point. On λ-σ plane this phase can be represented as the upper strain-stress curve.

(2) With the stretch λ_2 kept fixed, the DET generator is charged through outer circuit till the electric field reaches E_{bd} (close to the dielectric strength of the DE material). This phase locates as a straight line passing through origin with smaller slope on Q-V plane in Fig. 2.3a and as a vertical line on λ-σ plane in Fig. 2.3b.

(3) With the voltage controlled to maintain the electric field at E_{bd} (ON state), the DET generator is contracted in area and restored to the initial stretch λ_1. The generated electrical energy can be deduced from inspecting the infinitesimal variation on the electrical energy dU_e. According to Eq. 2.1, Eq. 2.2 and the incompressible assumption, dU_e can be calculated as (as introduced in [23]),

$$dU_e = \left(\frac{Q}{C}\right) dQ - 2U_e \left(\frac{1}{A}\right) dA \tag{2.12}$$

The first term $\left(\frac{Q}{C}\right) dQ = VdQ$ is just the electrical energy input from the outer circuit by the flowing-in of charges. The second term is the generated energy, or in other words the mechanical-transduced electrical energy. This generated energy is directly proportional to the U_e, the currently stored electrical energy by the DET. From Eq. 2.2, U_e is also directly related to the applied electric field. By maintaining the applied electric field as high as possible during this phase will indeed maximize the generated energy by the DET generator per cycle. This phase locates as the electric breakdown limitation hyperbola on Q-V plane and as the lower strain-stress curve on λ-E^2 plane from λ_2 to λ_1.

(4) With the deformation λ_1 kept fixed, the DET generator is discharged to zero. The DET generator can now perform another energy conversion cycle. This phase locates as a straight line passing the origin with larger slope on Q-V plane and as a vertical line on λ-σ plane.

After the finishing of one energy conversion cycle, the area enclosed by the state trajectory of the DET generator on the state plane is proportional to the generated electrical energy. Since state is limited by the electric breakdown and the rupture strength of the material, these two constraints are the significant factors that affect the efficiency of the DET generator.

2.2.2 Applications

DET generators generally have decent energy density. The following figures have been demonstrated in experimental laboratory tests: 173 J/kg for an inflating circular diaphragm DET made with a silicone elastomer dielectric layer undergoing bubble like deformation ([21]); 370 J/kg for a DET with similar geometry except the DE layer is made with a natural rubber dielectric ([3]); 780 J/kg for a planar circular DET made with an acrylic elastomer dielectric layer undergoing equi-biaxial expansion ([29]). High energy density, cheapness of DE materials and ease of manufacture characteristic of DET, all these advantages make DET generators good candidates for harvesting clean energy in large scale. As introduced previously, DET system generally prefers high voltage to maximize the performance, which is also in favor with power distribution system.

DET generators are also relatively insensitive to the operating frequency. From the previous elaboration, the operation of DET generator mainly depends on the strain and stress that applied to the system rather than the rate of the mechanical input, i.e. the DET generator usually have large dynamic range ([23]). This enables DET generator to harvest energy sources with irregular frequencies, which are common in renewable energy sources such as ocean waves and wind.

Energy harvester based on DET for harvesting ocean wave energy have been exploited in [17]–[19], [21], [29], [30]. The cyclic characteristic of the ocean wave well fits the operational principle of DET generator.

In particular, in [18], [30], DET generators with cylinder shape were designed to harvest the ocean wave energy. The proposed device has a hollowed cylinder chamber as the main body, with the top sealed by a bubble like DET layers and the bottom left opened. The device can work either as a buoy or as a stationary facility at the shore. The chamber is half-immersed in the ocean, with the bottom beneath and the top DET generator above the ocean surface. When the waves strike the device, the air pressure within the chamber will push the DET layer sealed on-top to inflate and deflate cyclically. The controlling circuit will perform the proper control law and charge take-off operation to harvest the energy.

In [17], the generator is composed of a chain of hollowed cylinder chambers with their side-walls composed of DET layers. By immersing totally underneath the ocean surface, this setup will be deformed cyclically by the ocean waves, so as each unit of DET layers along the chain.

In [19], the generator is composed of a four-bar linkage with DET layers constrained onto the links. The four-bar linkage is then connected additionally to an oscillating flap. With waves push onto the flap, the four-bar linkage is deformed in area and so as the DET layers.

Since DE materials are generally light and deformable, wearable devices that harvest energy from human activities are also proposed. A proof-of-principle example is shown in [23], with DET generators placed in the heels of shoes to collect energy from walking activities. Step-up converter is needed for DET for working as wearable devices.

2.3 DET actuator

2.3.1 Basic working principle

While in generator mode the DET is compressed by the external mechanical input in the OFF state (no electrical load applied), in actuator mode the DET is compressed by the Maxwell stress and hence in the On state.

Assume again the simple DET system as mentioned in Section 2.2. For small strain S_z, the stress-strain relationship can be approximated to a linear elastic characteristic as Eq. 2.10, thus the strain generated by the Maxwell stress can be written as (with Eq. 2.5),

$$S_z = \frac{\sigma_e}{Y} = -\frac{\varepsilon_0 \varepsilon_r}{Y}\left(\frac{V}{z}\right)^2 \lambda^4 = -\frac{\varepsilon_0 \varepsilon_r}{Y}\left(\frac{V}{z}\right)^2 \frac{1}{(1+S_z)^2} \tag{2.13}$$

Under the small-strain assumption, this expression can be further simplified as,

$$S_z = -\frac{\varepsilon_0 \varepsilon_r}{Y}\left(\frac{V}{z}\right)^2 = -\frac{\varepsilon_0 \varepsilon_r}{Y} E^2 \tag{2.14}$$

From the incompressible assumption, the relationship between the equi-biaxial strain $S = \lambda - 1$ and S_z is given by,

$$\lambda^2 \lambda_z = 1 = (1+S)^2(1+S_z) \tag{2.15}$$

Again, with the small strain assumption, the in-plane expansion S can be approximated as (with Taylor' expansion),

$$S = -\frac{1}{2} S_z \tag{2.16}$$

These results are under the assumption of small strain, but some natures of the DET actuators can be observed and qualitatively discussed. The electric field across the DE material determines the Maxwell stress, affects both the possible thrust and stroke of the actuator quadratically. Hence the performance of DET actuator is also directly related to the applied electric field.

DET actuators usually need additional mechanical frames to transform the in-plane or normal-to-plane stress and strain into usable thrust and stroke.

Some basic configurations of DET actuators are shown in Fig. 2.4 (from [23]).

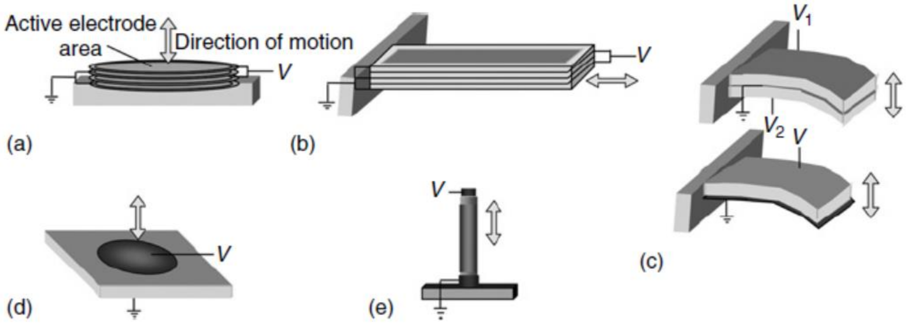

Figure 2.4. Basic DET actuator configurations (from [23]): (a) stack, (b) extender, (c) bimorph and unimorph bending beam actuators, (d) diaphragm and (e) tube.

These basic configurations use only the in-plane or normal-to-plane strain and stress of the DE materials to generate stroke and thrust. Some of the designs utilize stacking method for scaling up the effective stroke and thrust. For example, the stack configuration (2.4a) piles up DET layers to enhance the normal-to-plane strain and stress, while the extender (2.4b) and the tube configuration (2.4e) adopt similar methods but to enhance the in-plane strain and stress. Some of the designs make use of the deformability of the DE materials. For example, the bending beam (2.4c) and the diaphragm configuration (2.4d) permit out-of-plane deformation during operation, the tube configuration (2.4e) roll up a single long DET layer to implement stacking method for space saving. Although these designs are straightforward and relatively simple, they have shown the two major advantages of DET: scalability and deformability.

Advanced design in the mechanical frames in DET actuators will largely increase the stroke or thrust from the basic configurations. For example, mechanical frames with negative spring constant will perform work to the DET configuration during the operation to increase the effective stroke of the actuator.

2.3.2 Applications

Many DET actuators have been proposed in recent researches. DET actuators can improve the existing applications for space-saving, interactivity, conformability and inhibition of noise. DET actuators can also be essential in brand new designs of actuators.

Some examples of DET actuators improve the existing applications are:

In [5], DET-based micro gas valves were introduced. The setup utilizes stacked DET actuators that located at the inlets as the valve stem. Once activated, the shrink in thickness of DET layers will enable the gas to flow into the valve. DE materials usually work in silent, thus they might lower the noise and power loss for gas valve applications.

In [6], DET loudspeakers were proposed. The DET layers work both as actuator and sound-radiated medium. The deformability of DE materials enables the proposed loudspeakers to be placed to curved surface.

In [8], [9], DET tunable lenses were proposed. With clear fluid enclosed within transparent DET layers, the ensembled lenses will change the focal of length when proper commanding voltage is applied. In this way no additional mechanical mechanism is needed comparing to traditional tunable lenses. The transparency of certain DE materials enables this design, which also shows the diversity in the characteristics of different DE materials. Benefit from the polymer industry, a large variety of DE materials are available, and the material choice can be optimized for the considered applications.

Other applications that improved by DET actuator can also be found in [10] considering soft actuators for robots interacting with humans and the environment and in [7] considering braille displays.

For actuator designs that are originated from DET technology, artificial muscle is an interesting topic since the very beginning of DET history. Among many other electromechanical transducer technologies, DET is considered as one of the most similar to how human muscle behaves. A variety of artificial muscle designs were covered in [31]. For example, robot driven by rolled DET actuators, inchworm-type climbing robot with the body actuated by DET actuators.

Advanced designs on the mechanical frames of DET actuator are also of interest in current DET research field. In particular, DET actuator with bow-tie shape frame was introduced in [32]. The proposed frame with designed elastic characteristic forms a negative stiffness mechanism that help to increase the effective stroke of the plain rectangular DET actuator.

In [33], the proposed biasing frame mechanism combines both negative stiffness and linear elastic springs. The DET layer has a basic ring structure which will only have meaningful stroke in normal-to-plane direction with the help of biasing mechanisms. The negative stiffness part of the frame enables operation states to be bi-stable, lowers energy for maintaining stroke at large deformation.

In [34], flexible frames were proposed for DET actuator to perform out-of-plane deformation. The flexible frames can also be the medium between the soft DE material and the additional rigid frames for ease of attachment.

Other DET actuators with interesting mechanical frames can also be found in [35], [36].

2.4 DET sensor

2.4.1 Basic working principle

From Eq. 2.6, the capacitance of the DET is correlated to the current geometry. In constant charge condition, the relationship between the current voltage and the original voltage can be written as,

$$V' = \frac{Q}{C'} = \frac{Qz}{\varepsilon_0 \varepsilon_r L^2 \lambda^4} = \frac{V}{\lambda^4} \tag{2.17}$$

The current voltage will vary with the fourth power of the equi-biaxial stretch ratio. Since the DE materials generally allow larger deformation than most other deformable electromechanical materials, with proper settings the variance range in V' could be tuned to be sufficient for accurate measurement. Based on the variance on V', geometry information can be extracted. This approach is suitable for alternative mechanical input ([23]): for DC or very slow frequency mechanical input the variance in V' will be affected also by the current leakage of the DET and other factors, which will lead to inaccurate measurement.

An alternative way is to measure the capacitance of the DET directly. A common method is to construct a RC circuit with the DET as the capacitor and an additional measurement resistance R_m. This circuit behaves as a high-pass filter as shown in Fig. 2.5. Fig. 2.5 assumes both the capacitance C_{DET} and the electrode resistance R_{DET} are correlated to the system geometry. A sampling sinusoidal voltage signal V_s, with a frequency $f_s = \frac{\omega_s}{2\pi}$ higher than the cut-off frequency of the high-pass filter, will be applied across the RC circuit. The voltage V_m or the current I_m of resistance R_m will be measured and recorded.

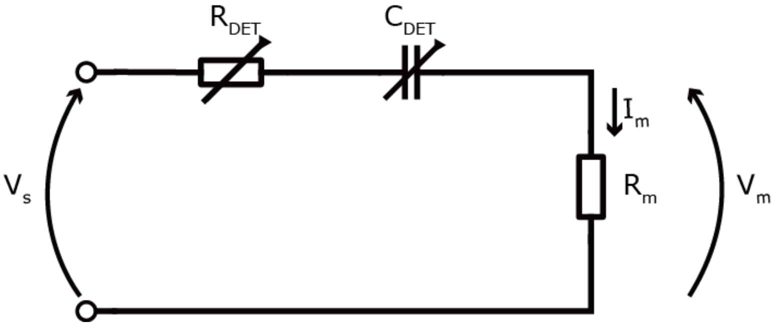

Figure 2.5. High-pass filter consist of DET system and measurement resistance.

From the measured V_m and I_m, many approaches can be utilized to estimate the capacitance of the DET. For example, as introduced in [37], the rms of I_m, $I_{m,rms}$ and the phase shift ϕ at the measurement frequency ω_s can be firstly extracted from the measured I_m. Then the Kirchhoff voltage equation can be written as,

$$\frac{V_s}{I_m} = R_{DET} + R_m - \frac{i}{\omega_s C_{DET}} \tag{2.18}$$

Here V_s and I_m are phasors of signals V_s and I_m. C_{DET} and R_{DET} can now be calculated as,

$$R_{DET} = Re\left(\frac{V_s}{I_m}\right) - R_m = \frac{V_{s,rms}}{I_{m,rms}} \cdot \cos\phi - R_m \tag{2.19}$$

$$C_{DET} = -\frac{1}{Im\left(\frac{V_s}{I_m}\right) \cdot \omega_s} = -\frac{1}{\frac{V_{s,rms}}{I_{m,rms}} \cdot \sin\phi \cdot \omega_s} \tag{2.20}$$

with $V_{s,rms}$ the rms value of the sampling signal.

Besides classic phasor analysis, online regression algorithm can also be utilized on the datums of V_m and I_m to estimate C_{DET} and R_{DET}.

By carefully tuning the sampling frequency and magnitude of V_s, the sampling signal might be superimposed onto commanding voltage signal without affecting the normal operation of DET systems. This enables the so-called self-sensing characteristic for the DETs, that the DET applications can operate without additional sensors. Self-sensing generally lowers the complexity of application structure or increases the reliability when additional sensors are available.

DET sensors are also benefit from the scalability and deformability of DE materials. Arrays or stacks of DET sensors can be manufactured to achieve multi-point sensing. The flexibility of DET structure makes it possible to place the DET sensors to irregular surfaces or hard-to-reach places with least interference to the monitored object. This is useful in bioengineering and many other application fields.

2.4.2 Applications

Attempts of making self-sensing DET devices have been made in recent researches. In [11] and [37], high frequency, small magnitude sampling voltage is superimposed onto commanding signals. The capacitance is estimated through basic phasor equations as introduced previously. In [14], similar sampling voltage is used, but regression algorithms such as Least Mean Squares and Recursive Least Square are utilized to estimate the parameters of the circuit.

Alternative measurement methods for system geometry are also available: in [38], the charging current is measured for determining the capacitance; in [39], resistance of the compliant electrodes is measured for geometry estimation.

Chapter 3

Theoretical Background for Fatigue in DET Systems

As can be seen in Chapter 2, DET generators are generally subjected to cyclically electrical and mechanical loading. Since DET systems usually have structures of layers rather than rotary structures, they need to return to initial condition from time to time for continuously operating. The same situation is also common in DET actuators: reciprocating motion is the major task for actuators working as system engines. As such, even if the applied electrical and mechanical conditions are well within the endurable range, DET applications are still susceptible to electro-mechanical fatigue and degradation during the operation. Understanding the lifetime and reliability behavior of DETs under cyclically loading is thus crucial for validating the feasibility of the technology.

The major factors that are likely to affect the lifetime of DET systems are:

- Mechanical and electrical loading history due to the normal operation of DET applications;
- DE material formulation, processing and pre-conditioning;
- DET configuration scale and size;
- Working environmental effects (for example, kinematic constraints due to electrode configuration, surrounding media, temperature, humidity, etc.);
- Dissipative effects due to the material constitutive response (viscoelasticity and electrical conductivity).

Since DE materials belong to polymer category, to establish approaches for characterizing lifetime and reliability of DET systems, existing practices for polymer technologies and research fields can be reasonable starting points and references. Lifetime characterizations in polymer industry regarding to either mechanical and electrical loading are well-established. In particular:

- For mechanical loading, a significant number of test methods and results exist on the fatigue life characterization of elastomeric specimens under cyclic loading conditions. Examples are the ASTM standards D430, D4482, D623, the ISO standards 6943, 466-1, 466-3, and papers [40]–[44];

- For electrical loading, the existing standards, such as ASTM D149 and IEC 60243, only cover the determination of the short-time dielectric strength of solid insulating materials subjected to direct current or alternative current with power frequencies (between 48 Hz and 62 Hz) conditions. However, established practices exist for the electrical degradation and breakdown characterization of polymers [45], mostly developed in power cable industry.

From [22] and our own experience, electrical degradation and breakdown seems to be the most probable mode that lead to the failure of DETs. In this study the investigation on the lifetime of DETs will consider electrical loading only. No mechanical loading is applied except the Maxwell stress and the constant pre-stretch ratio. Models, test plans and data analyses used in this study are developed in accordance with those currently employed in other fields of research and industry (mainly [45], [46]).

In this chapter, the electrical degradation and breakdown mechanisms for polymers are covered in Section 3.1. The adopted stochastic approach for handling the DET lifetime result is introduced in Section 3.2.

3.1 Electrical degradation and breakdown for polymer

Common DE materials such as natural rubber, silicone elastomer, acrylic elastomer all fall into category of polymers. Polymers are composed of long-chain macromolecules with repeating monomer units. They usually have excellent dielectric characteristic and controllable mechanical behavior. Hence they are widely used in power cable industry for electrical insulation, mechanical support etc.

The electrical degradation and breakdown processes in polymers can be defined as: the degradation procedure during which damage is accumulated within the material at the presence of electrical loading, and the final breakdown stage in which conducting channels are formed across the material. The electrical degradation and breakdown processes are complex procedures involve many physical and chemical mechanisms. In [45], the models of electrical degradation and breakdown mechanisms are divided into three categories: (1) low-level degradation models; (2) deterministic breakdown models and (3) stochastic models of the breakdown. However, the practical degradation and breakdown processes are indeed a combination of all the mechanisms, a detailed and accurate description on the process is generally difficult to achieve. Each of the category will be briefly introduced in the following sections.

3.1.1 Low-level degradation models for polymer

Degradation mechanisms that present within the polymer under low or even no electrical loading are introduced in this section. Degradation processes such as physical aging, chemical aging are not necessarily triggered by the electrical loading. But they can affect the probability of the electrical breakdown and can also be involved in electrical degradation procedures. Electrical degradation processes such as water treeing and partial discharging are initiated and intensified by the applied electrical loading.

Physical aging

The glass transition temperature T_g is the temperature below which the polymer will transform into glass-like state. Polymers such as elastomers have their glass transition temperature T_g below room temperature, thus elastomers are normally soft and flexible. Polymers such as polyvinyl chloride (PVC) have their glass transition temperature T_g above room temperature, thus they generally appear to be hard and rigid. The exact value of T_g depends on many factors, including the cooling or heating rate prior to the temperature. A more well-defined temperature level T_g' is at which the macroscopic viscosity and the relaxation rate of the polymer asymptotically approach infinity. T_g' is generally lower than T_g. Between T_g and T_g' is where the physical aging appears. In this temperature interval, the chain segmental motions of the polymer are inhibited and the returning to the equilibrium is slow down, thus the non-equilibrium state is now metastable. In this non-equilibrium state, slow structural relaxation via segmental motion is still allowed within the polymer and known as the physical aging. Physical aging can present above T_g of the bulk material: the amorphous regions adjacent to the crystalline lamella or the filler particles will have a higher local T_g than that of the rest amorphous body. Eventually the local mechanical stresses due to the structural relaxation (physical aging) will generate additional microvoids or increase the size of existing microvoids. Physical aging will also increase the number of interfaces between amorphous and chain-fold regions within the polymer. This leads to a greater density of traps and defects, and consequently an increase in local space charge concentrations. All these effects of physical aging will increase the propensity of the polymer to electrical degradation procedures. Hence the physical aging will indeed compromise the dielectric performance of the polymer.

Chemical aging

Chemical aging processes occur when polymer free radicals are formed due to certain initiating steps. The initiating steps could be thermal, oxidative, UV absorption, ionizing radiation, or even mechanical. Free radicals are very chemically active and will lead to chain scission or cross-linking network formation. Either way the dielectric behavior of polymer will be changed, which might lead to unexpected electrical degradation or breakdown processes.

Electrical aging

The main electrical aging processes include water trees, partial discharges and electrical trees. These aging processes can be triggered by electric field orders of magnitude lower than the dielectric strength of the polymer, thus they are still belonging to the low-level degradation models.

Water trees occur at relatively low field (lower than electrical trees), but water is essential for the process to origin and continue. Polymer material should be in contact with aqueous electrolyte for water trees to form. Water trees are generally visible with shape like tree branches. They can grow across the dielectric material without forming conducting path that leads to direct electrical breakdown, but the tree path can initiate electrical tree and thus degrade the insulation of the polymer.

Partial discharges occur in the gaseous contents enclosed by the microvoid within the polymer,. Since the gas enclosed within the voids usually have a permittivity lower than the surrounding polymer material, when electrical loading is applied, the electric field within the voids will be enhanced. When the applied electric field reaches certain threshold value, this enhanced field will ionize the gas. The carriers of the ionization might erode the compact wall of the voids, generate defects within the material. If the discharge persists, these defects are likely be the starting points for electrical trees or other degradation mechanisms. The critical electric field level depends on the size of microvoid, the gas pressure and the gaseous contents.

Electrical trees usually originate from the defects caused by partial discharge or other degradation processes. The tree branches are consisting of connected channels which are only weakly conductive. Thus, the forming and growing of electrical trees do not necessarily lead to immediate breakdown, but dielectric performance is definitely degraded. Hence electrical trees can still be considered as a degradation model.

3.1.2 Deterministic breakdown models for polymer

The deterministic electrical breakdown models will provide an exact critical electric field level based on operating conditions of the polymer, above which the breakdown will occur. These models can be categorized according to the processes that lead to the final breakdown stage. In [45], four such models have been introduced as:

Electric breakdown

Two types of electric breakdown are essential for polymer:

- Avalanche breakdown, which requires relatively high electric field level. In this case, when an electron with high enough energy collides with a bound electron, both electrons will be freed. With the help of the applied electric field, the two electrons can again be accelerated and achieve enough energy before next collisions. As this procedure continues, the number of carriers will increase exponentially and eventually cause irreversible damage to the polymer. This type of breakdown can be described by the required number of generations of ionizing collisions and level of applied electric field.
- Intrinsic breakdown, which happens when the rate of losing energy, from electrons to lattice in polymer via electron-photon scattering, reaches a critical value. When the energy cannot be completely absorbed by the lattice, the electrons will eventually acquire sufficient energy for the final breakdown. The crucial electric field level for intrinsic breakdown can be found by solving the balancing equation between the energy gaining and losing functions for electrons.

Thermal breakdown

When the polymer is electrically stressed, some leakage current will flow within the material and some electrical power will be dissipated through the polymer. If the heat input (either from electrical power dissipation or the ambient environment) exceed the heat loss during the operation, the temperature on the polymer will increase indefinitely. The increasing in temperature might lead to two types of electric breakdown:

- The high temperature permanently changes the physical properties of the polymer (for example melting), which might cause the dielectric strength lower than the applied electric field level and hence lead to electrical breakdown.
- The increase of temperature will increase also the conductivity of the polymer: high temperature will free more bound electrons within the material. The current will be enhanced due to the increase of the conductivity and so as the Joule heating. The Joule heating will further increase the temperature and thus the conductivity. This positive feedback procedure is the so-called ‘thermal runaway’ and will eventually lead to material breakdown.

Electromechanical breakdown

This mechanism is similar to DET electromechanical instability introduced in Section 2.2.1: the polymer cannot compensate the electrostatic stress due to the electrical loading and eventually lead to electrical or mechanical breakdown.

Partial discharge breakdown

Partial discharge has been introduced in section 3.1.1 as degradation model. The same procedures can lead to directly breakdown of the polymer. The level at which partial discharge breakdown occurs is also dependent on the gaseous content, polymer material and the microvoid configuration.

For deterministic degradation and breakdown mechanisms, given the operation condition and material characteristic, the critical condition is defined by the corresponding models. This is generally not the case in practical applications where lifespan and dielectric strength cannot be predicted exactly. Hence they are better described through stochastic approach with corresponding probability distribution models. In this thesis we will focus on the stochastic approach for characterizing the reliability and lifetime behavior of DET with methods adopting from the polymer industry. The detailed theoretical background on the stochastic approach will be introduced in next section.

3.2 Stochastic approach for DET lifetime

3.2.1 Basic introduction on reliability statistics

For polymer dielectric under electrical loading, it is impossible to predict the exact lifetime before electrical breakdown or the breakdown electric field level for certain operating condition, as mentioned previously. But if the lifetime probability distribution under electrical loading are known information, the failure probability at certain lifetime can be estimated within degree of confidence. To explore the lifetime distribution and probability, stochastic approach is thus necessary. Stochastic approach generally involves testing a large set of identical specimens under the same electrical loading. Each specimen will fail at a random different time that is likely to obey certain lifetime probability distribution model.

An intuitive way to present the result of this kind of tests is plotting the obtained lifetime results as histogram. In this histogram, the vertical dimension represents the number of failed specimens, while the horizontal dimension represents the lifetime of the specimens. Thus, each bar in the histogram shows number of failed specimens (height) within a time interval (width). Fig. 3.1 shows an example of lifetime results for 60 specimens presented as histogram figures (reproduced from [45]). Fig. 3.1a, shows a direct histogram of the testing result, and in Fig. 3.1b shows a histogram for cumulative number of specimens failed before the time intervals. The fraction of failed specimens is shown at the right axis.

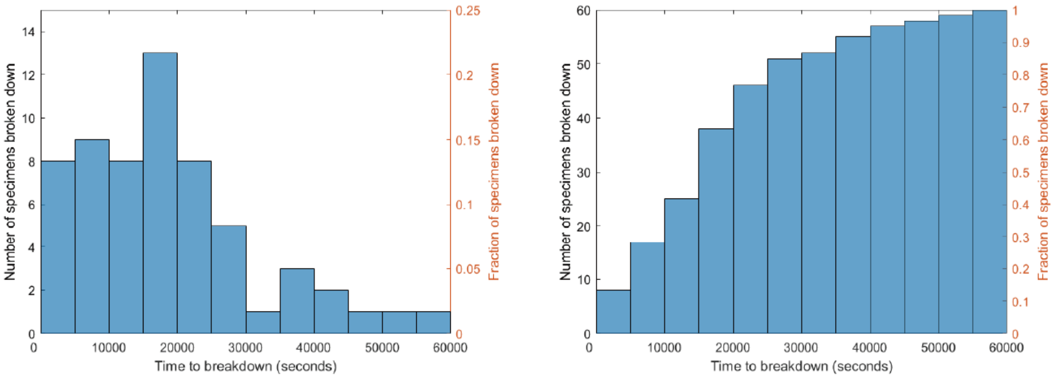

(a) (b)

Figure 3.1. (a) Histogram representation of results for constant-stress tests, the height of each vertical bar represents number of specimens or the proportion of the total number of specimens failed within the corresponding time interval; (b) cumulative histogram representation of the same set of results (reproduced from [45]).

If the test is consisting of infinite number of specimens, the histogram will have infinite number of bars with infinitesimal width, i.e. the histogram becomes a smooth curve, as shown in Fig. 3.2. The fraction of the failed specimen in these two histograms will now correspond to the probability density and the cumulative probability of the failure. Thus, the two curves indeed represent, accordingly, the probability density function (PDF) $f(t)$ and the cumulative probability function (CDF) $F(t)$ of failure.

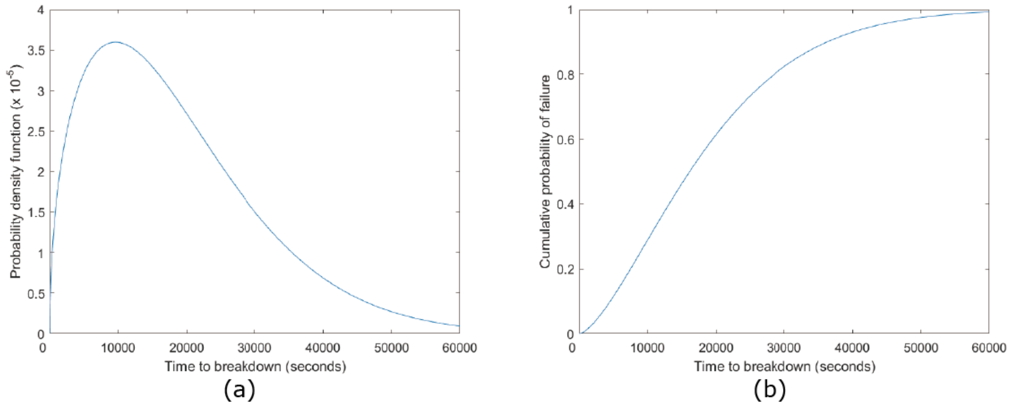

Figure 3.2. Examples of (a) probability density function and (b) cumulative distribution function of failure based on the same result set in Figure 3.1 (reproduced from [45]).

The CDF $F(t)$ is the probability of a specimen failed before time t, i.e.

$$F(t) = Prob(t_b \leq t) \tag{3.1}$$

with t_b the time-to-breakdown for the specimen. $F(t)$ will always start at the origin and tend to 1 with $t \to \infty$, under the general assumption that no specimen is broken at the start of the test and eventually all specimens will fail in finite time. The relationship between CDF $F(t)$ and the PDF $f(t)$ is given by,

$$F(t) = \int_0^t f(\tau) d\tau \tag{3.2}$$

since $f(t)$ can be interpreted as $f(t)dt = Prob(t \leq t_b < t + dt)$ for $dt \to 0$. Thus $F(t)$ equals geometrically to the area under $f(t)$ curve between times 0 and t. The inverse relationship is also useful, which is:

$$f(t) = \frac{dF(t)}{dt} \tag{3.3}$$

The reliability function or the survivor function $R(t)$ is the probability that a specimen will not fail before the time t, hence it is the complement of $F(t)$:

$$R(t) = Prob(t_b > t) = 1 - F(t) = \int_t^{\infty} f(\tau)d\tau \tag{3.4}$$

The hazard function (HF) $h(t)$ represents the instantaneous rate of failure at time t for a specimen that has already survived so far, namely:

$$h(t) = \lim_{\delta t \to 0} \frac{Prob(t \leq t_b < t + \delta t | t_b \geq t)}{\delta t} = \frac{f(t)}{R(t)} \tag{3.5}$$

The reliability function and the hazard function for the previous mentioned example (from [45]) are reproduced in Fig. 3.3.

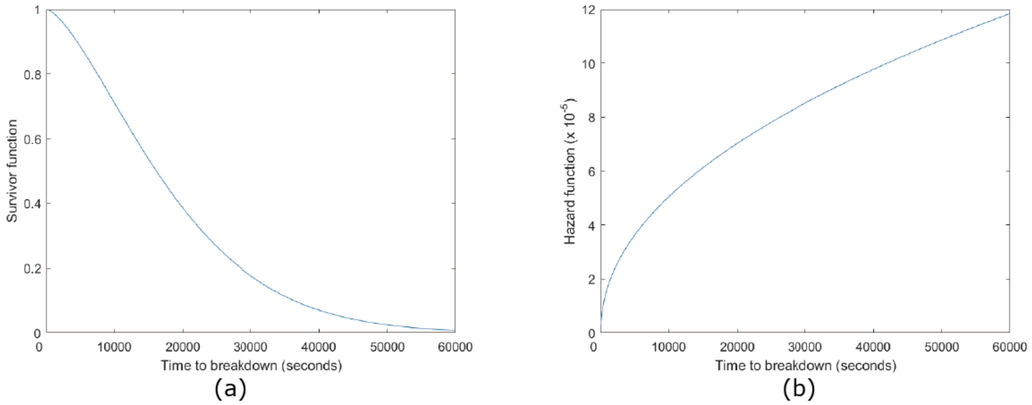

Figure 3.3. Examples of (a) reliability function and (b) hazard function based on the same result set in Fig. 3.1 (reproduced from [45]).

From Eq. 3.3 and Eq. 3.4, $f(t) = -\frac{dR(t)}{dt}$. Together with Eq. 3.5, we can get a differential equation:

$$\frac{dR(t)}{dt} = -f(t) = R(t)h(t) \tag{3.6}$$

which has a solution with the form $R(t) = \exp\left[-\int_0^t h(\tau)d\tau\right]$. The relationship between $h(t)$ and $F(t)$ can now be written as,

$$F(t) = 1 - R(t) = 1 - \exp\left[-\int_0^t h(\tau)d\tau\right] \tag{3.7}$$

This expression emphasizes the effect of time-varying hazard function on the CDF. In the next section, time-varying parameters (such as the applied electric field level) can be accounted based on this expression.

3.2.2 Weibull distribution model

Basic introduction on Weibull distribution

Weibull distribution is widely used in reliability statistics for assessing the lifetime of specimens, and is also suggested in [45] to characterize the lifetime behavior of polymer dielectric under electrical loading. The CDF $F(t)$, the PDF $f(t)$ and the reliability function $R(t)$ of a two-parameter Weibull distribution are defined as,

$$F(t) = 1 - \exp\left[-\left(\frac{t}{\alpha}\right)^{\beta}\right] \tag{3.8}$$

$$f(t) = \left(\frac{\beta}{\alpha}\right)\left(\frac{t}{\alpha}\right)^{\beta-1} \exp\left[-\left(\frac{t}{\alpha}\right)^{\beta}\right] \tag{3.9}$$

$$R(t) = \exp\left[-\left(\frac{t}{\alpha}\right)^{\beta}\right] \tag{3.10}$$

in which the distribution model can be determined with two parameters: α the scale parameter and β the shape parameter. From Eq. 3.5, the hazard function of Weibull distribution has the form

$$h(t) = \frac{f(t)}{R(t)} = \left(\frac{\beta}{\alpha}\right)\left(\frac{t}{\alpha}\right)^{\beta-1} \tag{3.11}$$

In Weibull distribution, parameter α is also known as characteristic lifetime since at $t = \alpha$, $F(\alpha) = 63.21\%$. As the name indicated, parameter β determines the shape of the CDF and PDF curves, so as the hazard function. The effects of β on CDF, PDF and HF curves are shown in Fig. 3.4 (reproduced from [45]).

For CDF (Fig. 3.4a), the increase of β will lower the probability for specimen to fail at the early stage, but in the meantime increase the failure probability at the late stage. β will not change the characteristic lifetime (which is defined by α) of the distribution, all curves intersect at the characteristic lifetime with percentile of 63.21%.

For PDF (Fig. 3.4b), β dramatically changes the shape of the PDF curves. For $\beta \leq 1$, the PDF decreases monotonically. For $\beta > 1$, the PDF is peaked with the probability density at the peak increases along with the increasing of β. Since integral of the PDF from 0 to ∞ should maintain unity, the PDF becomes narrower. The peak also approaches the characteristic lifetime α when $\beta \to \infty$. In other words, as β increases, the lifespans of specimens will have a smaller deviation.

For HF (Fig. 3.4c), the function curve is highly dependent on the values of β. Specifically:

- $\beta < 1$ indicates a HF that decreases over time, which is typical of early-life failures;
- $\beta = 1$ indicates a constant HF, which means that there is no damage accumulation. The CDF now becomes an exponential distribution as $F(t) = 1 - \exp\left(-\frac{t}{\alpha}\right)$;
- $\beta > 1$ indicates a HF that increases over time, which provides a strong evidence of damage accumulation that is typical of wear-out failures. Very large values of β (i.e., $\beta > 5$) are typically distinctive of bad system design or extreme testing conditions.

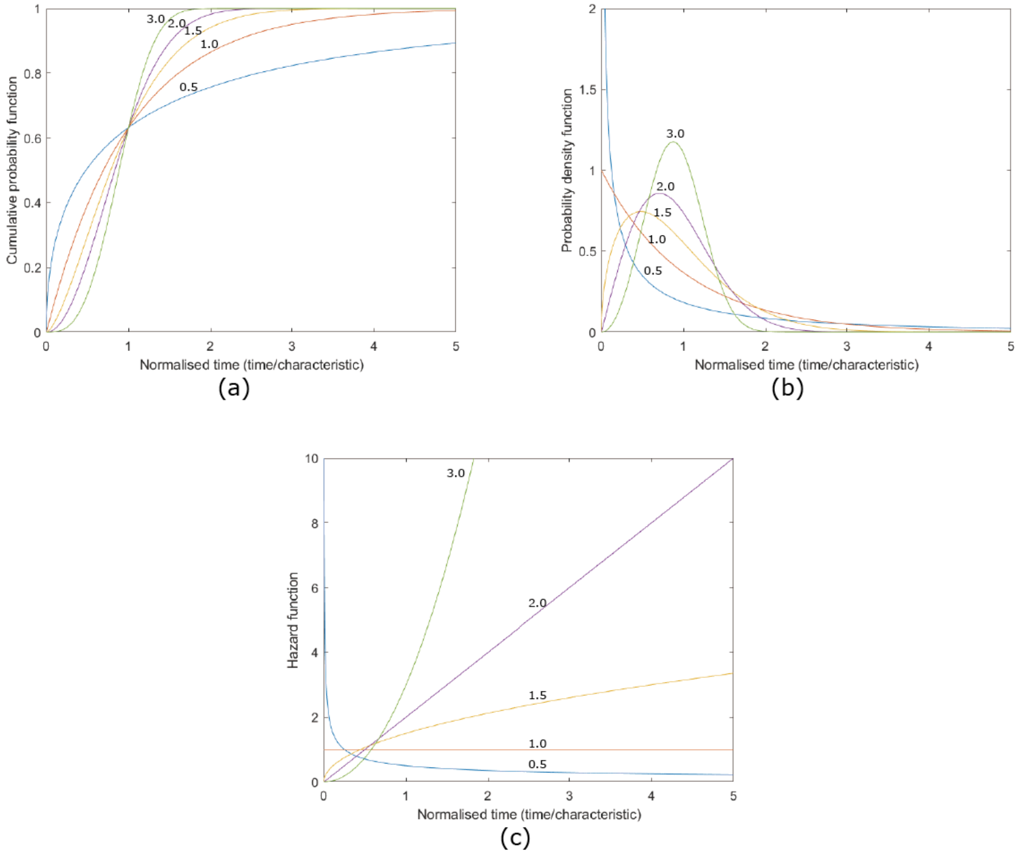

(a) (b)

(c)

Figure 3.4. Comparison of different values of β on (a) CDF, (b) PDF and (c) hazard function with normalized time axis (reproduced from [45]).

Two-parameter Weibull distribution is a particular case from the general three-parameter Weibull distribution, which has the CDF defined as,

$$F(t) = \begin{cases} 1 - \exp\left[-\left(\frac{t - t_{th}}{\alpha}\right)^{\beta}\right], & t \geq t_{th} \\ 0, & t < t_{th} \end{cases} \tag{3.12}$$

with t_{th} an inception time or threshold value below which the specimen will not fail. t_{th} also serves as a location parameter as it shifts the distribution along the time axis by the value of itself. In this thesis we mainly focus on the two-parameter Weibull distribution as initial assumption for DET lifetime distribution.

Incorporating effect of electrical loading into Weibull distribution

The following reasoning has also been reported in [47], [48].

As suggested in [45], the effect of electric field can be incorporated into Weibull distribution model through the characteristic lifetime α. In [45], two empirical laws are introduced: the inverse power law and the exponential law.

The inverse power law relates α and the applied electric field level E as,

$$\alpha(E) = \frac{\exp(a_1)}{E^{a_2}} \tag{3.13}$$

with a_1 and a_2 new parameters to be determined by numerical fitting of experiment results.

The exponential law relates α and the applied electric field level E as,

$$\alpha(E) = a_1 \exp\left(\frac{a_2}{E}\right) \tag{3.14}$$

Both laws make a common assumption that the increase of the electrical loading will decrease the characteristic lifetime, hence parameter $a_2 > 0$. This thesis will consider the inverse power law as initial assumption for DET lifetime distribution, for the general reason that this relationship can be easily incorporated into Weibull distribution model. In inverse power law, parameter a_2 reflects how the electric field affects the distribution, i.e. relates to the breakdown mechanism of the testing condition. While a_1 works as a scale parameter which converts the electric field level to the range of lifetime. Additional parameter E_{th} can be included in as,

$$\alpha(E) = \begin{cases} \dfrac{\exp(a_1)}{(E - E_{th})^{a_2}}, & E \geq E_{th} \\ \infty, & E < E_{th} \end{cases}$$

with E_{th} the threshold electric field, below which the specimens will not fail. As a first assumption, we have considered $E_{th} = 0$. With a time-varying electric field $E(t)$, the inverse power law can be incorporated into the hazard function (Eq. 3.11) of Weibull distribution model as,

$$h(t) = \frac{\beta}{\exp(a_1\beta)} t^{\beta-1} [E(t)]^{\beta a_2} \tag{3.15}$$

Substitute Eq. 3.15 into Eq. 3.7, the CDF can now be written as,

$$F(E,t) = 1 - \exp\left\{-\int_0^t \frac{\beta}{\exp(a_1\beta)} \tau^{\beta-1} [E(\tau)]^{\beta a_2}\, d\tau\right\} \tag{3.16}$$

The operation of DET generator, as introduced in Chapter 2, involves applying electrical stress when DET configuration is expanded and withdrawing when it is contracted. Hence the operating electrical loading on the DET generator can be roughly approximated by a square-wave electric field waveform. In this thesis square-wave electric field waveform with 50% duty cycle is considered as the test condition.

The considered periods of electrical loading are relatively small compared to the estimated lifespan of the DET system (DET generators usually work in 0.1-10Hz while the expected lifetime should be of months or even years). During each operating cycle, the DET system will also experience charging and discharging phases in addition to normal constant electric loading. Hence, the lifetime characteristic might be better described in terms of number of energy conversion cycles. In this way, the performance of a DET generator can also be directly related to the lifetime. Hence, we postulate that the CDF incorporated with square-wave electric field signal can be written as:

$$F(N) = 1 - \exp\left[-\left(\frac{N}{N_c}\right)^{\beta}\right] \tag{3.17}$$

which describes the probability of failure for a DET specimen during the Nth operating cycle. N_c is now called the characteristic lifetime cycles. If the effect of electrical loading needs to be incorporated, N_c can share the same expression of $\alpha(E)$ as $N_c = \alpha(E) = \frac{\exp(a_1)}{E^{a_2}}$, in which E now represents the magnitude of the square-wave electrical field waveform. The associated parameters might be affected additionally by the frequency and shape of the square-wave electrical stress now.

The effect of frequency might be deduced through Eq. 3.16 which deals with elapsed time. For square wave electric field waveform with 50% duty cycle, the CDF can be written as,

$$\begin{aligned} F(E,t) &= 1-\exp\left[\sum_{n=0}^{N-1} -\int_{nT}^{nT+\frac{1}{2}T} \frac{\beta}{\exp(a_1\beta)}\tau^{\beta-1}E^{\beta a_2}\,d\tau\right] \\ &= 1-\exp\left\{\sum_{n=0}^{N-1} -\frac{E^{\beta a_2}}{\exp(a_1\beta)}\left[\left(nT+\frac{1}{2}T\right)^{\beta}-(nT)^{\beta}\right]\right\} \end{aligned} \tag{3.18}$$

with T the period of the square wave waveform. No simple explicit form is available for this expression, but since generally $N \gg \frac{1}{2}$, a rough approximation can be calculated using integral with rectangle method and the first order Taylor approximation:

$$F(E,t) \approx 1-\exp\left[-\frac{E^{\beta a_2}T^{\beta}N^{\beta}}{2\exp(a_1\beta)}\right] = 1-\exp\left\{-\left[\frac{TN}{2^{\frac{1}{\beta}}\alpha(E)}\right]^{\beta}\right\} \tag{3.19}$$

which compared with Eq. 3.17 will have $N_c = \frac{2^{1/\beta}\alpha(E)}{T}$. This expression indicates that the larger the period, the shorter the characteristic lifetime cycles since the material is electrically stressed longer with larger period. Here, this conclusion is not considered at first: Eq. 3.16 is based on continuous constant electric field that might not be suitable for square-wave electric field waveforms, also the expression is a result of many approximations. Hence here we will use Eq. 3.17 as a primary distribution model and the dependence of N_c on the frequency of square-wave waveform will be explored through experiments.

In Eq. 3.17, assumption has been made that the shape parameter β will not be affected by the applied electric field. But from [45], parameter β might indeed vary for different levels of electric field since different levels might trigger different failure mechanisms. To include this possible dependency of β on the electric stress, here we postulate an expression of β as,

$$\beta = a_3 - a_4 \log E \tag{3.20}$$

with additional parameters a_3 and a_4. This proposed expression is simply stating that β is linearly dependent on the logarithm of the electric stress. Logarithm of the stress has been chosen since Weibull analysis is more conveniently assessed in logarithmic scale.

After estimating the parameters N_c and β, the Mean-Cycle-To-Failure (MCTF) can be calculated as the mean value of the Weibull distribution,

$$MCTF = N_c \cdot \Gamma(1 + 1/\beta) \tag{3.21}$$

Eq. 3.17 and Eq. 3.21 alone can be fitted with experimental data without considering the effect of electrical loading to validate how test conditions other than electric field level (such as electric field frequency, kinematic constraints and DET device size) affect the lifetime distribution.

Weibull parameters estimation and confidence analysis

In previous section, parameters a_1, a_2, a_3, and a_4 (or N_c, β neglecting effect of electrical loading) needed to be estimated for defining the model. A generally accepted method for estimating the Weibull parameters is the Maximum Likelihood Estimation (MLE) method.

As introduced in [46], The MLE method is aiming to find the parameters that maximize the joint likelihood function. For lifetime characterization, a likelihood function represents how likely a lifetime result set would be observed, if the lifetime indeed follows the distribution model defined by certain parameters. Assume each specimen’s lifetime is independent and identically distributed, the joint likelihood function will be the product of likelihood functions for all the obtained results, thus can be presents as a function $L(\boldsymbol{t};\boldsymbol{\theta}) = \prod_i f(t_i,\boldsymbol{\theta})$, with $\boldsymbol{t}$ the obtained lifetime result vector and $\boldsymbol{\theta}$ the parameter vector. Joint likelihood function is generally logarithmized as the sample log-likelihood function with the form $\mathcal{L}(\boldsymbol{t};\boldsymbol{\theta}) = \ln[L(\boldsymbol{t};\boldsymbol{\theta})]$. The MLE method can now be interpreted as: given sample vector $\boldsymbol{t}$ and the proposed distribution model, finding the estimated parameter vector $\widehat{\boldsymbol{\theta}}$ that maximize the sample log-likelihood function $\mathcal{L}(\boldsymbol{t};\boldsymbol{\theta})$.

General optimization tools, such as *fmincon* function from MATLAB© Optimization Toolbox, can be easily utilized to solve this kind of problems. *fmincon* function finds the minimum of an objective function under given constraints, thus the negative of $\mathcal{L}(\boldsymbol{N};\boldsymbol{\theta})$ can be used as the objective function. Additional constraints have been made as $N_c > 0$ and $1 \leq \beta \leq 5$, to prevent the identification of distributions that have failure rate decreases over time or with excessive accelerated failure.

From [46], if the number of samples is large and the given distribution models satisfy certain regularity conditions, parameter set $\hat{\boldsymbol{\theta}}$ estimated through MLE method converges in distribution to a normal distribution. This means that the joint sampling distribution of $\hat{\boldsymbol{\theta}}$ converges to a multivariate normal distribution with means as the true parameter $\boldsymbol{\theta}_0$. Most numerical optimization tools provide the approximated Hessian of the objective function at the found optimal vector $\hat{\boldsymbol{\theta}}$. Hessian is the matrix of second derivative of the objective function, and can also be used to estimate the covariance matrix for the estimated parameter vector $\hat{\boldsymbol{\theta}}$. Based on the normal asymptotic behavior of MLE method and the estimated covariance matrix, the two-sided $100\gamma\%$ confidence interval can be approximated on the estimated parameters or on functions that depend on the parameters.

In this work, parameters a_1, a_2, a_3, and a_4 or N_c, β have been estimated through MLE method. The two-sided 95% confidence intervals for parameters, lifetime under certain percentile and MCTF under certain electric field level are also estimated.

Weibull distribution graphical presentation

Weibull probability paper is a common way to present the obtained result and is intuitive for validating how well the Weibull distribution model fits the obtained result. Weibull probability paper has non-linear scale on the two axes:

- The vertical axis shows the cumulative probability. The scale is $\log_{10}[-\ln(1-P)]$ with P the cumulative probabilities of the sample result;
- The horizontal axis shows the observed lifetime. The scale is $\log_{10}(t)$.

To plot the result data points onto the Weibull probability paper, the cumulative probabilities P for the obtained results need to be estimated. A good and simple approximation on P is suggested in IEC 62539. Assume n specimens with observed lifetime have been acquired through testing under identical conditions. Specimens need firstly to be sorted from lowest to largest according to the observed lifetime, then a rank $i = 1, \ldots, n$ is assigned to each specimen according to the sorted order. The cumulative probability for the ith specimen can now be estimated as,

$$P(i,n) = \frac{i - 0.44}{n + 0.25} \times 100\% \tag{3.22}$$

When plotted on the Weibull probability paper, the two-parameter Weibull distribution model Eq. 3.17 can be transformed as,

$$\log_{10}[-\ln(1 - F)] = \beta \log_{10} N - \beta \log_{10} N_c \tag{3.23}$$

This expression represents a straight line on Weibull probability paper. Thus, the observed lifetimes will scatter along this straight line if the lifetime distribution model indeed follows the two-parameter Weibull model. Parameters N_c and β represent the offset (as the location of 63.19% percentile) and the slope of the straight line.

Presenting the results on the Weibull probability paper will also reflect the characteristics of other distribution. For three-parameter Weibull distribution, the line will be curved towards $-\infty$ along vertical axis at around the lifetime threshold t_{th} in Eq. 3.12. In certain cases, the life distribution following two-parameter Weibull model might have time-varying shape parameter β, for example the specimen might have $\beta < 1$ at early stage indicating a decreasing failure rate at the beginning of operation and have $\beta > 1$ later on for damage cumulating failure rate. This kind of distribution is the so-called multiplicatively-mixed two-parameter Weibull distribution ([45]) and on the Weibull probability paper the distribution is consist of two straight lines with different slopes in different lifetime regions. Examples of standard two-parameter, three-parameter and multiplicatively-mixed two-parameter Weibull distribution are plotted in Fig. 3.5.

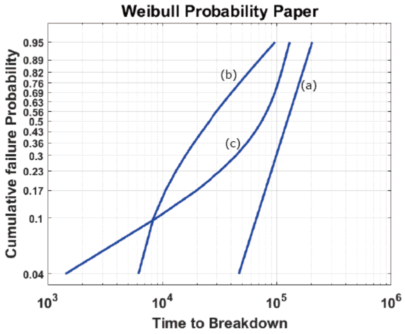

Figure 3.5. Different types of Weibull distribution model plotted on the Weibull probability paper, in particular: (a) two-parameter Weibull model; (b) three-parameter Weibull model; (c) multiplicatively-mixed two-parameter Weibull model (reproduced from [45]).

But generally, without enough observed data points, the curviness of distribution line on Weibull probability paper is difficult to be observed and validated.

The two-sided $100\gamma\%$ confidence interval of time to breakdown for certain percentile will form two curves that sandwich the estimated straight line of Weibull distribution. These two curves can be used to validate the reliability of the estimation.

Size scaling

In practical applications, specimens usually have sizes larger than those tested under laboratory condition. In order to apply the distribution model (obtained from tests) to practical situation, a simple and straight-forward method has been suggested in [45] and IEC 62539. Assume specimens with experimental sizes that are capable to capture sufficient characteristics of the material, specimens with bigger sizes can be considered as plain multiplicity of specimens with experimental size. The reliability probability of larger sample can now be expressed as the product of reliability probabilities for multiple smaller samples. Let the scale ratio D defined as $\frac{Application\ size}{Experimental\ size}$, based on Eq. 3.17 and the reliability function Eq. 3.12, the joint reliability can be calculated as,

$$R_{application} = R_{experimental}^{D} = \exp\left[-D\left(\frac{N}{\widehat{N_c}}\right)^{\widehat{\beta}}\right] \tag{3.24}$$

From this expression, the scaling of size will not affect the shape parameter $\hat{\beta}$ but only reduce the characteristic life cycle $\widehat{N_c}$ to $\frac{\widehat{N_c}}{D^{\frac{1}{\hat{\beta}}}}$. In practice specimens with larger sizes might be affected by different failure mechanisms, thus Eq. 3.24 needs to be verified through experiments.

Chapter 4

Electromechanical Characterization on DE Materials

Before conducting the lifetime characterization, electromechanical characterization has been performed on three typical DE materials to compare their capabilities in DET applications. The three considered DE materials are:

- Styrenic rubber (THERABAND YELLOW 11726), which will also be used in the lifetime characterization experiments;
- Natural rubber (OPPO BAND GREEN 8003);
- Double sensitive acrylic tape (VHB 4905 by 3M).

The thickness of specimens based on these three DE membranes are firstly measured. Then the dielectric strength, electrical conductivity, dielectric constant and mechanical response characteristics will be measured accordingly following the proposed procedures. The experimental set-ups and procedures are introduced in Section 4.1, the results for electrical characterization are reported in Section 4.2 and the results for mechanical response characterization are reported in Section 4.3.

4.1 Experimental set-ups and procedures

This section describes the experimental set-ups and procedures that have been used for determining the electromechanical properties of the three considered DE membranes.

For each DE membrane under investigation, the different characterization tests have been conducted on the same batch of material.

Specimens of the THERABAND YELLOW 11726 and OPPO BAND GREEN 8003 materials are prepared from the virgin band as is provided by the manufacturer. Specimens of the VHB 4905 material are prepared by first laminating (thereby, gluing) three virgin pieces of tape one on top of the other to obtain a three-layered membrane. This has been done for the following two reasons: 1) in practical DET applications, the VHB 4905 is frequently used in the form of laminates made by two/three layers of the base material [49]; 2) to make the initial working thickness of the VHB 4905 specimen similar to the initial working thicknesses of THERABAND YELLOW 11726 and OPPO BAND GREEN 8003 specimens.

Every experiment has been conducted in a laboratory environment, with a temperature of around 25 °C and a relative humidity of around 60%. Although the electromechanical properties of DEs are known to be affected by temperature, humidity and other environmental factors, these effects are not considered in this work.

4.1.1 Measurement of membrane thickness

Film thickness has been measured via a high-accuracy CCD laser displacement sensor (Keyence LK-G152). As shown in Fig. 4.1, tests are performed with the DE membrane specimen interposed between a base flat circular plate and a calibrated disc (made of brass, $50mm$ in diameter and $10mm$ in height).

In the set-up, the laser is kept fixed and is used to measure the distance of the same central point of the calibrated disc both in presence and in absence of the DE material under test. Membrane thickness is then estimated as the difference between these two measures. Correctness and repeatability are verified by performing the measurements five times on the same specimen and by checking that the acquired values do not differ by more than three per cent; then, the average value is taken as the membrane thickness estimate, t.

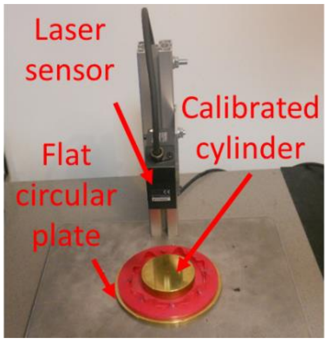

Figure 4.1. Set-up for membrane thickness measurement.

Although the use of a calibrated cylinder does not make it possible to measure the membrane thickness locally, the set-up considered here enables to reduce the errors due to imperfect contact between DE membrane and base plate, as well as to imperfect light reflection by the DE membrane (that is likely to be different from a material to one another due to different specimen thickness, roughness and colour). For the considered laser sensor and DE materials, these two issues made indeed difficult to obtain consistent results with the laser profilometry method suggested in [23].

4.1.2 Measurement of membrane dielectric strength

Dielectric strength measurement is performed with unequal cylindrical metallic electrodes with a set-up similar to those suggested in the standards IEC 60243-1 and ASTM D149 for thin films and laminates.

As shown in Fig. 4.2, a cylinder with dimension $25mm$ in both diameter and height is used as the high voltage electrode, whereas a cylinder with dimension $150mm$ in diameter and $10mm$ in height is used as the ground electrode. Both cylinders are made of brass and with the edges rounded to give a radius of $3mm$; they are arranged coaxially within $2mm$. The cylinder surfaces that are in contact with the membrane are polished and free from irregularities resulting from previous testing. To insure safety and to limit current dispersions though the surrounding air, the HV electrode is fully embedded in a plastic cylindrical receptacle (constituted by two parts made in Delrin®) that closes onto the DE membrane specimen. This protects the HV electrode from the user touch and interrupts the air path to the ground electrode. To limit the exposed metal surface, the lower half of the ground electrode is embedded in a Delrin® frame.

As for the power, control and measurement electronics: 1) the electric potential difference is provided to the unequal electrodes via a HV DC/DC converter (Untravolt 40A24-P30-C); 2) the connection between HV converter and electrodes is made with double-insulated HV cables; 3) input voltage is commanded to the HV supply either manually or automatically via a signal generator (ISO-TECH GFG 2004); 4) the electric potential difference commanded and generated by the HV supply are logged automatically to a PC via a USB-based oscilloscope (PicoScope 2202). This set-up enables to test DE membrane specimens with maximum electric potential difference selectable in the range from 0 to $40kV$, and to obtain breakdown voltage (and thus, dielectric strength) measurements with a resolution equalling 0.8% of the selected full scale.

For each specimen under test, electric potential difference is applied between the electrodes according to a short-time (rapid-rise) test; that is: voltage is raised from zero at a uniform rate until breakdown occurs, with the rate of rise chosen among 0.5 kV/s, 2 kV/s and 5 kV/s to guarantee the breakdown to occur between $10s$ and $20s$. After rupture, the breakdown voltage, V_{BD}, is extracted from the acquired data and the dielectric strength of the tested specimen is estimated as $E_{BD} = \frac{V_{BD}}{t}$.

To assess any dependency of dielectric strength on strain ([24]), each of the considered materials is here tested at different levels of equi-biaxial deformation.

Since dielectric breakdown in polymers is known to be a stochastic process as introduced in Chapter 3, seven specimens are tested for each material and level of deformation.

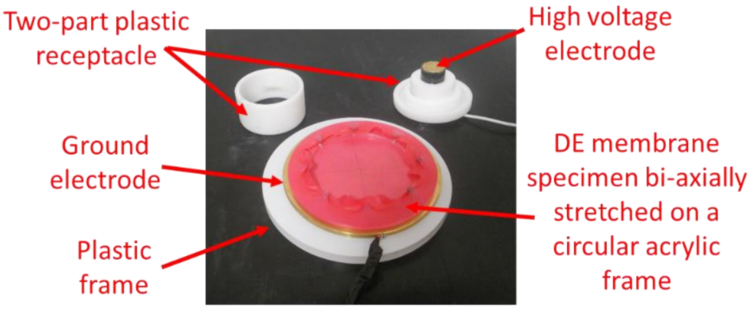

Figure 4.2. Electrode set-up for membrane dielectric strength measurement.

Differently from [23], unequal cylindrical electrodes have been preferred here to hemispherical (or spherical) and plate electrodes in order to test on larger volumes of materials, which typically provides more conservative and repeatable values that are closer to those experienced in practical applications. Differently from the IEC 60243-1 and ASTM D149 standards, the ground electrode of the unequal cylinders set-up is chosen larger than the suggested value ($150mm$ vs $75mm$) so as to support over their entire area DE membrane specimens that are stretched onto circular frames. This is important since each of the considered materials is here tested at different levels of equi-biaxial deformation in order to assess any dependency of dielectric strength on strain ([24]).

4.1.3 Measurement of membrane electrical conductivity

Volume conductivity measurement is performed on the electrode set-up shown in Fig. 4.3 which comprises: 1) the DE membrane under test; 2) an outer plastic frame made of two identical

Delrin® rings, each featuring $130mm$ internal diameter, $155mm$ external diameter and $3mm$ thickness, which is used to keep the DE membrane in a pre-stretched state at opposite sides; 3) two identical circular carbon grease (MG Chemicals 846) electrodes with $80mm$ diameter that are reported on the opposite sides of the DE membrane after pre-stretch; 4) an inner plastic frame made of two identical Delrin® rings, each featuring $80mm$ internal diameter, $120mm$ external diameter and $3mm$ thickness, which is used to confine the carbon grease electrodes within the prescribed $80mm$ diameter; 5) two copper strips for electrical instrumentation connection that are placed at opposite sides in contact with the respective carbon grease electrode and bonded to the inner ring; 6) two insulation layers made of an acrylic tape (VHB 4905 by 3M) disposed at opposite sides (also embedding the wires of the electrical instrumentation) which are used to minimize as much as possible spurious resistance paths (both in air and over the surfaces of DE membrane and frames) from HV to ground electrodes as well as to protect the HV electrode from the user touch. The same acrylic tape is also used at the interfaces of the Delrin® rings (of both inner and outer frames) with the DE membrane to promote adhesion ad insulation.

Electrical conductivity is measured at high voltage by connecting the sample electrodes to the same power, control and measurement electronics described in Section 4.1.2 with the addition of a pico-amperometer (Keithley 6485 Picoammeter) that is placed between the ground of DE membrane specimen and the ground of the HV power amplifier. A $1M\Omega$ resistor is also connected in series to prevent damage by current or voltage surges in case of electric breakdown of the DE specimen. This set up enables to measure leakage currents across the DE specimen up to $20mA$ (although usually employed in the range from $20\mu A$ to $0.1nA$).

For each specimen under test, electric potential difference is applied step-by-step, with electric field increments of about $10MV/m$ and a hold-time of about 60 s for proper material electrification (namely, for the current to settle after its asymptotic decay due to dielectric absorption and the sweep of mobile ions to the electrodes). At the completion of the test, the steady state values of the current attained at the end of each step, $I_L(E)$, are extracted and the electrical conductivity at a given level of applied electric field, E, is estimated as $\kappa(E) = \frac{I_L(E)}{AE}$, A being the electrode area.

To assess repeatability, tests are performed on three nominally identical specimens of the same membrane. The results are then used to compute mean value and standard deviation.

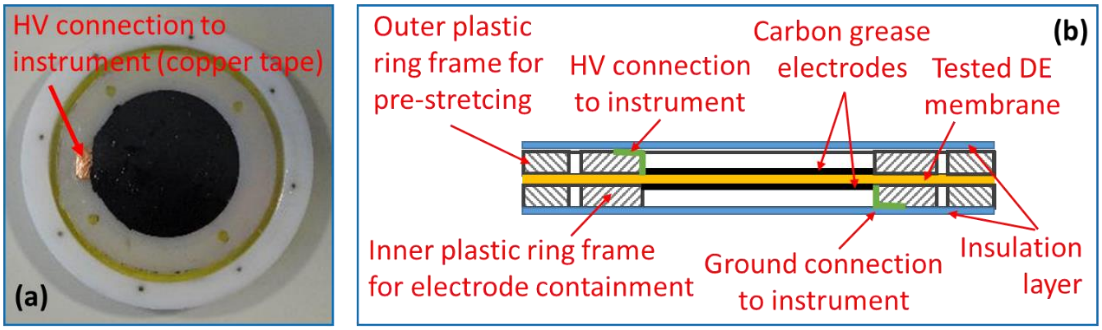

Figure 4.3. Electrode set-up for membrane dielectric constant measurement.

In this study, carbon grease electrodes are used in place of other electrode systems, like those suggested in the standard ASTM D257, for the following reasons: 1) they are expected to provide electrical property values that are closer to those experienced in many practical investigations, since carbon grease is the most employed material for the development of DETs based on the commercial elastomer films investigated here; 2) sprayed and evaporated metal electrodes do not adhere satisfactorily to the styrenic rubber membrane; 3) metal foil electrodes are not adequate for thin membranes like those considered here; 4) rigid metallic electrodes cannot get into intimate contact with the DE membrane under test and, thus, perform worse in all parameter estimations that involve the division of a measured quantity by the specimen area; 5) carbon grease enable easier and faster preparation of large quantities of specimens.

Worth to be mentioned: the considered set-up only uses two electrodes. That is, it does not comprise a third guard electrode which is suggested in the standard ASTM D257 to intercept all stray currents that may introduce measurement errors. Here, the guard electrode has been omitted since two insulation layers already exist in the set-up which brake almost any undesired path of conduction between HV electrode and ground electrode (see Fig. 4.3).

4.1.4 Measurement of membrane dielectric constant

Dielectric constant measurement is performed on the same electrode set-up shown in Fig. 4.3 with an LCR bridge (Hameg Instruments LCR meter HM 8118) connected to the specimen electrodes in place of the other electronics equipment described previously. This set-up enables the measurement of capacitance values in the range from $0.01pF$ to $100mF$, with test frequency, alternate current signal level and bias voltage selectable in the ranges from $20Hz$ to $200kHz$, from $50mV_{RMS}$ to $1.5V_{RMS}$, and from $0V_{DC}$ to $5V_{DC}$, respectively.

Each specimen is tested with the LCR meter at $20Hz$ with a $5V_{DC}$ biased alternate current signal having $1.5V_{RMS}$ root-mean-square magnitude. Once stabilized, the capacitance reading, C, of the instrument is taken and the relative dielectric constant of the DE membrane, ε_r, is estimated as $\varepsilon_r = \frac{Ct}{A\varepsilon_0}$, ε_0 being the vacuum permittivity ($\varepsilon_0 = 8.8541 \cdot 10^{-12} F/m$).

To assess any dependency of dielectric constant on strain, each of the considered materials is here tested at different levels of equi-biaxial deformation.

To assess repeatability, measurements are performed on three nominally identical specimens for each testing condition (material and level of stretch). The results are then used to compute mean value and standard deviation.

Worth to be mentioned:

- As done for conductivity measurement, carbon grease electrodes have been preferred here to other electrode systems, like those suggested in the standard ASTM D150 and in [23]. The reasons are the same as the ones provided in Section 4.1.3.
- In evaluating DE membrane capacitance value, no correction factor for the stray field at the edge has been applied; in fact, for the large diameter electrodes employed in the set-up, the ratio of fringing capacitance (estimated as per standard ASTM D150) and measured capacitance is always less than two percent for any of the tested specimens.

4.1.5 Measurement of membrane stress-strain response

Though in this work the dielectric characteristic and the associated effect on the lifetime is of major concern, mechanical characterization has also been performed to compare the considered materials comprehensively. The mechanical response of the considered DE materials is determined by testing transversally pre-stretched pure-shear specimens with a commercial tensile stage (Galdabini SUN 500). As shown in Fig. 4.4, the adopted pure-shear specimens feature a longitudinal length in the unstretched state equal to $10mm$ and a transversal length in the clamped state equal to $200mm$ (where longitudinal and transversal respectively mean parallel and normal to the motion direction imposed by the tensile stage).

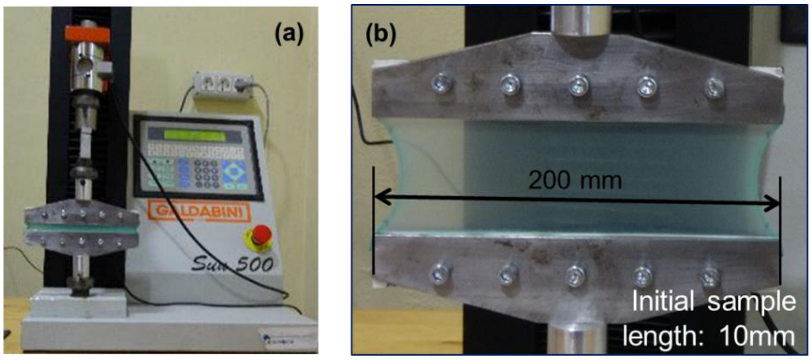

Figure 4.4. Set-up for membrane stress-strain response measurement.

In this study, each specimen under tests is cycled 10 times between the same deformation limits to remove Mullins effect, which disappear between the sixth and the seventh cycle for the considered materials. The last loading-unloading cycle is then taken as the stabilized response of the specimen.

To investigate strain-rate dependencies of the mechanical response, each specimen is tested at the following five different strain-rates: $0.004s^{-1}$, $0.08s^{-1}$, $0.4s^{-1}$, $0.8s^{-1}$ and $1.2s^{-1}$.

To investigate dependencies of the mechanical response on the applied strain level, each specimen is also tested at two different deformation amplitudes:

- Large Stroke: the maximum deformation level is set at the 90% of the elongation at break limit of the considered material, whereas the minimum deformation level is set as the value at null stress for the cycle performed at a strain rate of $0.08s^{-1}$..
- Intermediate Stroke: the strain amplitude is decreased so as to get the most effective response from the material.

As compared to the procedure suggested in [50], here the pure-shear specimens of each of the considered materials are pre-strained in the transversal direction to a value, λ_p, which is close to that used in practical applications. Moreover, a larger ratio of height to width (20 vs 10) is employed to obtain results that better approximate the response of ideal pure-shear specimens, especially at the larger levels of longitudinal deformation.

4.2 Electrical characterization results

This section reports the results obtained by testing the three considered commercial DE membranes with the set-ups and procedures described in the previous sections.

4.2.1 Measurement of membrane thickness

Measurement of membrane thickness, t, provided the following outcomes:

- A mean value of $293\mu m$ with a standard deviation of $5.46\mu m$ for the styrenic rubber band THERABAND YELLOW 11726;
- A mean value of $224\mu m$ with a standard deviation of $3.85\mu m$ for the natural rubber band OPPO BAND GREEN 8003;
- A mean value of $1492\ \mu m$ with a standard deviation of $15.96\mu m$ for the double sensitive acrylic tape VHB 4905.

Since the VHB 4905 is sticky and provided with a native paper liner, thickness estimation for this material has been performed with the same procedure described in Section 4.1.1, but in the following indirect manner: 1) the thickness of the specimen is measured without removing the liner; 2) the liner is removed from the specimen and its thickness measured; 3) specimen thickness is then obtained as the difference of these two measures.

4.2.2 Measurement of membrane dielectric strength

The experimental results of the dielectric strength tests conducted on the considered DE membranes are reported in Fig. 4.5-4.7 with circle markers. In particular:

- Fig. 4.5 reports the electrical breakdown data acquired on the THERABAND YELLOW 11726 membrane tested at the following three levels of equi-biaxial stretch: $\lambda = 1, 2.04, 3.12$.
- Fig. 4.6 reports the electrical breakdown data acquired on the OPPO BAND GREEN 8003 membrane tested at the following five levels of equi-biaxial stretch $\lambda = 1, 1.5, 2, 2.5, 3$.
- Fig. 4.7 reports the electrical breakdown data acquired on the VHB 4905 membrane tested at the following four levels of equi-biaxial stretch $\lambda = 2, 3, 4, 5$.

As shown, identical specimens subjected to the same testing condition (type of material and level of strain) fail at different values of applied electric field, with the spread of the breakdown data increasing significantly with the level of applied equi-biaxial stretch. The spread of the breakdown data is quite similar for the THERABAND YELLOW 11726 and the OPPO BAND GREEN 8003, and smaller for the VHB 4905.

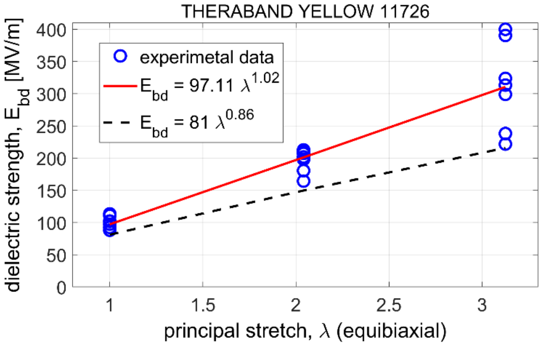

Figure 4.5. Dielectric strength vs stretch correlation for THERABAND YELLOW 11726: experimental data (circles); power law fitting of mean values (red solid line); 90 % reliability power law estimate (black dashed line).

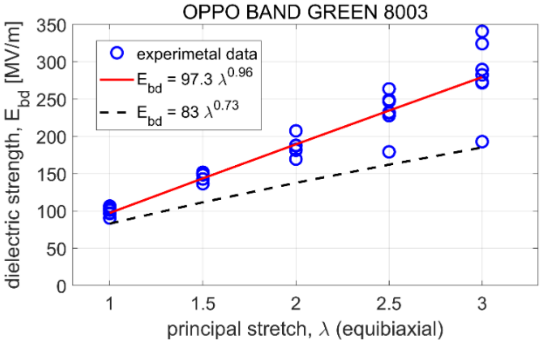

Figure 4.6. Dielectric strength vs stretch correlation for OPPO BAND GREEN 8003: experimental data (circles); power law fitting of mean values (red solid line); 90 % reliability power law estimate (black dashed line).

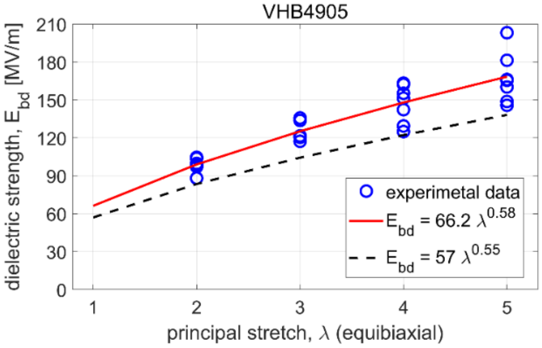

Figure 4.7. Dielectric strength vs stretch correlation VHB 4905: experimental data (circles); power law fitting of experimental data (red solid line); 90 % reliability power law estimate (black dashed line).

Despite the increasing spread of the acquired data, breakdown strength resistance of every material is shown to improve markedly with strain. To quantify this increase, the followings have been determined and reported for each material in the respective figures:

- Fitting of the experimental data with a power-law in the form $E_{BD} = E_0 \cdot \lambda^r$ (where E_0 and r are material parameters, see [24]), plotted with a solid red line, which represents the mean dielectric strength of the considered material;
- the lower-bound power-law, having the same form $\underline{E_{BD}} = \underline{E_0} \cdot \lambda^{\underline{r}}$ (where $\underline{E_0}$ and $\underline{r}$ are material parameters) and plotted with a dashed black line, which represents a limiting threshold not to be exceeded if one wants to guarantee a probability of failure of less than 10% (that is, a reliability higher than 90%, IEC 62539).

The fitted results are presented in Table 4.1 as,

Property	THERABAND^{TM} YELLOW 11726	OPPO BAND^{TM} GREEN 8003	VHB^{TM} 4905
Unstretched dielectric strength:			
E_0 (average) [MV/m]	97.1	97.3	66.2
$\underline{E_0}$ (90% reliability) [MV/m]	81	83	57
Strengthening exponent:			
r (average)	1.02	0.96	0.58
$\underline{r}$ (90% reliability)	0.86	0.73	0.55

Table 4.1. Fitted parameters for dielectric strength based on measured data on the three considered DE membranes.

The presented results highlight the following:

- THERABAND YELLOW 11726 and OPPO BAND GREEN 8003 behave quite similarly (the respective parameters E_0, r, $\underline{E_0}$ and $\underline{r}$ are indeed very close), with the former performing slightly better;
- VHB 4905 is the material with worst dielectric strength resistance.

The considered styrenic and natural rubber membranes have a similar dielectric strength resistance only if specimens do not come into contact with water. In fact, while immersion into water causes a significant reduction in dielectric strength for the OPPO BAND 8003, only a minor variation in the response occurs in the THERABAND YELLOW 11726. This is shown in Fig. 4.8, which reports the breakdown data for unstretched membranes that were immersed into water for two days and then tested in the following conditions:

- Wet state (red circle markers), where the samples have been dried with a towel for a few minutes and left for 1 hour at room temperature;
- Dried state (blue diamond markers), where the samples have been dried in an oven at 40°C for 2 hours.

As it can be seen, in wet state the spread of the breakdown data increases and its average shifts downward; with the spread and shift being larger for the OPPO BAND 8003. This reduction is however only temporary; upon drying, both materials indeed regain an average dielectric strength higher than $90MV/m$ (though to an average value of around $93MV/m$ that is slightly lower than those reported in Table 4.1 for specimens that did not get in contact with water). As a possible reason, the described effect could be due to the water adsorption/permeability of natural rubber is larger than styrenic rubber.

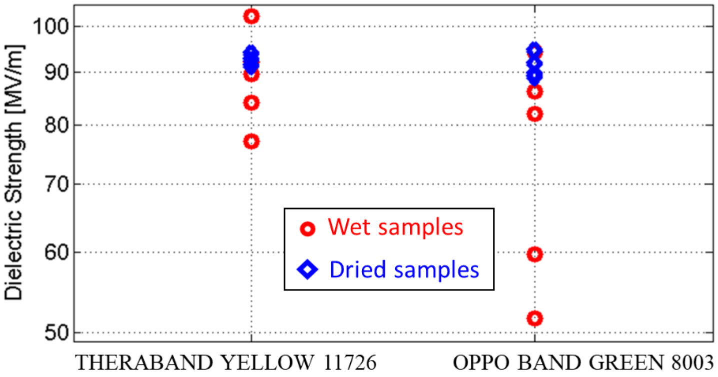

Figure 4.8. Dielectric strength for wet (red circle markers) and dried (blue diamond markers) specimens: THERABAND YELLOW 11726 (data on the left) vs OPPO BAND GREEN 8003.

As compared to other results existing in the literature, the findings obtained here are in line with those described in [3] and [51], which report $E_0 = 97\ MV/m$ and $r = 0.99$ for the OPPO BAND GREEN 8003 and $E_0 = 69\ MV/m$ and $r = 0.54$ for the VHB 4910 (a tape that has the same formulation of the VHB 4905 and that is just twice in thickness) for experimental data acquired with stamp electrodes embedded in epoxy resin.

4.2.3 Measurement of membrane electrical conductivity

The experimental results of the electrical conductivity tests performed on the considered DE membranes are reported in Fig. 4.9-4.11. In particular:

- Fig. 4.9 and 4.10 report the electrical conductivity data respectively acquired on the THERABAND YELLOW 11726 membrane and on the OPPO BAND GREEN 8003 membrane tested at an equi-biaxial stretch of $\lambda = 2$ (thus, with thicknesses of about $73\mu m$ and $56\mu m$, respectively).
- Fig. 4.11 reports the electrical conductivity data respectively acquired on the VHB 4905 membrane 8003 membrane tested at an equi-biaxial stretch of $\lambda = 5$ (thus, with thicknesses of about $59\mu m$).

These levels of stretch have been selected since they are in the middle of the operational range that is expected for the considered membranes and to provide specimens with comparable thickness (thus, geometrically similar) despite different in material.

In the figures, blue dot markers represent the average over the measurements performed on the three specimens tested at the same conditions, with the blue error bar representing their standard deviation.

As shown, average and standard deviation values of increase with the applied electric field irrespective of the considered material.

To quantify the dependency of conductivity with applied electrical solicitation, fitting of the experimental data with an exponential-law in the form $\kappa = \kappa_0 e^{\frac{E}{E_B}}$ (where κ_0 and E_B are the material parameters to be determined, see [52]) has been performed. For each material, curve fits are plotted in the respective figures with a dashed red line, whereas fitted parameters are reported in Table 4.2 for comparison.

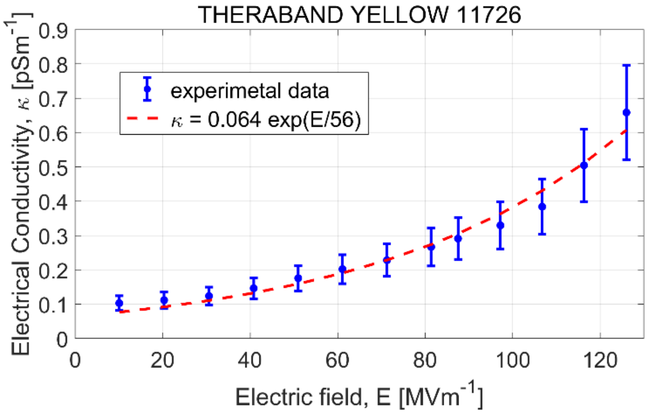

Figure 4.9. Electrical conductivity vs electric field for THERABAND YELLOW 11726 with an equi-biaxial stretch of $\lambda = 2$: experimental data (blue dot marker with errorbar); exponential law fitting (red dashed line).

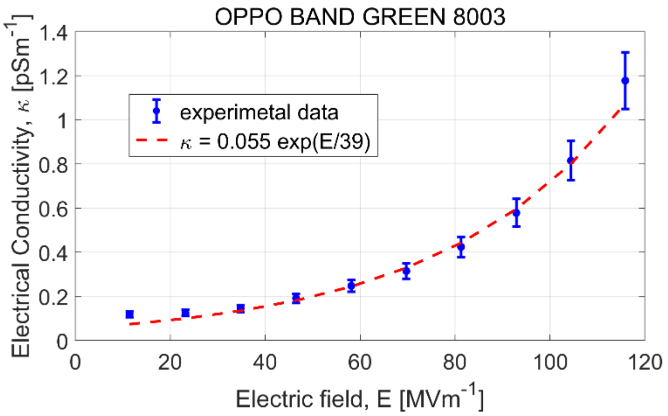

Figure 4.10. Electrical conductivity vs electric field for OPPO BAND GREEN 8003 with an equi-biaxial stretch of $\lambda = 2$: experimental data (blue dot marker with errorbar); exponential law fitting (red dashed line).

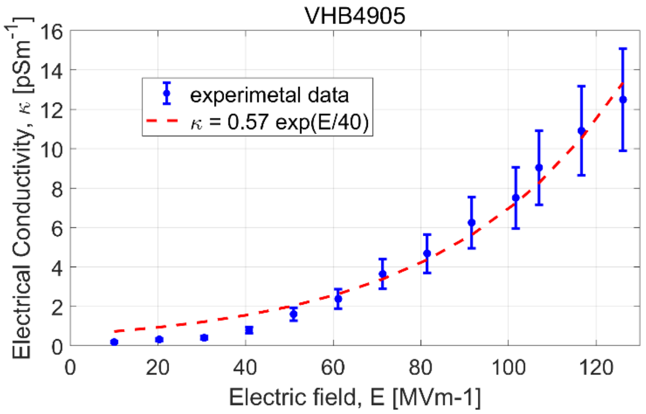

Figure 4.11. Electrical conductivity vs electric field for VHB 4905 with an equi-biaxial stretch of $\lambda = 5$: experimental data (blue dot marker with errorbar); exponential law fitting (red dashed line).

Property	THERABAND^{TM} YELLOW 11726	OPPO BAND^{TM} GREEN 8003	VHB^{TM} 4905
Conductivity at low field (@E_B):			
κ_0 [pS/m]	0.064	0.055	0.57
Conductivity exponential law parameter:			
E_B [MV/m]	56	39	40

Table 4.2. Fitted parameters for conductivity based on measured data on the three considered DE membranes.

Figures and table highlight the following:

- The conductivities of THERABAND YELLOW 11726 and OPPO BAND GREEN 8003 are in the same order of magnitude with the former performing better from moderate to high electric field levels. In particular, THERABAND YELLOW 11726 is characterized by a slightly larger conductivity at low electric fields (it features a κ_0 parameter that is $16\ \%$ larger); OPPO BAND GREEN 8003 is instead more sensitive to electric field variations (it features a E_B parameter that is 30% smaller).
- VHB 4905 is rather dissipative; its electrical conductivity is one order of magnitude larger than that of the other two materials, mostly due to a large value of κ_0 (8.9 times larger than that of THERABAND YELLOW 11726 and 10.3 times larger than that of OPPO BAND GREEN 8003)

The above reported results are acquired on specimens made of the same material and subjected at the same level of stretch. To verify the eventual dependency of electrical conductivity on mechanical strain, tests have been additionally performed on four specimens of VHB 4905 subjected to four different stretches $\lambda = 3, 4, 5, 6$. Results are reported in Fig. 4.12 with different markers, which show a rather limited dependency of electrical conductivity on mechanical strain.

As compared to other results existing in the literature, the findings reported here for the VHB 4905 are in line with those described in [53] and obtained for the same material but samples with different geometry (namely, expanding circles with $25mm$ initial diameter). Considering indeed the data plotted in [53] for an electric field equal to $125MV/m$, one can estimate an average conductivity of $\kappa\,(E = 125\ MV/m)\ \approx 10.17pS/m$ evaluated over nine nominally identical specimens, with maximum and minimum values equalling $50pS/m$ and $5pS/m$ (the smallest value being much far away from the others for which it may be considered as an outlier).

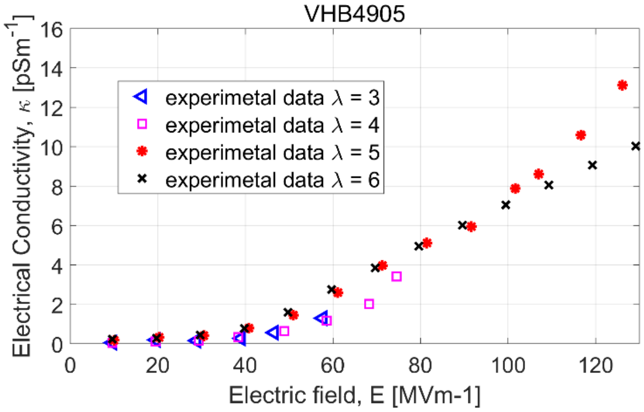

Figure 4.12. Electrical conductivity vs electric field for VHB 4905: results comparison for specimens tested at different levels of equi-biaxial stretch (λ)

4.2.4 Measurement of membrane dielectric constant

The experimental results of the tests conducted for assessing the dielectric constant of the considered DE membranes and its eventual dependency on applied strain are reported in Fig. 4.13-15. In particular:

- Fig. 4.13 and 4.14 report the dielectric constant data respectively acquired on the THERABAND YELLOW 11726 membrane and on the OPPO BAND GREEN 8003 membrane tested at the following three levels of equi-biaxial stretch $\lambda = 1, 2, 3$.
- Fig. 4.15 reports the dielectric constant data acquired on the VHB 4905 membrane tested at the following four levels of equi-biaxial stretch $\lambda = 3, 4, 5, 6$.

In the figures, blue dot markers represent the average over the three measurements performed on the three specimens tested at the same conditions, with the blue error bar representing their standard deviation. The red dashed line corresponds instead to the mean dielectric constant of the material, which is reported in Table 4.3, that is obtain by averaging all the measurements performed on the same material for all the applied strain levels.

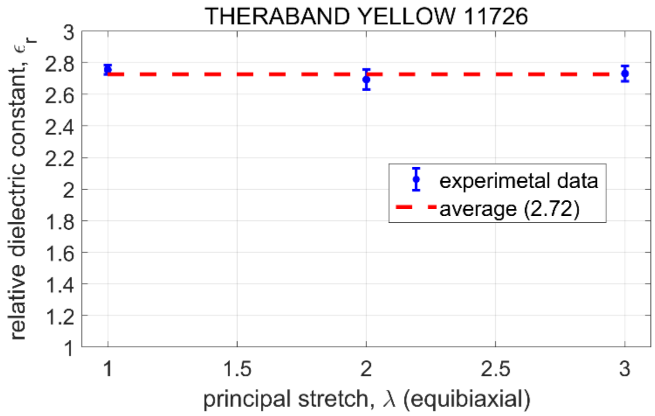

Figure 4.13. Dielectric constant vs stretch correlation for THERABAND YELLOW 11726: experimental data (blue dot marker with errorbar); Average value (red dashed line).

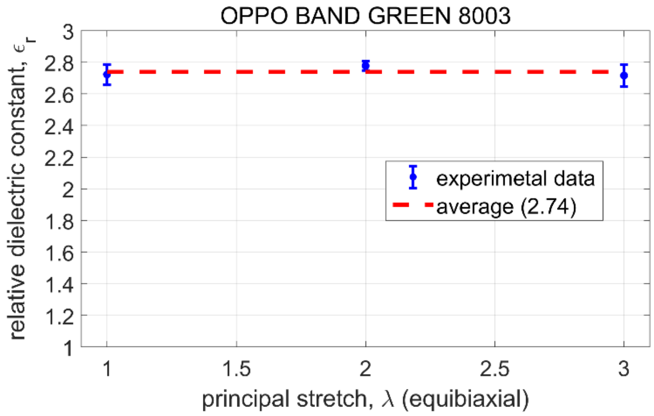

Figure 4.14. Dielectric constant vs stretch correlation for OPPO BAND GREEN 8003: experimental data (blue dot marker with errorbar); Average value (red dashed line).

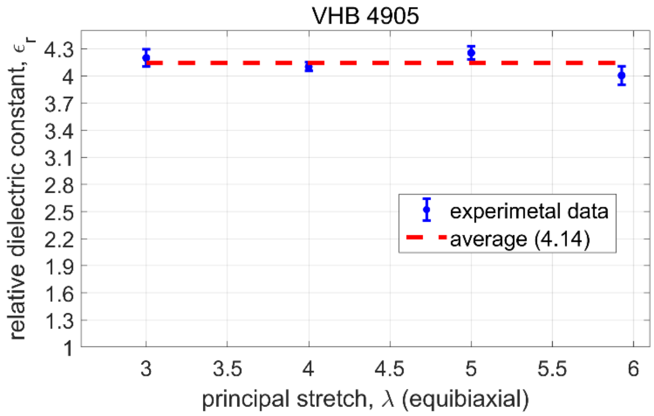

Figure 4.15. Dielectric constant vs stretch correlation for VHB 4905: experimental data (blue dot marker with errorbar); Average value (red dashed line).

Property	THERABAND^{TM} YELLOW 11726	OPPO BAND^{TM} GREEN 8003	VHB^{TM} 4905
Dielectric constant (average):			
ε_r	2.72	2.74	4.14

Table 4.3. Average dielectric constants for the three DE materials.

Overall, the presented results show:

- A rather negligible dependency of dielectric constant on applied strain for all the considered materials and deformation ranges;
- The average dielectric constants of THERABAND YELLOW 11726 and OPPO BAND GREEN 8003 are very similar, with the latter being slightly larger;
- The VHB 4905 is the material with better dielectric constant.

As compared to other results existing in the literature, the findings obtained here for the OPPO BAND GREEN 8003 are in line with those described in [3] which reports a dielectric constant $\varepsilon = 2.8$. However, this is not the case for the VHB 4905 membrane; in many papers, indeed, its thicker version (the VHB 4910) is quoted to have a dielectric constant that varies sensibly with strain. Table 4.4 compares the values of dielectric constant estimated here for three stretch levels ($\lambda = 3, 4, 5$) with those extracted from four well-known papers [24], [51], [54], [55]. Clearly, results are not consistent across different works which can attributed to the following reasons:

- Formation of an air film between electrodes and tested specimen in the case of rigid electrodes that is due to the surface roughness of the membrane. This air film may reduce the measured value of capacitance, with the reduction typically increasing with specimen stretch since the effective area of contact between electrode and membrane is likely to diminish with biaxial strain (since thinner portions of the membrane deform more than the thicker ones, the ratio between crest area and valley area of the surface roughness of the membrane is expected to decrease with strain).
- Influence of edge effects on the measured value of capacitance which, according to the standard ASTM D150 and as more detailed in [56], provide an error on the measured dielectric constant that increases as the diameter of the electrode decreases, as the height of the electrode increases and as the thickness of the membrane under test increases

(thereby, as the stretch applied to a same virgin membrane decreases). As mentioned in Section 3.4, this effect should be negligible for the electrode arrangement considered here. However, this is less the case of the set-ups adopted in existing works, for which the ratio of fringing capacitance (estimated as per standard ASTM D150 and [56]) and measured capacitance can be as high as ten percent and function of the strain applied to the specimen.

In support to these arguments, it is worth recalling the results obtained in a preliminary work [57], where a thinner version of the membrane OPPO BAND GREEN 8003 (the OPPO BAND RED 8012) was tested with the cylindrical brass electrodes shown in Fig. 4.2, which provided a permittivity significantly dependent on strain (thus, a response that is not consistent to that reported here for the OPPO BAND GREEN 8003 that is made of the same natural rubber).

	This paper	Kofod et al. [54]	Mazza et al [55]	Li et al. [24]	Tröls et al. [51]
	VHB 4905	VHB 4910	VHB 4910	VHB 4910	VHB 4910
	Carbon grease electrodes	Planar metal + carbon black electrodes	Cylindrical gold electrodes	Rigid platinum electrodes	Silver paste electrodes
	80 mm diameter	30 mm diameter	25 mm diameter	Unknown diameter	14 mm diameter
	Test at 20 Hz	Test at 1-10Hz	Test at 100 Hz	Unknown frequency	Test at 1Hz
$\lambda = 3$	$\varepsilon_r = 4.198$	$\varepsilon_r \approx 4.55$	$\varepsilon_r = 3.71$	$\varepsilon_r \approx 3$	$\varepsilon_r = 3.83$
$\lambda = 4$	$\varepsilon_r = 4.101$	$\varepsilon_r \approx 4.48$	$\varepsilon_r = 3.34$	$\varepsilon_r \approx 2.75$	$\varepsilon_r \approx 3.60$
$\lambda = 5$	$\varepsilon_r = 4.254$	$\varepsilon_r \approx 4.48$	$\varepsilon_r = 2.62$	$\varepsilon_r \approx 2.5$	$\varepsilon_r = 3.44$

Table 4.4. Fitted parameters for conductivity based on measured data on the three considered DE membranes.

4.3 Mechanical response results

This section presents the results of the mechanical tests conducted on pure shear specimens made of the considered materials. In particular, for each material it reports the stabilized stretch-stress curves for loading-unloading cycles performed at different strain rates and for two different strain amplitudes.

The experimental results considering deformation amplitude of large stroke (see Section 4.1.5) are presented in Fig. 4.16-18, while results considering deformation amplitude of intermediate stroke (see Section 4.1.5) are presented in Fig. 4.19-21.

The mechanical response of hyperelastic materials can be described through phenomenological models, which are generally based on a scalar function referred as strain energy. Strain energy density functions (Ψ) take different forms in different proposed models. Some models consider functions that depend on the principal stretches as $\Psi(\lambda_1, \lambda_2, \lambda_3)$, like the model proposed by Ogden; some other consider functions that depend on the strain invariants as $\Psi(I_1, I_2)$ (the third invariant is not considered since DE membranes are generally assumed to be incompressible and thus $I_3 = \lambda_1^2\lambda_2^2\lambda_3^2 = 1$); Neo-Hookean and Mooney-Rivlin models belong to this category. The strain invariants are extracted from the Cauchy-Green stress tensor with the forms $I_1 = \lambda_1^2 + \lambda_2^2 + \lambda_3^2$ and $I_2 = \lambda_1^2\lambda_2^2 + \lambda_2^2\lambda_3^2 + \lambda_3^2\lambda_1^2$. Due to the finite chain length of the polymer's macromolecules, hardening phenomenon occurs when a relatively large strain is applied to the material. From [58]–[60], to cope with this effect, Gent has proposed a hyperelastic strain energy function having the form:

$$\Psi = -\frac{\mu}{2} J_m \ln\left(1 - \frac{I_1 - 3}{J_m}\right) \tag{4.1}$$

with μ being the shear modulus and J_m the limiting value for quantity $I_1 - 3$. The limit on invariant I_1 also limits all the principal stretches. When $I_1 - 3 \to J_m$, $\Psi \to \infty$; hence, hardening effect is reflected in the large strain region. Gent's model has been verified to be accurate in the large strain region but not in the small strain region. In [58], the author combines the Gent's model with the Gent-Thomas logarithmic term ([61]) to achieve a so-called Gent-Gent model featuring strain energy function in the form

$$\Psi = -\frac{\mu}{2} J_m \ln\left(1 - \frac{I_1 - 3}{J_m}\right) + C_2 \ln\left(\frac{I_2}{3}\right) \tag{4.2}$$

with C_2 being an additional material parameter. This model aims to capture the mechanical response of polymers both in small strain and large strain region. The obtained mechanical response results have been fitted according to this model. The fitted models are plotted in Fig. 4.16-21 with parameters listed in Table 4.5.

As can be seen from the figures, this model fits extremely well with the obtained results in both large stroke and intermediate stroke cases for all the three different DE materials. Thus, the Gent-Gent model can be considered as a robust hyperelastic model for describing DE membranes to be used in DET control and design. The results also show that testing at different strain rates have little effect on the mechanical response for THERABAND YELLOW 11726 and OPPO BAND GREEN 8003 specimens. For VHB 4905, the mechanical response is instead affected by the testing strain rate; especially at the two ends of the stroke for the large stroke case. In the intermediate stroke case, this dependence is smaller.

The hysteresis losses during one cycle of stroke (calculated as the area enclosed by the stretch-stress trajectory) for the considered DE membranes are also reported in Table 4.6. From Table 4.6, the testing strain rates seem to have little influence on the hysteresis loss. This is not the case for the testing stroke range, especially for OPPO BAND GREEN 8003 specimens. While for THERABAND YELLOW 11726 specimens the hysteresis is negligibly affected by the stroke range and for VHB 4905 specimens the hysteresis only increases mildly with the larger stroke, the hysteresis loss in OPPO BAND GREEN 8003 specimens increases over 7 times in the larger stroke case.

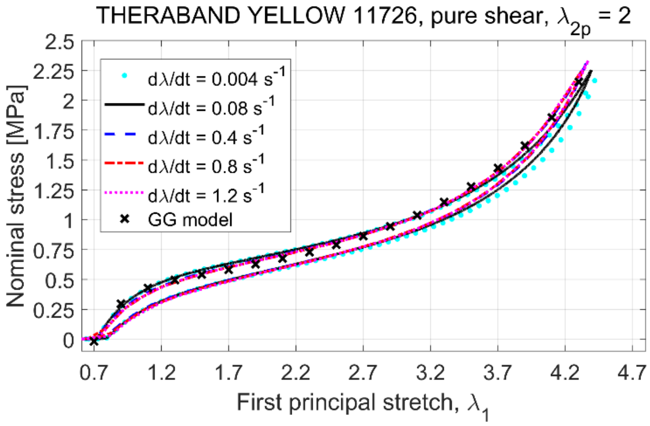

Figure 4.16. Cyclic stress-strain response of a pure-shear specimen with transversal pre-stretch $\lambda_{2p} = 2$ made of THERABAND YELLOW 11726 for large stroke: experimental data at different strain rates (with different markers) vs. Gent-Gent (GG) model fitted on the large stroke data acquired at a strain rate of $0.4s^{-1}$ (black cross markers, fitted parameters are reported in Table 4.5).

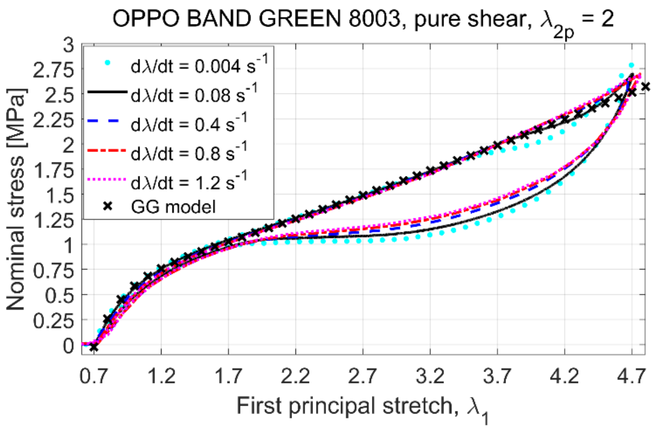

Figure 4.17. Cyclic stress-strain response of a pure-shear specimen with transversal pre-stretch $\lambda_{2p} = 2$ made of OPPO BAND GREEN 8003 for large stroke: experimental data at different strain rates (with different markers) vs. Gent-Gent (GG) model fitted on the large stroke data acquired at a strain rate of $0.4s^{-1}$ (black cross markers, fitted parameters are reported in Table 4.5).

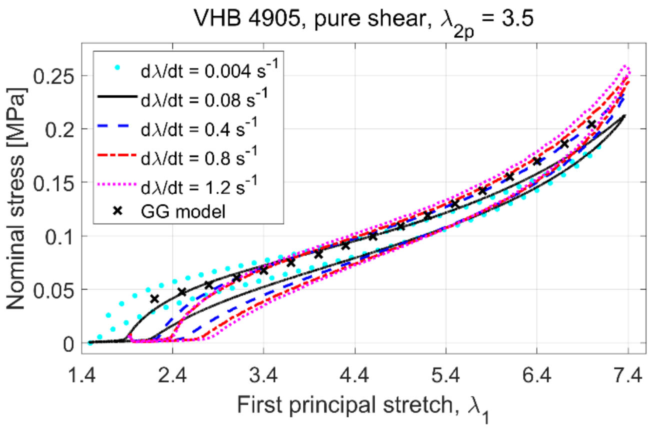

Figure 4.18. Cyclic stress-strain response of a pure-shear specimen with transversal pre-stretch $\lambda_{2p} = 3.5$ made of VHB 4905 for large stroke: experimental data at different strain rates (with different markers) vs. Gent-Gent (GG) model fitted on the large stroke data acquired at a strain rate of $0.4s^{-1}$ (black cross markers, fitted parameters are reported in Table 4.5).

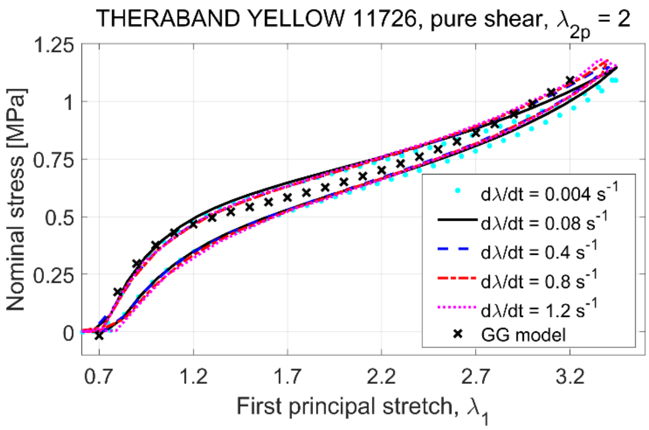

Figure 4.19. Cyclic stress-strain response of a pure-shear specimen with transversal pre-stretch $\lambda_{2p} = 2$ made of THERABAND YELLOW 11726 for intermediate stroke: experimental data at different strain rates (with different markers) vs. Gent-Gent (GG) model fitted on the large stroke data acquired at a strain rate of $0.4s^{-1}$ (black cross markers, fitted parameters are reported in Table 4.5).

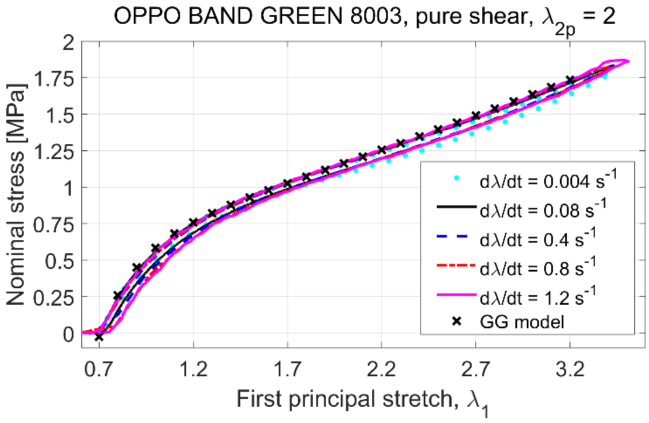

Figure 4.20. Cyclic stress-strain response of a pure-shear specimen with transversal pre-stretch $\lambda_{2p} = 2$ made of OPPO BAND GREEN 8003 for intermediate stroke: experimental data at different strain rates (with different markers) vs. Gent-Gent (GG) model fitted on the large stroke data acquired at a strain rate of $0.4s^{-1}$ (black cross markers, fitted parameters are reported in Table 4.5).

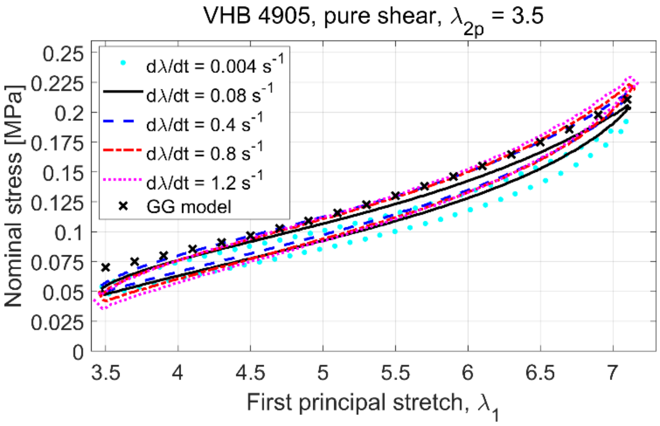

Figure 4.21. Cyclic stress-strain response of a pure-shear specimen with transversal pre-stretch $\lambda_{2p} = 3.5$ made of VHB 4905 for intermediate stroke: experimental data at different strain rates (with different markers) vs. Gent-Gent (GG) model fitted on the large stroke data acquired at a strain rate of $0.4s^{-1}$ (black cross markers, fitted parameters are reported in Table 4.5).

Property	THERABAND^{TM} YELLOW 11726	OPPO BAND^{TM} GREEN 8003	VHB^{TM} 4905
1^{st} modulus of the Gent-Gent model:			
μ (@$0.4s^{-1}$) [KPa]	187.63	494.10	16.57
Parameter of the Gent-Gent model:			
J_m (@$0.4s^{-1}$)	36.9	541	141.8
2^{nd} modulus of the Gent-Gent model:			
C_2 (@$0.4s^{-1}$) [KPa]	185.93	183.80	0

Table 4.5. Fitted parameters of Gent-Gent model that describing the mechanical properties of THERABAND YELLOW 11726, OPPO BAND GREEN 8003 and VHB 4905.

		Deformation rate $[s^{-1}]$				
		0.004	0.08	0.4	0.8	1.2
THERABAND™ YELLOW 11726	Intermediate Stroke	10.17	10.24	9.4	10.13	11.23
	Large Stroke	11.9	10.27	8.99	8.72	11.18
OPPO BAND™ GREEN 8003	Intermediate Stroke	4.79	3.89	3.53	4.33	5.16
	Large Stroke	24.17	23.24	21.21	19.45	18.89
VHB 4905	Intermediate Stroke	10.83	10.47	11.07	11.33	12.84
	Large Stroke	12.36	11.9	14.64	16.70	18.95

Table 4.6 Hysteresis loss in a cycle as function of strain rate and range of deformation: THERABAND YELLOW 11726 vs. OPPO BAND GREEN 8003 vs. VHB 4905.

Chapter 5

Lifetime Characterization on DET Specimens

In this work, a custom experimental set-up has been designed and implemented to perform lifetime characteristic investigation on DET specimens.

In order to cope with the stochastic approach for characterizing the lifetime characteristic of DET configuration, the experimental set-up should have the capabilities in:

- Testing multiple specimens simultaneously to save time for generating statistically meaningful amount of data in order to validate the lifetime probability distribution;
- Commanding high voltage signal and ensuring galvanic isolation: as introduced in previous chapters, to simulate the practical electrical loading during the operation of DETs, the experimental electric field signal is chosen as square-wave electric field waveform with 50% duty cycles. Since DETs generally prefer high voltage operating condition for maximizing the performance, the magnitude of the experimental field signal needs the applied voltage in the range of several kilovolts. Isolation between high voltage operating circuit and low voltage signal circuit is mandatory for safety and avoiding damage on devices;
- Monitoring and acquiring voltage and current signals of the DET specimens: since the failure of DET specimens leads to electrical breakdown, the voltage and current in the high voltage circuit are occasionally suffering from unexpected and abruptly variation during the test. Thus, accurate and fast response on the status of the circuit is essential;
- Handling of failed DET specimens without affecting the continuation of the test.

As mentioned in Chapter 3, operational mechanical loading is not considered during the test for the DET specimens. Besides the assumption that operational mechanical loadings might be minorly affecting the lifetime characteristics, they also appear in variety of forms: depending on the DET configurations, their form might vary from inflating, in-plane stretching, bending etc. Thus, for now the only mechanical loading considered in this thesis is the constant pre-stretching that applied to the DET specimens during the preparation of specimens. In the future, experimental set-up considering combined mechanical-electro loading, which simulates practical working conditions for an inflatable DET wave energy harvester (introduced in [18], [30]), will be developed.

The proposed experimental set-up will be introduced in Section 5.1, the DET specimen preparation will be covered in Section 5.2, in the Section 5.3, control strategy for the experimental set-up will be introduced. Finally, in Section 5.4 and 5.5, the lifetime results of the two considered DE materials are reported.

5.1 Experimental set-up

5.1.1 Experimental set-up functionality

Four test benches have been developed in this work. Each of them enables:

- Testing up to 16 identical circular planar DET specimens at the same time;
- Data acquisition system that could monitor and archive voltage and current signals in high voltage DET circuit with a sampling frequency of up to $10kHz$;
- Fully automated operation, including automatic detection and isolation of broken DETs;
- Galvanic isolation between high voltage (HV) and low voltage (LV) circuitry via isolated amplifiers and DC/DC converters.

The schematic of experimental set-up is shown in Fig. 5.1, with a photo of an actual test bench is shown in Fig. 5.2.

A single HV DC/DC converter (Ultravolt 10C24-P125, $10kV$, $12.5mA$, $125W$) is used to apply the desired level of electric field on all the DET specimens. The HV DC/DC converter is powered up by a $24V$ DC power supply, TDK-Lambda LS150-24C, and enclosed within a custom modified plastic IP65 case. The HV converter is controlled via a $0\text{-}10V$ voltage analogue commanding signal and a digital enabling signal ($0\text{-}0.8V$ for disable and $2\text{-}32V$ for enable). Monitoring signals for voltage and current at output side of the HV converter are also available as analogue signals. The enable commanding signal is connected in series with a mechanical stop button, indicated as S_E in the schematic, for emergency shutdown in case of hazardous situations. Since the considered HV converter does not sink current, to prevent back discharging from DET specimens to the HV converter, especially in case of a short circuit (with potentially high explosive hazard), a forward biased diode (HVStuff, $100mA$, $30KV$, indicated with the letter D in the schematic) is placed at the output port of the HV converter.

At the specimens' side, all DET specimens are connected in-parallel to be tested simultaneously. The upper electrode of the ith specimen is connected to the main circuit through a HV reed relay (MEDER electronic Standex HE24-1A69-02, the same as all the rest reed relays involved in the setup), indicated with the letter S_i in the schematic. This relay is responsible for isolating the failed DET specimens. The HV reed relays are commanded through digital signals (0-$2V$ for disable and 18-$24V$ for enable) for on/off switching. The lower electrodes of all DET specimens are joined together and connected in series with a custom-designed current sensor incorporated with galvanic isolation for monitoring the total current flow through the specimens. Voltage divider with galvanic isolation is placed in parallel to the specimen array for monitoring the voltage.

As introduced previously, the testing electrical loading is square-wave electric field waveform. Since DETs are indeed capacitors, the experimental circuit should be able to handle the charging and discharging phases of the DET specimens properly without damaging the associated devices.

For charging phase, DET specimens are charged through resistor R_C ($R_C = 850k\Omega$, Vishay VR68 resistors). R_C limits the maximum charging current under the maximum output condition that can be provided by the HV converter ($V_{out} = 10kV$, $I_{out} = 12.5mA$). For the maximum output condition, the considered DC/DC converter has a rising time of $1.2ms$ for step commanding signal. For the charging phase of a square-wave electric waveform around $1Hz$ (similar to practical operation frequency of DET generator for harvesting wave energy) this converter is more than capable.

Since the circuit is designed to test variety of DET specimens, the resistance and capacitance of the specimen array are undefined. Thus, the discharging time of the DET specimens is also not fixed. The discharging of the DET specimens will be performed via a dedicated route to ensure a completely discharging during the off state of square-wave electric field waveform. As shown in Fig. 5.1, this route is consisting of a HV reed relay S_D and two discharging resistors R_{D1} and R_{D2} placed in series. The two resistors are used for limiting the instantaneous power on the relay. The rated power of the HV reed relay (HE24-1A69-02) is $50W$, any combination of voltage and current that applied across the relay should not exceed this value. Thus, in extreme case that at the beginning of discharging phase when S_D is closed, the maximum applied voltage V_{max} that was retained by DET specimens from previous charging phase will apply across the S_D. The instantaneous power should then be limited as

$$\frac{V_{max}^2}{R_C + R_{D1} + R_{D2}} \leq 50(W) \tag{5.1}$$

For maximum output voltage $V_{out} = 10kV$, we have $R_C + R_{D1} + R_{D2} \geq 2M\Omega$. From the available resistors, $R_{D1} = R_{D2} = 1M\Omega$, Vishay VR68 resistors have been chosen.

The charges on the internal capacitor of HV converter also need a proper discharging route. A resistor R_S is applied in-parallel with output side of the converter. This resistor is constantly in operating during both charging and discharging phase. According to the requirements on the rated power, voltage and discharging time, a $22.5M\Omega$ resistance which consists of two Vishay ROX-1-1/2 resistors of $45M\Omega$ connected in parallel is chosen for this role.

The switching between the charging phase and discharging phase is controlled via a HV reed relay S_C. As shown in Fig. 5.1, when S_C is opened, the circuit is separated into two discharging routes mentioned previously, indicates the discharging phase. When S_C is closed, the HV converter is able to charge up the DET specimens, indicates the charging phase.

The discharging relay S_D, the switching relay S_C and the square-wave voltage commanding signal should operate in phase to ensure correct charging and discharging operation. To extend the lifespan of the HV relays, avoiding switching during high voltage is preferable (except for S_D which is inevitable, hence the necessary of resistors R_{D1} and R_{D2}).

All the cable junctions in the HV area will be wrapped with 3M VHB4905 tape for insulation.

Control of the HV converter and relay switching as well as data acquisition of monitoring signals are performed via a PC-based automation system composed by Beckhoff controllers and Bekchoff I/O modules.

The related models of Beckhoff controller are industrial PC C5102-0060 and embedded PC CX5140-0125. TE1400 (TwinCAT3 Target for MATLAB®/Simulink®) and the TC1220-0080 (TwinCAT3 PLC/C++/MATLAB®/Simulink®) software modules have been installed on the industrial PC, while the embedded PCs only have TC1220-0080 installed. Through dedicated System Target File for MATLAB®/Simulink® coder, TE1400 module enables generation of

TwinCAT3 runtime modules based on MATLAB® scripts or Simulink® model.. TC1220-0080 allows the real-time execution of the generated modules.

The related Bekchoff I/O modules are:

- Digital output modules EL2808 and EL2804 are applied for commanding HV relays and HV converter enable signal;
- Analogue output modules EL4132 are applied for commanding the square-wave electric field waveform to HV converter;
- Analogue input modules EL3104 are applied for acquiring voltage and current monitoring signals.

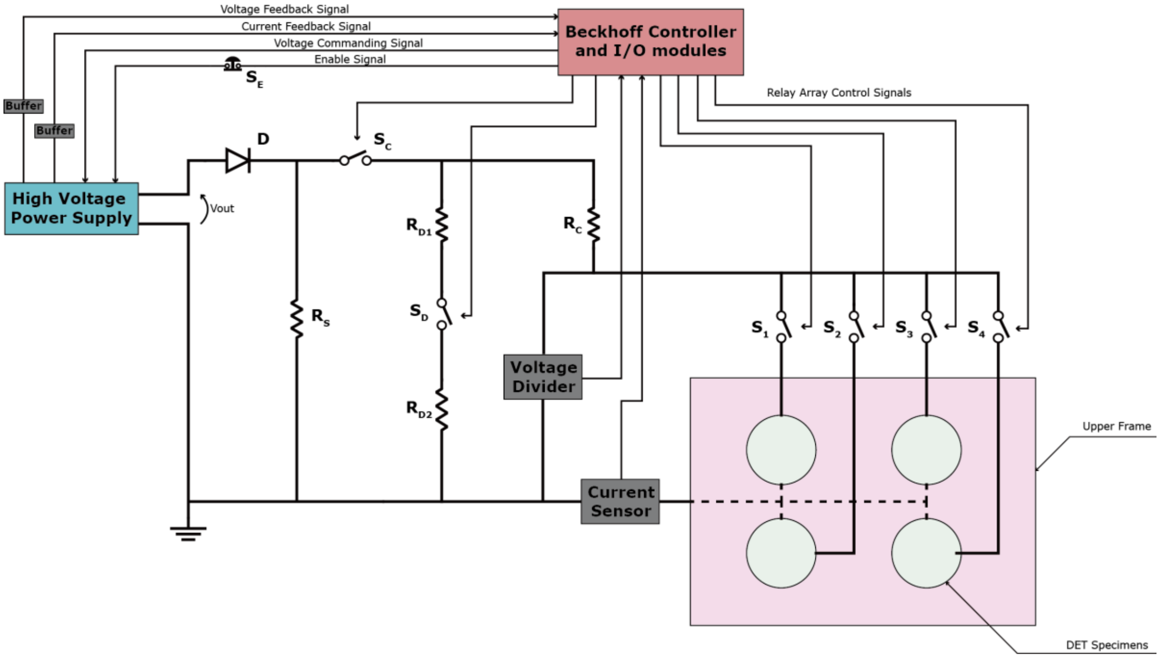

Figure 5.1. Schematic of the test benches, only 4 specimens are presented for simplicity.

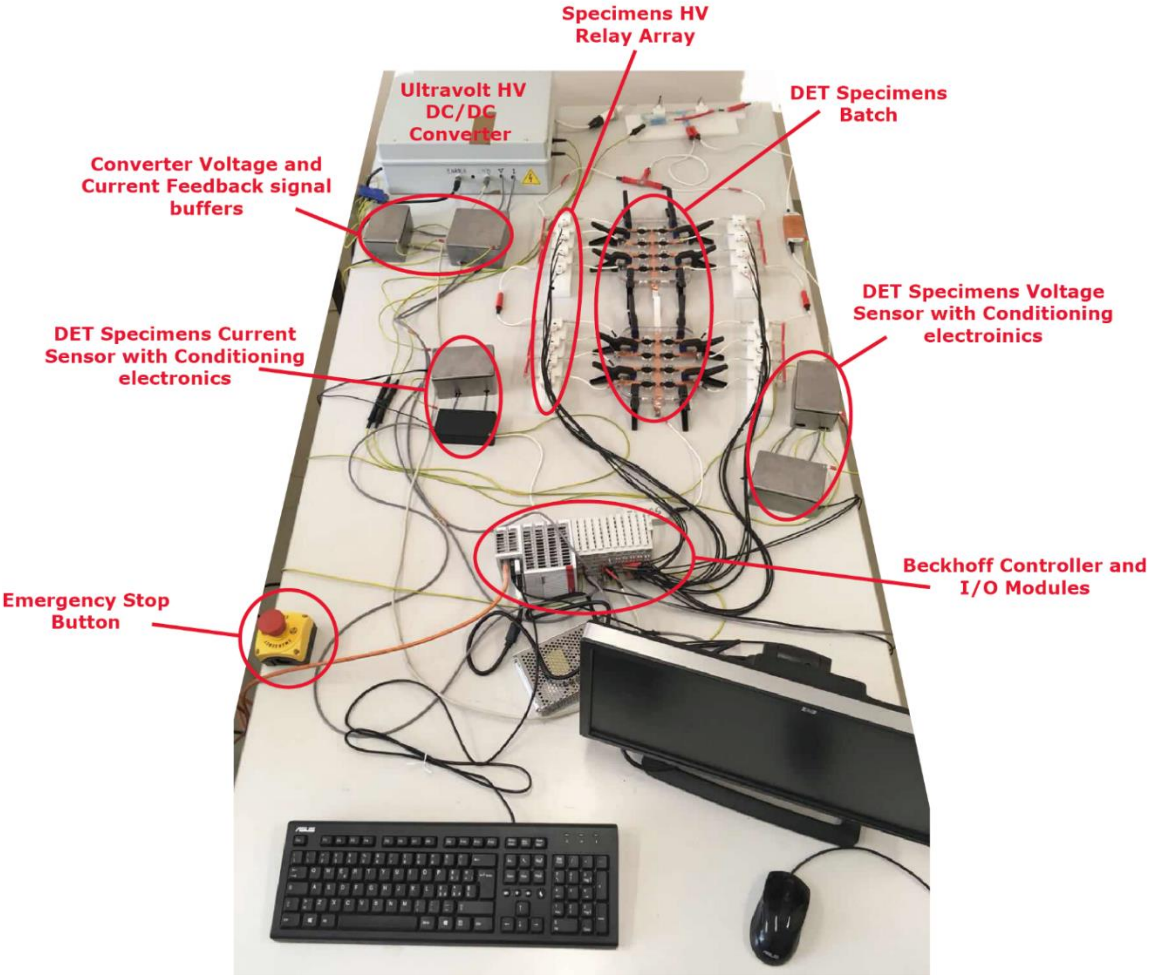

Figure 5.2. A picture for one of the implemented test benches that is testing two batches of silicone DET specimens.

5.1.2 Galvanic isolation and monitoring circuits

All the circuits mentioned in this section were custom-prepared on copper strip boards. The copper strip within the galvanic isolation gap indicated in the corresponding circuits have been milled off to ensure the isolation.

Voltage divider

Measurement of the voltage across the DET specimens is implemented via an external custom-made voltage divider. The schematic of the voltage divider, incorporated with galvanic isolation, is shown in Fig. 5.3, a picture of the circuit is shown in Fig. 5.4.

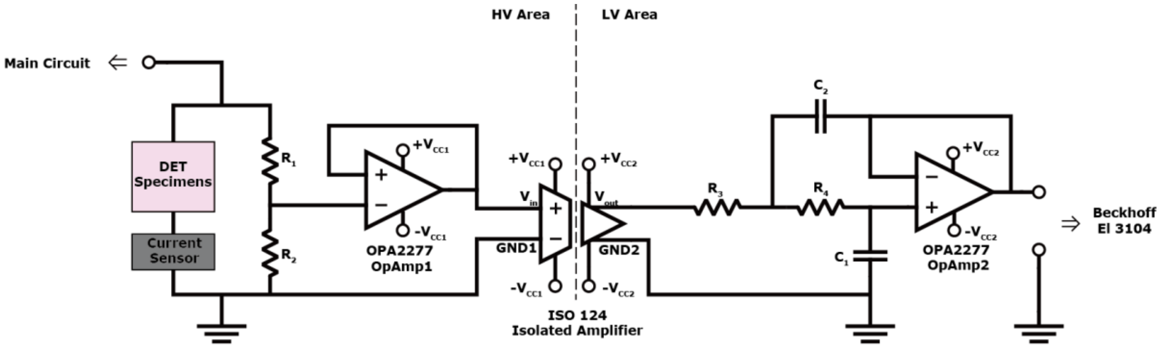

Figure 5.3. Schematic of the voltage divider with galvanic isolation, input buffering and output filter.

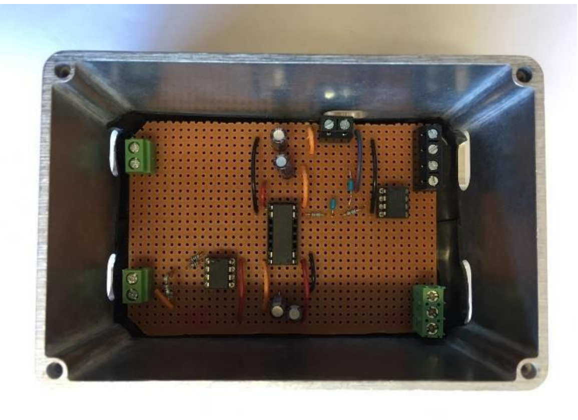

Figure 5.4. A picture of the voltage divider. The circuit is enclosed within a metal box working as Faraday shield, with SCOTCH 130C black electrical insulation tape utilized for the insulation.

Since the Beckhoff data acquisition system operates in LV condition (in the range of $0\text{-}24V$) while the DET specimens are tested under HV condition (in the range of $0\text{-}10kV$), to avoid high voltage entering data acquisition system and leading to permanent device damage or hazardous state, galvanic isolation is necessary to separate the HV area and LV area. As the name indicated, the major principle for galvanic isolation is to forbid direct conduction path between the isolated circuits, while information or energy can still be transmitted from one circuit to another through other means. Common communication means are induction, optical, acoustical etc. In this circuit, isolated amplifiers (Texas Instruments ISO124) have been used for the galvanic isolation. This isolated amplifier isolates the output circuit from input circuit through capacitor barriers. The modulator at input side of the isolated amplifier transforms the input voltage signal into duty-cycle modulated square-wave signal. The modulated signal will transmit through the capacitor barrier to the output side, while the demodulator at the output side retrieves and integrals the transmitted signal to recreate the input voltage at the output port. Since this working principle involves high frequency modulation-demodulation processing of signals, ripple will present at the recreated output voltage. A two-pole unity-gain filter of Sallen-Key type is suggested, according to the ISO124 datasheet, to be placed in series with the isolated amplifier output port. The Sallen-Key filter is composed of resistors R_3, R_4, capacitors C_1 and C_2 and operation amplifier $OpAmp2$ (Texas Instruments, OPA2277) as shown in Fig. 5.3. The cut-off frequency f_C and the Q factor of the Sallen-Key type filter can be calculated as,

$$f_C = \frac{1}{2\pi}\frac{1}{\sqrt{R_3 R_4 C_1 C_2}} \tag{5.2}$$

$$Q = \frac{\sqrt{R_3 R_4 C_1 C_2}}{C_1(R_3 + R_4)} \tag{5.3}$$

Given $f_C = 10kHz$, which is the maximum considered sampling frequency, and Q=1, which indicates no peaking at the cut-off frequency in Bode Plot for the frequency response of the filter. According to available resistors and capacitors, $R_3 = 14.97k\Omega$, $R_4 = 1.8k\Omega$, $C_1 = 1nF$, $C_2 = 10nF$ have been chosen for the filter circuit.

The voltage divider function is realized based on two resistors R_1 and R_2 (with $R_1 = 1.5G\Omega$ and $R_2 = 1M\Omega$, a ratio of $1500{:}\,1$). R_1 is the crucial resistance that needs to sustain most of the high voltage and the corresponding power, an Ohmite Slim-Mox resistor is chosen for this role. Since input impedance of the isolated amplifier ($200k\Omega$) is lower than the output impedance of this voltage divider ($1M\Omega$), the input voltage for ISO124 will be attenuated from the correct level. Thus, a simple voltage follower (based on $OpAmp1$) with large input impedance is placed between output port of voltage divider and input port of the isolated amplifier.

Since operation amplifiers are active devices, additional power supplies are necessary for the operation (shown in figure as V_{CC1} and V_{CC2}). To ensure again isolation between HV area and LV area, isolated DC/DC converters are utilized: RECOM Power REC6-2412DRW/R10/A for V_{CC1} and Murata MEV1D2412DC for V_{CC2}. Both provides $\pm 12V$ dual output voltage to the amplifiers to cover the considered analogue signal range. Both isolated DC/DC converters in the HV and LV area have their output $\pm 12V$ bypassed by two $1\mu F$ capacitors which locate as close to the isolated amplifier as possible, as suggested in the ISO124 datasheet.

Current sensor

Measurement of the current flowing across the DET specimens is performed between the DEG specimens and ground via an isolated amplifier and a shunt resistor (Texas Instruments AMC1301).

The schematic of the current sensor, incorporated with galvanic isolation, is shown in Fig. 5.5, a picture of the circuit is shown in Fig. 5.6.

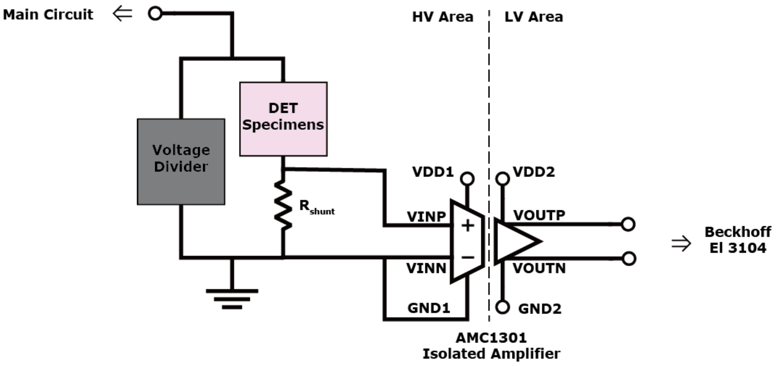

Figure 5.5. Schematic of the current sensor with galvanic isolation.

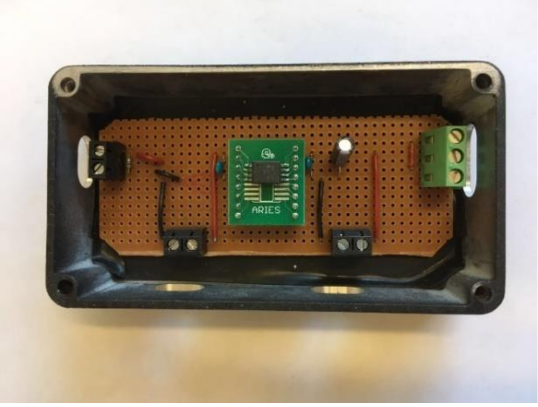

Figure 5.6. A picture of the current sensor. The circuit is enclosed within a metal box working as Faraday shield, with SCOTCH 130C black electrical insulation tape utilized for the insulation.

The galvanic isolation in AMC1301 is achieved through SiO_2-based, double-capacitive isolation barrier. Analog signal comes into AMC1301 will be modulated into digital bitstreams that could commutes through the capacitive barrier, similar to ISO124, and will be demodulated at the output side. The input range for AMC1301 is $\pm 250mV$, since the maximum current for the HV converter is $I_{out} = 12.5mA$, the shunt resistor is chosen as $R_{shunt} = 20\Omega$ to fulfill the range and maximize accuracy. Since the input impedance of AMC1301 ($18k\Omega$) is significantly larger than R_{shunt}, no voltage follower is needed at the input of AMC1301.

Since the considered DET specimens have relatively small capacitance (in the range of picofarad), the dynamic of current is relatively fast, thus at first no filter is applied at the output port of the current sensing signal.

Power supplies for AMC1301, shown in Fig. 5.5 as $VDD1$ and $VDD2$ are also carried out by isolated DC/DC converters to ensure isolation. RECOM Power REC6-2405SRW/R10/A for $VDD1$ and Murata MEV1S2405DC for $VDD2$ are chosen for powering up AMC1301 with 5V single output voltage.

5.2 DET specimens preparation

An exploded 3D view for general schematic of one batch of DET specimens is shown in Fig. 5.7.

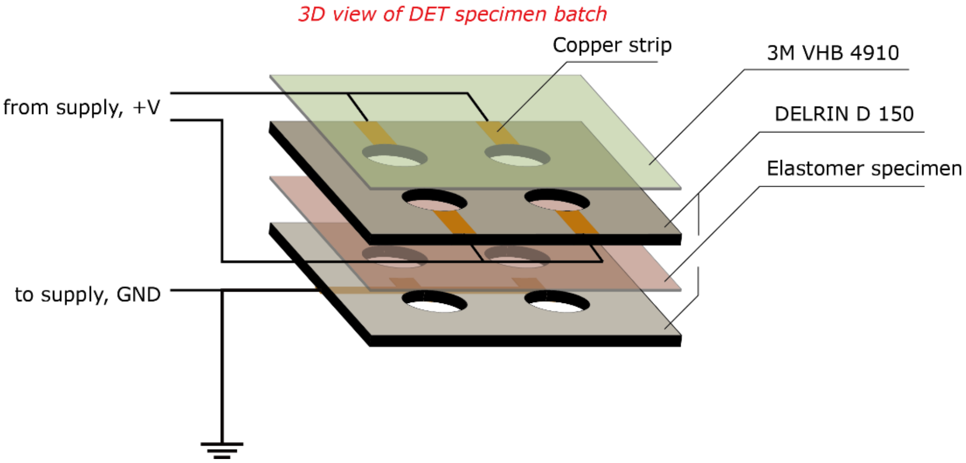

Figure 5.7. Schematic of a batch of DET specimens, only 4 specimens are presented for simplicity.

This schematic represents a basic configuration of DET as plate capacitor and is applicable for both styrenic and silicone DET specimens. The DE material is sandwiched between two frame plates in a pre-stretched configuration. An equi-biaxial pre-stretch is applied to all DET specimens on one batch of DET specimens. The pre-stretch ratio is chosen, accordingly for different DE materials, to achieve the most mechanically stressed configuration that is likely to happen in real applications as well as to reduce membrane thickness so as to make it suitable to be tested with the available HV converter. The plastic plates are holed, with each hole representing a small circular DET specimen with diameter ϕ. Compliant electrodes are located at the corresponding sites on top and bottom of the DE material. Adhesive copper strips are used to connect the compliant electrodes of the DET specimens to the main circuit of experimental set-up. A passivation layer (made with the tape VHB 4910) is placed on top of the plastic frame to isolate the HV electrodes of the DET specimens to prevent undesired discharges and electrocution, also as a protective cover against debris to fall onto the specimens.

5.2.1 Styrenic rubber membrane

Material description

THERABAND YELLOW 11726 is originally used as resistance band for exercising. Thus, the material has excellent mechanical performance. They are also cost-effective: a roll of 23m cost 70$. The considered styrenic rubber membrane comes in rolls with a thickness of about 250 µm and a width in the range of 90 mm to 110 mm depending on the production lot. Through measuring with a Mitutoyo Digimatic Micrometer, the exact thickness in the central test area for the roll of Styrenic rubber have thickness variation of about $\pm 5\%$. Styrenic rubber has been shown in Chapter 4 to have better dielectric strength, lower conductivity and possibly lower water absorption comparing to the OPPO BAND natural rubber. All these characteristics make it a promising candidate for DET applications. Thus, in lifetime characterization tests, styrenic rubber have been chosen as the DE material for the specimens.

Figure 5.8. A roll of THERABAND YELLOW 11726 with length of 25 yards (23 meters).

Specimen preparation

For styrenic rubber DET specimens, the frame plates are made of Delrin® D150 and are laser-cut according to the sketches shown in Fig. 5.9, with two pictures of finalized specimens shown in Fig. 5.10. Fig. 5.9a and Fig. 5.10a present a batch of 8 specimens with hole diameter $\phi = 25mm$, while Fig. 5.9b and Fig. 5.10b present a single specimen with hole diameter $\phi = 50mm$.

Tapped holes are scattered evenly along the edges of the frames for applying M3 screws on the lower plastic plates. The styrenic rubber membrane will be firstly marked with a rectangle that is a downsize shape of the plastic plates. The downsize shape has a proportion ratio equal to the desired pre-stretched ratio. An equi-biaxial pre-stretch ratio equal to 2.6 is chosen to all styrenic rubber DET specimens considered in this work. The membrane will then be pre-stretched through wrapping on the screws. When the marked rectangle on the membrane coincides the edges of plastic frame, the membrane will be pressed onto double-sided tapes (not shown in Fig. 5.7 and placed in between the plastic frame plates and membrane beforehand) to prevent the membrane from losing its pre-stretching during the experiments, especially after electrical breakdown of some specimens. Certain tapped holes on the upper plates will be used also as the connection joints between the copper strips and the HV relays in the main circuit.

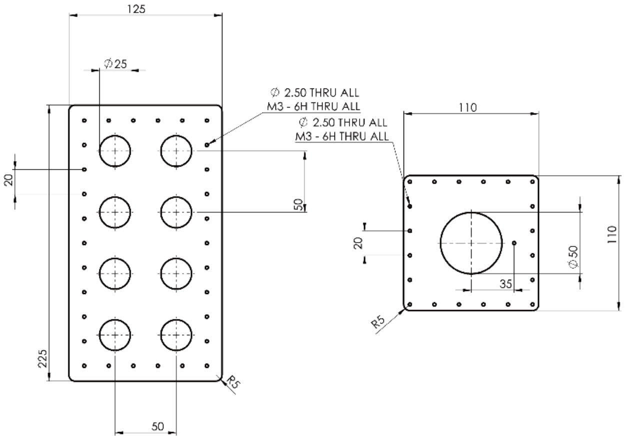

(a) (b)

Figure 5.9. Schematics of the frame plates for styrenic DET specimens with two different hole diameters: (a) $\phi = 25mm$ and (b) $\phi = 50mm$.

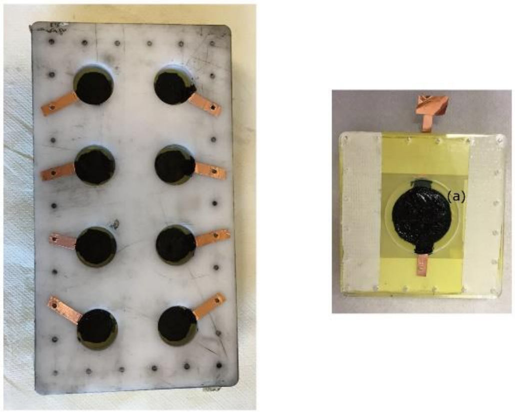

(a) (b)

Figure 5.10. Pictures of prepared batches of styrenic DET specimens with two different hole diameters: (a) $\phi = 25mm$ and (b) $\phi = 50mm$.

Carbon conductive grease (MG Chemicals® 846-1P) is used as the compliant electrodes for styrenic rubber specimens. The carbon grease is manually applied onto the DE membrane at the electrode site. Three different electrode configurations are considered for styrenic DET specimens:

- Free-expanding (Fig. 5.11a): DET specimens with circular carbon grease electrodes which are identical on both sides. The electrode diameter ϕ_e is smaller than the frame hole diameter ϕ. When electrically activated, the DET specimens can freely deform in-plane as expansion, and out-of-plane as wrinkle. The membrane thickness will be inhomogeneous and generally reduced within the electrode area due the compressive Maxwell stress, hence the electric field in the electrode area will be enhanced. For the two different sizes of frames, electrode diameters are chosen as $\phi_e = 20mm$ for $\phi = 25mm$, and $\phi_e = 40mm$ for $\phi = 50mm$;

- Perimeter-locked (Fig. 5.11b): the electrode configuration is similar to the Free-expanding ones, except that the electrode diameter ϕ_e is equal to the frame hole diameter ϕ. When electrically activated, the in-plane expansion on the boundary of the electrode is limited. But out of plane deformation is still allowed. The inhomogeneous and reduction in thickness within the electrode area are thus attenuated compared to Free-expanding ones;
- Surface-locked (Fig. 5.11c): the electrode configuration has $\phi_e = \phi$, which is similar to the perimeter-locked ones. But on the ground side, the specimen is supported by a metallic plate with carbon grease. When electrically activated, both the in-plane and out-of-plane expansion are inhibited. The thickness can be assumed as not-changed from initial condition.

In Fig. 5.12, three pictures of practical DET specimens with respectively three different electrode configurations are presented. Fig. 5.12 only shows specimens with hole diameter $\phi = 50mm$ since the difference in the electrode configuration is clearer to observe with larger specimens.

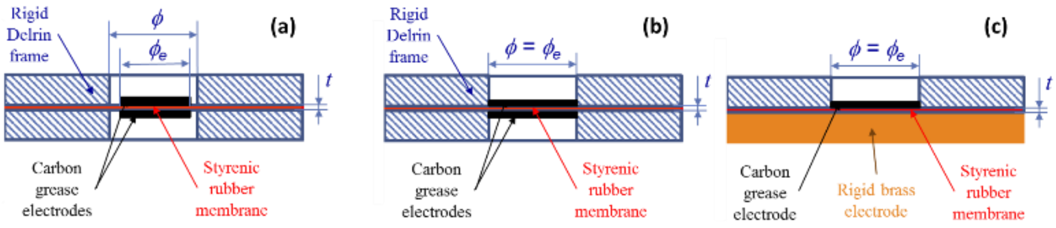

Figure 5.11. Schematics of three different electrode configurations: (a) Free-expanding to maximize area expansion of the specimen when electrically activated; (b) Perimeter-locked to prevent in-plane area expansion of the specimen when electrically activated; (c) Surface-locked to prevent both in-plane and out-of-plane area expansion of the specimen when activated.

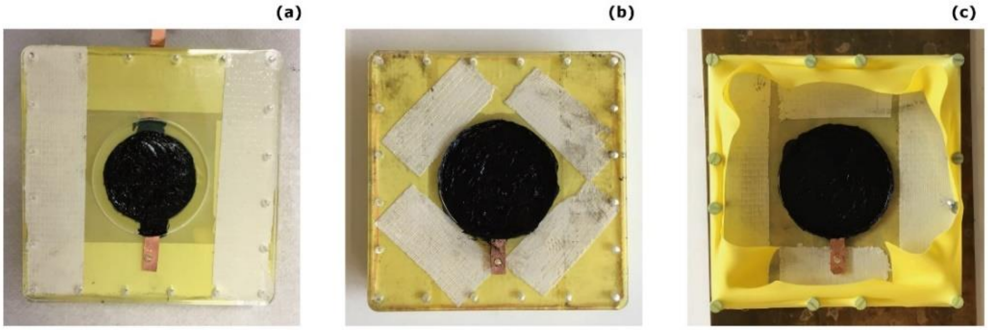

Figure 5.12. Pictures of three different electrode configurations: (a) Free-expanding, (b) Perimeter-locked and (c) Surface-locked.

5.2.2 Silicone elastomer membrane

Material description

Silicone, also known as polysiloxanes, is a class of polymer composed of repeating units of siloxane. Polydimethylsiloxane (PDMS) is a widely used silicone with methyl groups. Original PDMS has poor mechanical properties thus is usually cross-linked into a silicone elastomer. Silicone elastomer is a promising candidate for DE materials and has already been explored and utilized in the DET research field (as introduced in [2], [62]).

Silicone elastomer generally has good qualities such as material stability (against fire, water etc.), transparency and is non-toxic. Comparing to acrylic elastomer, another common choice for DE materials, silicone elastomer generally has a relatively low viscoelasticity. Wider working frequency range, lower operating power losses and lower heat generation can be achieved with silicone elastomer. In previous work available in the literature [63], silicone and acrylic elastomers have been compared for DET actuator application; this comparison has shown that silicone elastomer suffers much less from creeping in strain response.

Another advantage of silicone elastomer is the customizable material characteristics. Silicone elastomer is generally manufactured through addition curing. Common commercial silicones provide two parts of material in viscous base form, with one containing the catalyst and the other one containing the cross linker. The curing procedure involves mixing the two parts according to the product guideline. The requirements for the curing procedure can be loose and easy to achieve, hence the customization on the material can be conveniently validated. During the procedure, additional fillers can be included for enhancing electrical or mechanical characteristic. For example, silicone elastomer generally has relatively low dielectric constant comparing to rubber and acrylic elastomer, which might affect the DET performance as elaborated in Chapter 2. As shown in [2], upon adding a dielectric filler, the dielectric behavior of silicone elastomer can be enhanced. As an example, in [64] the dielectric constant of three-component silicone has been increased from 6 to 8 by adding portion of a titanium dioxide (TiO_2) during the curing procedure. The mechanical characteristic, such as Young's modulus, can also be modified through similar methods. The customization on the electromechanical properties of silicone elastomer increases remarkably the design freedoms in DET system. Since the uncured silicone parts are generally in viscous form, the geometry of the resulting silicone elastomer can also be controlled during the curing procedure. Thus, silicone elastomer can be easily scaled up by manufacturing thicker and larger membranes or can utilize more complex configurations than simple membrane stacking.

By including a conductive filler, the silicone elastomer can also be conductive and be used as compliant electrodes for DET application. The conductive fillers investigated in recent researches are mainly carbon-based nanocomposites because of their outstanding dielectric permittivity [65] and superb electrical conductivity [66]. Typical examples of carbon nanofillers include carbon black (CB) particles [67], carbon nanotubes (CNTs) [68], carbon nanofibers (CNFs) [69], and graphene nanoplatelets (GNPs) [70]. CBs are an amorphous form of carbon with a structure similar to disordered graphite and are the most used in literature as conductive filler mainly because they are cost effective and easy to handle (they do not oxidize as metallic nanoparticles do). A situation of particular interest occurs when the DE layers and the compliant electrodes consist of the same silicone matrix, which simplifies electrode-dielectric assembly (and, thus, the manufacturing of a complete DET device). The use of the same matrix for the different layers in a DET system improves the interface between the insulator and the conductive layers, since the ablation or migration of the electrode material to the DE material during the operation is in this case minimized [71]. This integrity is expected to increase the electrode's operation lifetime. Furthermore, as shown in [72], the dielectric constant of the DET configuration is minimally affected by the compliant electrodes when the electrode composite shares the same nature with the electroactive polymer. However, the conductive filler significantly stiffens the resulting silicone composite [71], which increases the overall stiffness of the DET system, especially when the thickness of the electrode composite is non-negligible comparing to that of the DE layer. Since external mechanical input is not considered in this study, the stiffening effect should have a little influence on the lifetime data obtained here. But for practical DET application, the impact of the stiffness introduced by the electrode layers on system lifetime should be explored.

Commercial silicone elastomers come in various types. As concluded in [2], most of them can be divided into two classes: room temperature vulcanizing rubber (RTV) and high temperature vulcanizing rubber (HTV), where the distinction is based on their curing temperature. As the names suggest, most of them requires a curing procedure. Recently, Wacker Chemie AG has proposed a silicone elastomer product that is commercialized under the name ELASTOSIL® FILM. This silicone composite is an ultrathin, high-precision film of cross-linked silicone rubber that is available in various layer thicknesses, ranging from $20\mu m$ to over $400\mu m$, and is manufactured under clean-room conditions entirely without solvents. Here we choose this product as the DE material for silicone DET specimens based on the following reasons:

(1) It is among the very first commercial products that have been purposely developed for the application of DETs: generally, the already-fabricated silicone elastomers which are commercially available should have better quality and uniformity than custom-prepared silicone layer and suffers less from defects such as micro voids and inclusions due to their matured routine and environment for manufacture procedure. Avoiding the curing procedure also lowers the fabrication requirement in the lab;

(2) It is a silicone-based product that makes it possible to integrate silicone-based compliant electrodes: Wacker also offers general silicone rubber product such as ELASTOSIL® RT 625 which belongs to RTV class. This product comes in two-parts with pourable viscous form and the mixture can be cured at room temperature. The curing procedure is relatively easy to handle and can be adopted to produce compliant electrodes with conductive fillers;

(3) The material's performances are very promising in terms of dielectric constant and electrical break-down limit.

The considered ELASTOSIL® film is available in sheet form and has a product code of 2030 250/150. The film sheets have a dimension of $210mm \times 250mm$ with a thickness of $150\mu m$. The silicone film has a relative permittivity of 2.8 and a dielectric strength in the range of $80\text{-}100MV/m$. For compliant electrode, the base silicone composite is chosen as ELASTOSIL® RT 625 A/B for its ease of handling. The conductive filler is chosen as carbon black (CB) particles for the reasons mentioned previously. Among different CBs we chose the Vulcan XC-72 from Cabot, because it is characterized by a high surface area that, decreasing the gaps between the polymer and the conductive aggregates, allows to reach a high conductivity even at low particle loading.

Specimen preparation

Silicone DET specimens have been prepared by following a procedure proposed for the manufacturing of an inflatable DET generator for harvesting ocean wave energy (reported in [21]).

The holding frames are made of PET plastic and were laser-cut according to sketches shown in Fig. 5.13. In particular, Fig. 5.13a shows the lower frame plate, which is consisting of two parts: the outer ring, on which M3 tapped holes are located and the inner plate, on which the holes for electrode sites are located. As done for the styrenic DET frames, the M3 screws are used as the initial wrapping pivots for applying the equi-biaxial pre-stretch ratio. Pre-stretch ratio for silicone DET specimens is chosen as 1.3. The outer ring and the inner plate are combined at first to be a single PET substrate. The silicone film will then be stretched and wrapped along the M3 screws. No tape is used here to maintain the pre-stretch ratio since the silicone membrane has some intrinsic adhesive effect on the PET frame. A cross has been drawn at the center of the original silicone sheet with predefined dimension to verify the pre-stretching status. Fig. 5.13b shows the upper frame plate. Besides featuring an exact duplication of the electrode sites that match those in the bottom inner plate, the upper frame also provides M4 tapped holes for connecting the specimen batch to main circuits. The cut-off round pieces for electrode sites are not disposed. They are used to fill the holes when the lower inner plate or upper frame plate performs as a flat plane during the electrode printing procedure.

To prepare the compliant electrode composite, firstly the carbon black powder is ball-milled in the Isopropyl Alcohol (IPA) dissolvent (with a weight ratio of $1:10$ and a total weight of $8.8g$) for 15 minutes. This allows to grind the carbon black and makes very small carbon black particle well dispersed into the solvent. Then the ELASTOSIL® RT 625 A/B (with a weight ratio of $A:B = 9:1$ and total weight of $8g$) and another portion of IPA ($8g$) are poured into the ball-milled mixture. This final mixture needs to be ball-milled again for another 15 minutes to reach an evenly stirred state that is necessary in addition curing of ELASTOSIL® RT 625. The final product is the electrode composite and is applied to the silicone film following the procedure shown in Fig. 5.16.

Only free-expanding electrode configuration is considered for silicone DET specimens, with the electrode diameter $\phi_e = 20mm$ and the hole diameter $\phi = 25mm$. The upper electrode patterns are printed firstly, thus in Fig. 5.16a the PET substrate is firstly consisting of the lower inner plate and outer ring as introduced previously. The utilized masks for lower and upper electrode patterns are shown accordingly in Fig. 5.14a and Fig. 5.14b. The masks have partial outline coinciding with the lower inner frame for aligning the masks and the PET frames. Once all the layers have been properly aligned and placed onto a flat surface, the electrode mixture is poured onto the electrode sites as shown in Fig. 5.16b. The electrode mixture is then blade-casted over the masks as shown in Fig. 5.16c. The excess of electrode mixture is then removed alongside with the mask, leaving only the mixture with electrode patterns on the silicone film for curing. The curing of the electrode composite is accomplished in about 12 hours at ambient temperature. After the curing procedure, the configuration is flipped over and placed onto the upper frame plate. Now with the upper frame plate as the PET substrate, the lower inner plate is removed and replaced by the mask for lower electrode patterns, the procedure is then repeated from Fig.5.16a to Fig. 5.16c for printing the lower electrodes, as shown in Fig. 5.16d. An example of final assembly is shown in Fig. 5.16e, the additional areas are for connecting the electrode to copper strips, which then link the electrodes to the main circuit. After the electrodes have been cured and firmly bonded to the silicone film on both sides, all frames are assembled together with clamps to maintain the pre-stretch ratio of the silicone film. Several batches of silicone DET specimens during the preparation are pictured in Fig. 5.15a, while an example of a final batch is shown in Fig. 5.15b.

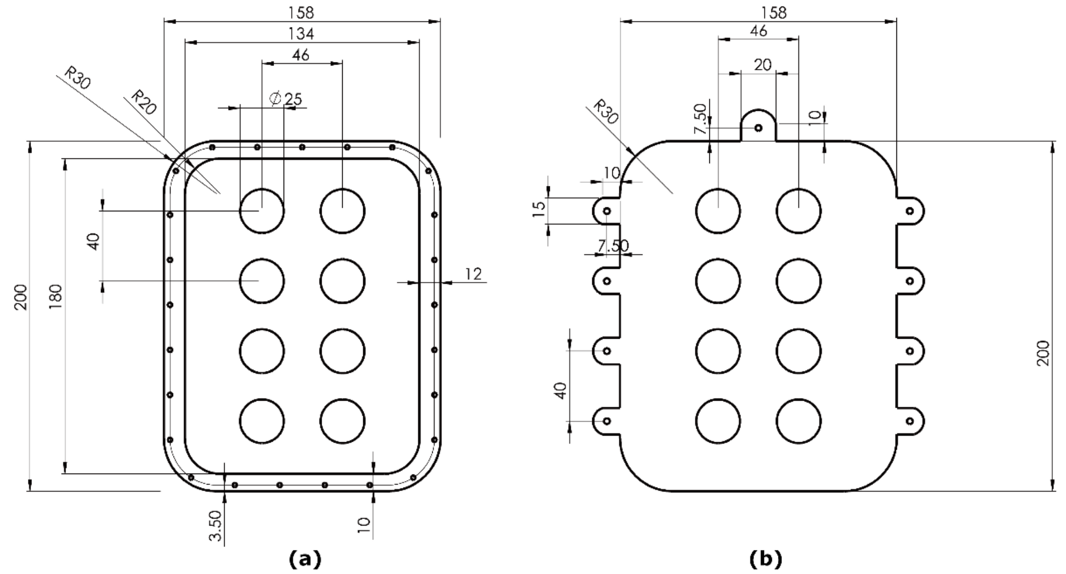

Figure 5.13. Schematics of the frame plates for silicone DET specimens with hole diameters $\phi = 25mm$: (a) lower frames, (b) upper frame

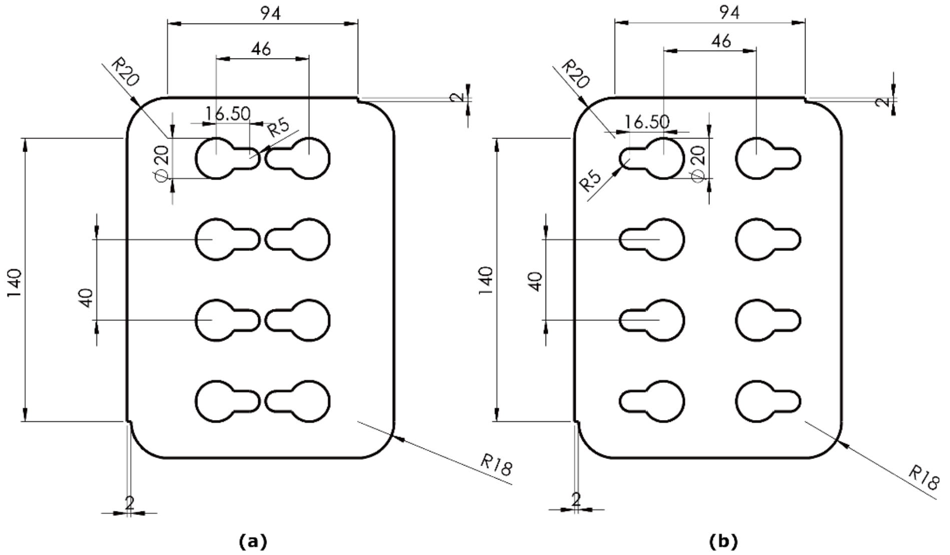

Figure 5.14. Schematics of the printing masks for silicone DET specimens with electrode diameters $\phi_e = 20mm$: (a) mask for lower electrodes, (b) mask for upper electrodes.

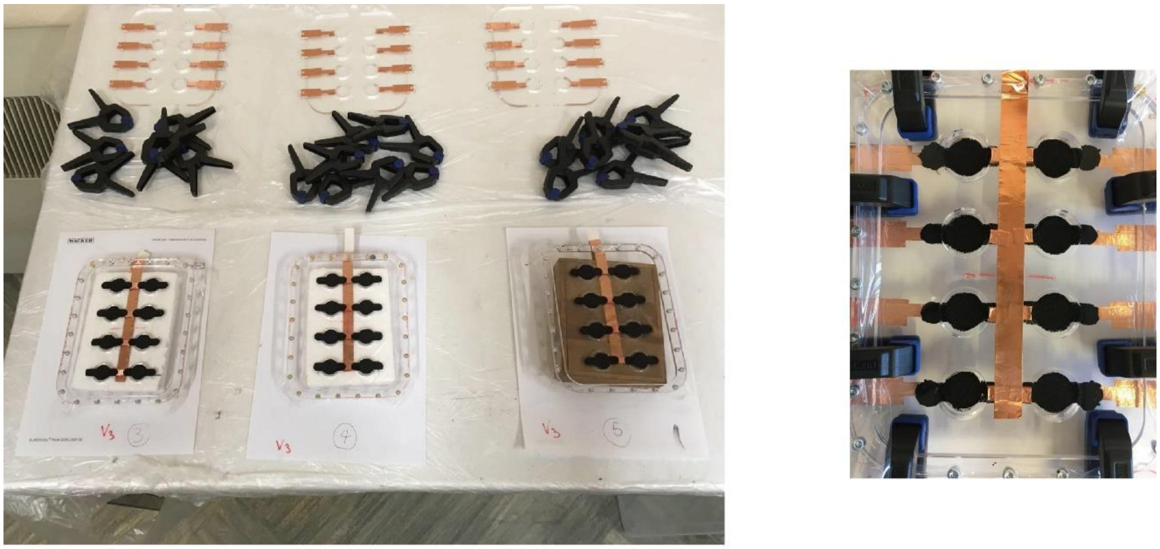

(a) (b)

Figure 5.15. Pictures of (a) several batches of silicone DET specimens under preparation and (b) a finalized batch of silicone DET specimens.

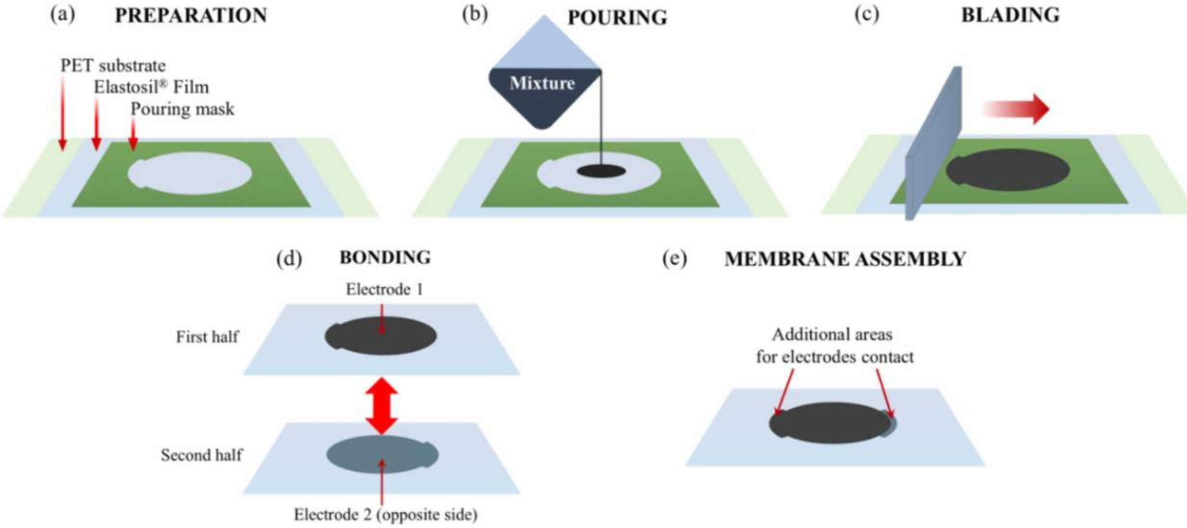

Figure 5.16. Phases of the preparation for silicone based compliant electrodes: (a) align the printing mask and silicone Film onto PET substrate, (b) electrode mixture is poured on the site of electrode holes; (c) electrode mixture is then blade-casted over the masks; (d) the excess of electrode mixture is removed alongside with the masks, and the electrode mixture that left on the silicone film is cured under ambient condition. Once the bonding is finished, the silicone film is flipped over and phases (a)-(c) is repeated for printing the lower electrode pattern; € a final assembly of the printed upper and lower electrodes with additional areas for copper strip to connect.

5.3 Control strategy

Since the experimental setup is designed to perform fatigue lifetime tests, the setup itself should be ensured to last longer than the tested specimens. The experimental setup is generally under high-voltage condition, the control of the setup should thus be cautious during the test operation to avoid shortening of equipment's lifespan or critical device damage. So far the implemented test benches have already been running for more than 1000 hours without problems.

As will be shown in the following sections, the control logic of the circuit is highly dependent on the time and event of the test operation. The Beckhoff industrial system is utilized here for controlling the operation of the experimental setup. Beckhoff TWINCAT3 software system executes instances of TcCOM (TWINCAT Component Object Model) modules in real-time on controllers or compatible PCs. With the help of TWINCAT System Target File, MATLAB®/Simulink® model can be transformed into Microsoft Visual Studio C++ project for generating the associated TcCOM module. Based on these observations, the control logic can be realized as a state machine within a Simulink® model using MATLAB®/Simulink® Stateflow tool. Then the model can be imported as a TWINCAT3 runtime module and executed in real-time to control the experimental setup. During the execution, certain parameters (such as the amplitude of the testing electric field) of the runtime module can be modified through the external mode of Simulink or through TWINCAT3 environment. The real-time signal monitoring can be achieved through Scope block in Simulink or through TWINCAT3 Measurement environment. Thus, the runtime modules can be executed independently in TWINCAT3 environment without MATLAB®/Simulink®, for example on a stand-alone Beckhoff EPC with only Runtime licenses installed. This enables the possibility to replace the high-performance IPC with a cheaper EPC. Engineering licenses (such as TE1400) need only to be installed on the IPC, hence lowering the cost in implementing multiple test benches.

The functionalities of the Simulink model for controlling the experimental setup can be divided into two groups:

- Signal I/O and archiving: for handling the circuit monitoring and commanding signals, and logging of lifetime information during the tests;
- Control logic: for generating commanding signals for proper operation of the experimental setup.

Signal I/O and archiving are straightforward and thus will not be introduced here. For the control logic, the state machine's diagram is shown in Fig. 5.17. A pulse-wave signal (50% duty cycle) is working as the triggering event (either edge) for the state machine, also as a clock event for synchronizing between the real-time execution in TWINCAT environment and the temporal control in Simulink.

The test operation will start when *Enable* signal is received, the state machine will then enter the *Normal Operation* state. Whenever a specimen is failed or *Disable* signal is received, the test system will be paused and transit to *Discharge Operation* state for discharging any remaining charges both on DET specimens and the HV converter. The *Enable*/*Disable* signal can be configured manually or sent by the logic functions. After *Discharge Operation* state, if failure has been detected, the system will enter the *Identification and Isolation* state to identify the failed specimens and isolate them from the remaining test operation. Or if it is a pause action, the system will go back to *Start* state waiting for further instruction. Once all the DET specimens on one batch failed, the test operation will stop completely.

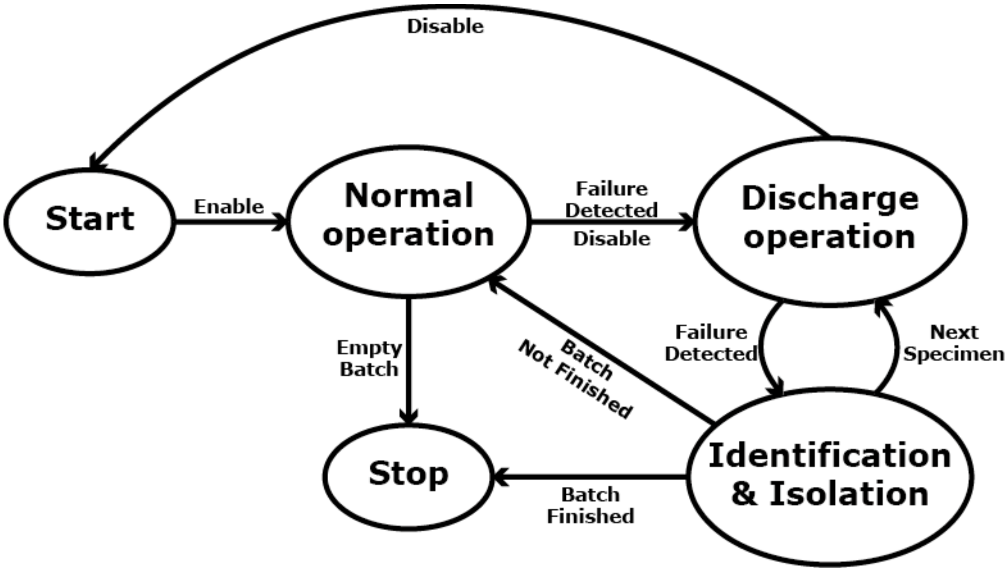

Figure 5.17. State diagram for the control logic.

A simple *Event* function in the control logic will constantly examine the temporary history of the received current and voltage monitoring signals. Based on the status of the circuit, the function will send the corresponding triggering events to the control logic for state transition. The *Event* function will be configured empirically for different test conditions and different types of DET specimens.

Normal operation

In the *Start* state, the list of to-be-tested specimens will be transformed into arrays for commanding the correspondingly the relay array $S_{1\ldots n}$. The list is defined according to the test plan and the continuation of the previous tests.

During the *Normal Operation* state, as introduced in previous sections, square-wave electric field waveform with 50% duty cycles is applied to the DET specimens. In practice, the HV converter is controlled in voltage and the square-wave waveform is ensured only for the nominal electric field. The discharging relay S_D and the switching relay S_C should operate in phase with the voltage square-wave signal to ensure correct charging and discharging phases. The controlling of the relays and commanding signals to generate the required square-wave voltage waveform is shown in Fig. 5.18.

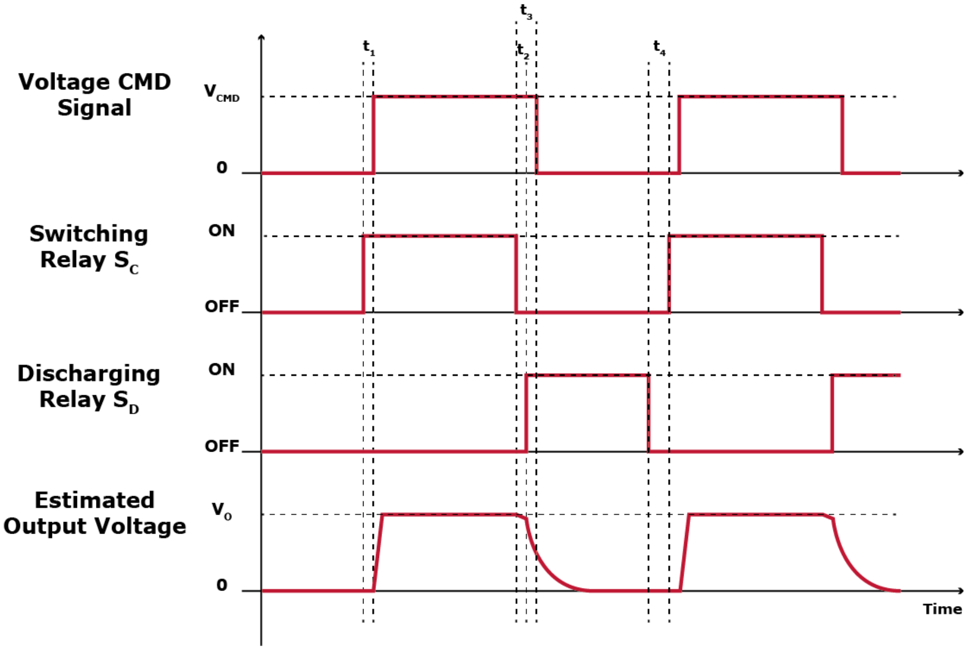

Figure 5.18. Waveforms of several commanding signals that working in phase for correctly manipulating the circuit.

In Fig. 5.18, four delays indicated as t_1, t_2, t_3 and t_4 are introduced. The voltage commanding signal is delayed from the turn-on and turn-off of relay S_C by t_1 and t_3 to avoid the switching of relay during high voltage difference. With delays t_2 and t_4, charging relay S_C and discharging relay S_D are guaranteed not to be turned on simultaneously. In addition, t_4 should also ensure that during the turn-on of S_D, the DET specimens can be discharged completely. A demonstration voltage waveform is shown at the bottom axis. The voltage will rise to the desired level when the voltage commanding signal is turned on at the beginning of one cycle. After the turn-off of S_C, the voltage will slowly decrease during the delay t_2. This decrease in voltage is due to the voltage divider and the internal current leakage of the DET specimens. Finally, the DET specimens will discharge completely when the discharging route is enabled by S_D. The control signal for S_C is the desired square wave signal with 50% duty cycle. To ensure the output voltage signal has the same shape, the delays should satisfy $t_1 = t_2$. During the tests, the delays are chosen as: $t_1 = 5ms$, $t_2 = 5ms$, $t_3 = 10ms$ and $t_4 = 10ms$.

The nominal electric field can be computed through dividing V_{out} by the DE membrane thickness, which is either measured in the inactive state for styrenic rubber or use directly the thickness indicated in the datasheet for ELASTOSIL® film.

The endured lifetimes for the DET specimens are recorded during the *Normal Operation* state. A counter is reserved to accumulate as the square-wave voltage waveform propagates. The counting triggers whenever the voltage rises from zero to desired level and maintains for more than ¼ of the signal period. This triggering condition is handled by the *Event* function. The counter will be archived and paused whenever the system exits the *Normal Operation* state.

The exit of the *Normal Operation* state happens when electrical breakdown is detected, or the test needs to be suspended. The electrical breakdown in DET specimens will form conductive paths through the DE membrane, thus failed DE specimens will short-circuit the experimental setup. The current will eventually be limited by the charging resistor R_C as introduced in Section 5.1. But certain resistors, such as R_C, have relatively low rated power and are only suitable when the circuit is simply charging or discharging. To avoid operating the circuit at full output power under high voltage for a long time, the test should be paused immediately after the detection of short-circuit. The main difference between normal operation (charging) and short-circuit is the duration of peak current level. The theoretical total capacitance of a batch of eight silicone DET specimens with $1cm$ radius is roughly $700pF$, together with charging resistor R_C as $850k\Omega$, the time constant of charging is below $1ms$. Thus, the triggering condition for detecting short-circuit is chosen as: whenever the high-current state lasts more than $50ms$ during the test operation. Once short-circuit detected, *Event* function will send *failure detected* event to the state machine, and the control logic will then transit to the *Discharge operation* state. *failure detected* event will be reset after the finishing of the *Identification and Isolation* state.

Discharge operation

The *discharge operation* state is consisting of the following steps: firstly, relay S_C is turned off to separate the specimens from the HV converter. Then the Voltage CMD signal is turned off and the discharging relay S_D is turned on to discharge the remaining charges held in the circuit. After 1 second of discharging, all relays will be turned off, including relay array $S_{1 \dots n}$.

Identification and Isolation

After the discharging of the circuit, if *failure detected* event was received, the control logic will traverse the list of tested specimens to find the failed ones. An identification voltage is applied to the tested specimen. This voltage is chosen to be lower than the test voltage and assumed to be harmless to the specimen. If the tested specimen is still alive, the identification voltage will last for $500ms$ and then entering the *Discharge operation* state. While if the tested specimen is failed, the *Event* function will detect the short-circuit again and notify the control logic to isolate this specimen. The corresponding relay in the relay array will be turned off permanently and this specimen will be eliminated from the list. The number of the failed specimen will be archived, together with the paused counter which indicates the endured lifetime for the failed specimen. The same procedure is repeated until all the specimens on the list have been examined. Finally, the to-be-tested list will be updated based on remaining specimens, the test will be continued or terminated according to this updated list.

If no specimen was found during the *Identification and Isolation* state, *Disable* signal will be sent, and the test will be suspended for further inspection.

5.4 Results on styrenic rubber

In this section, lifetime results on styrenic DET specimens will be presented and discussed. Four sets of experiments have been performed to assess the lifetime characteristics under different electrode configurations and electrical loading profiles. In particular, they have considered the effect of:

- Different nominal electric field amplitudes;
- Different electrode configurations as introduced in Section 4.2.1. Since electrode configurations mainly affects the mechanical expansion of the DET specimen during the on-state of the applied electric field, hereafter the electrode configurations might also be referred as "mechanical constraints";
- Different frequencies for the square-wave electric field waveform;
- Different DET specimen sizes.

The results and analysis have also been reported in [47] and [48] .

5.4.1 Lifetime vs electrical field amplitude tests

To assess the influence of the amplitude of the applied electric field on lifetime, three batches of 16 identical DET specimens have been tested. The mechanical constraints for these specimens were perimeter-locked with diameter $\phi = 25mm$. The applied square-wave electric field waveforms have a duty cycle of 50%, 1 Hz frequency and the following different amplitudes:

- $70.3MV/m$ (for the first batch);
- $100MV/m$ (for the second batch);
- $127MV/m$ (for the third batch).

The obtained lifetime and the corresponding cumulative failure probability data (estimated via Eq. 3.22) are reported in Fig. 5.19a and Fig. 5.19b. Based on these obtained data, the Weibull model (described in Chapter 3 as Eq. 3.13, 3.17, 3.20 and 3.21) can be fitted and presented as straight lines in Fig. 5.19a, with the corresponding MCTFs plotted in Fig. 5.19b. The corresponding 95% confidence curves are also plotted as dashed lines in these figures. The corresponding Weibull parameters resulting from the MLE estimator fitting procedure are listed in Table 5.1.

Inspection on the obtained experimental data and the fitted straight lines reveals that the proposed Weibull model incorporated with electrical loading is capable to capture the dependency of DET lifecycles on the applied electric field amplitude. Since the applied electric field amplitude directly correlates with the level of performance achievable by the DET application as introduced in Chapter 2, this model can also be considered capable to describe the relationship between the reliability and the performance of the DET configurations. In particular, Fig. 5.19a shows that the proposed Weibull model incorporated with electrical loading provides a good fit on the obtained failure data, since most of the obtained lifetime data fall within the 95% confidence bound curves at the corresponding percentiles. Fig. 5.19b shows that the Weibull MCTF curve described by Eq. 3.21 is capable to capture the general trend of the experimental failure data. Note that the approximated 95% confidence curves reported in Fig. 5.19b represent the mean lifetime, rather than for all the experimental data, will fall within those bounds with a probability of 95%. Hence, the boundary curves in Fig. 5.19a can be reckoned as prediction ranges for DET lifetime under a given amplitude of electrical loading and percentile. While boundary curves in Fig. 5.19b can be reckoned as a prediction range for mean DET lifetime under a given amplitude of electrical loading.

From the parameters in Table 5.1, the characteristic lifetime $N_C = \alpha(E) = \frac{\exp(a_1)}{E^{a_2}}$ decreases ($a_2 > 0$) whereas the shape parameter $\beta = a_3 - a_4 \log E$ increases ($a_4 < 0$) as the electric field amplitude is increased. This can be observed in the figures as the decreasing trend of lifetime data points and the increasing of slopes of fitted straight lines, when the applied electric field increases.. This observation, while confirms the hypotheses behind Eq. 3.13 and 3.20, is quite intuitive: increasing the electrical loading amplitude is expected to reduce generally the lifetime and increase the rate of failure. But notice should be made that the decrease in N_C is far more drastic than the increase of β, i.e. the dependence on the field amplitude for characteristic lifetime is more evident than failure rate. The necessary of parameters a_3 and a_4 in the proposed Weibull model should be explored more detailly. Additional tests with more levels of electrical loading will be conducted in the future.

From a lifetime testing perspective, this result also indicates the significance of testing the specimens in laboratory environment at electric field amplitudes that approach the intrinsic dielectric strength of the DE materials, even though in general the applied electric field amplitude in practical operative conditions are relatively small compared to the dielectric strength. In this way the fatigue tests can be accelerated so as to reduce the testing times and costs, while the obtained model parameters are still viable for DET design.

Electric Field [MV/m]	Weibull parameters					
	N_C	β	a_1	a_2	a_3	a_4
127	1121	3.19				
100	2771	2.64	25.35	3.7842	-2.65	-0.78
70.3	10685	2				

Table 5.1. Fitted parameters for model Eq. 3.13, 3.17, 3.20 and 3.21 based on the obtained lifetime results from electrical field amplitude tests.

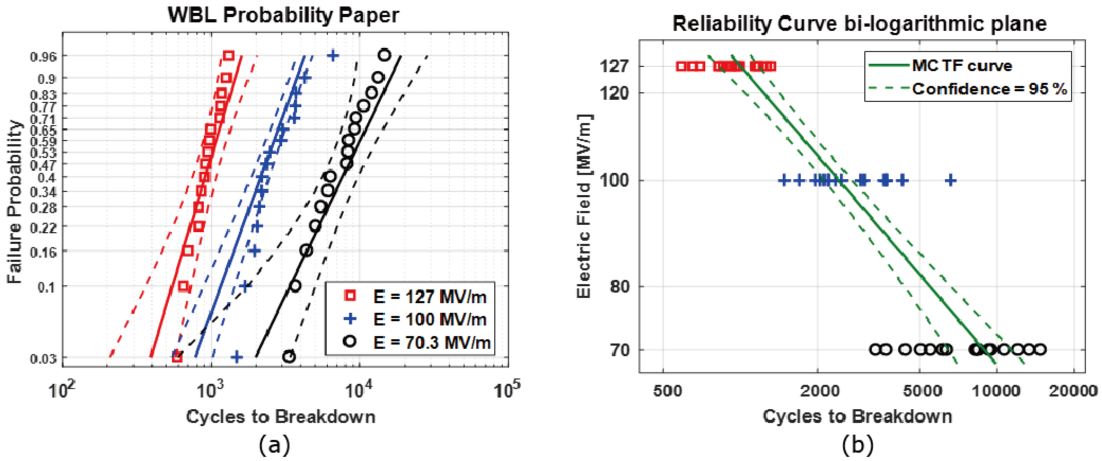

(a) (b)

Figure 5.19. Lifetime results obtained from electrical field amplitude tests and the fitted distribution models plotted in: (a) Weibull probability paper, with 95% confidence curves in lifetime as dashed lines, the fitted Weibull model as the straight lines and the obtained lifetime data as different markers; (b) bi-logarithmic plane, with fitted MCTF as solid line and the confidence curves of MCTF as dashed lines.

5.4.2 Lifetime vs mechanical constraint tests

To assess the influence on lifetime of the different types of kinematic constraints applied via different electrode configurations, three different batches of DET specimens all with frame hole diameter $\phi = 25mm$ have been tested. All three batches have been tested under the same electrical loading as square wave electric field waveform with 50 % duty cycle, 1 Hz frequency and $100MV/m$ nominal amplitude, but with the following different mechanical constraints:

- Free-expanding (for the third batch), as in Fig. 5.11a with $\phi_e = 20mm$;
- Perimeter-locked (for the second batch), as in Fig. 5.11b;
- Surface-locked (for the first batch), as in Fig. 5.11c.

The obtained lifetime data are reported in Fig. 5.20a. Comparison of the obtained failure data and the fitted Weibull models is instead reported in Fig. 5.20b. In this case, since no simple explicit relation can be included within the Weibull model that correlates the mechanical constraint type and lifetime characteristics, the fitting of the experimental data is performed on each of the three batches independently through the standard two-parameter Weibull model (Eq. 3.17). The corresponding estimated Weibull parameters are listed in Table 5.2.

From Table 5.2, the characteristic lifetime $N_C = \alpha$ increases as the level of mechanical constraints decreases (from surface-locked to free-expanding case). At a first sight, this observation is rather counterintuitive. With the DET specimen less constrained, the DE membrane will expand in area once activated. Its thickness becomes not uniform due to the incompressibility of the DE material: specifically decreasing at the center and increasing at the periphery. This follows the actual electric field values at the center are higher than the nominal electric field. This local enhancement of electric field should thus lead to a failure earlier than the case where DET specimens' deformation are constrained and the practical electric field levels are less different from the designed nominal one.

However, the increase in lifetime might be explained by considering that DETs are suffering from electric field singularities (fringing effect and the presence of air as the additional dielectric medium) at the electrode's boundary. This electric field singularities might introduce higher local electric field level than the nominal one. Since the DET area expansion causes the thickness to shrink from electrode periphery to center, it is likely that the thickening of material at the electrode boundary reduces the maximum amplitude of the singular electric field. An evidence in favor of this conjecture comes from the visual inspection of the broken specimens, which highlights the following:

- The breakdown spots on the surfaced-locked and perimeter-locked DET specimens are almost always at the border, indicating high electric field located at the boundary;
- The breakdown spots on the free-expanding DET specimens are mostly in the specimen bulk, indicating the high electric field concentrations at the boundary might be inhibited and possibly now the local electric field enhancement within the specimen bulk due to the decrease of thickness has prominent effect on the reliability.

Differently from N_C, the shape factor β does not seem to change significantly with varying types of mechanical constraint, even though β seems to increase as the level of mechanical constraint decreases. The estimated 95% confidence boundaries for the estimation of the β for each mechanical constraint are highly overlapping: $(2.57, 7.43)$, $(2.27, 6.01)$ and $(1.9, 5.6)$ for Free-expanding, perimeter-locked and surface-locked respectively. Thus, the differences among the fitted β reported in Table 5.2 for the three test batches are statistically insignificant. This observation indicates that the breakdown mechanism might not be affected by the electrode configurations or the mechanical constraints. The estimated 95% confidence boundaries for the estimation of the α are: $(3958, 5058)$, $(2471, 3325)$ and $(1516, 2156)$ for Free-expanding, perimeter-locked and surface-locked respectively, which are more distinguishable than β. This is similar to the results obtained in the test comparing different amplitude of electrical loading, which indicates that the difference in lifecycle trending (related to α) might generally be more obvious and easier to identify than the rate of failure (related to β) in DET fatigue testing.

	Weibull parameters	
Mechanical constraint types	N_C	β
Free expanding	4508	5
Perimeter locked	2898	4.14
Surface locked	1836	3.75

Table 5.2. Fitted parameters for model Eq. 3.17 based on the obtained lifetime results from mechanical constraint tests.

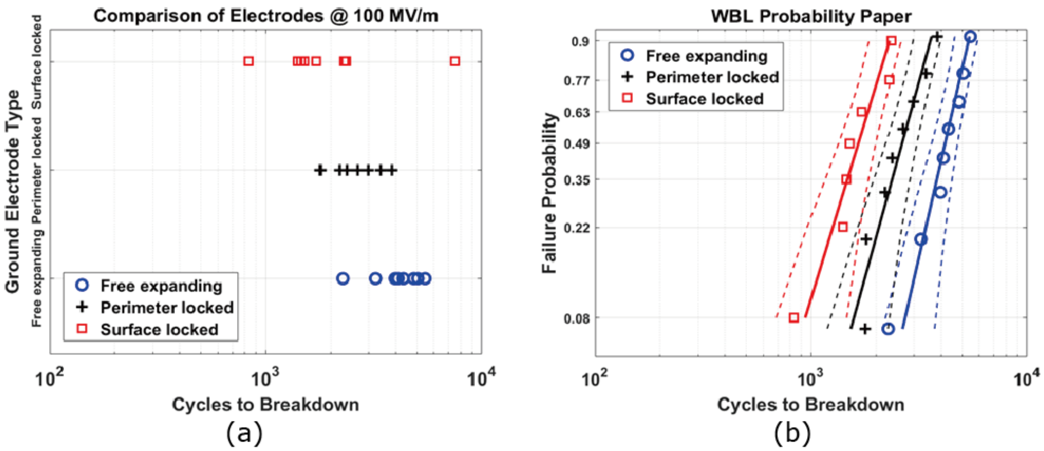

Figure 5.20. Lifetime results obtained from mechanical constraint tests and the fitted distribution models plotted in: (a) log scale of lifetime; (b) Weibull probability paper, with 95% confidence interval in lifetime as dashed lines, the fitted Weibull model as the straight lines and the obtained lifetime data as different markers.

5.4.3 Lifetime vs electrical loading frequency tests

To assess the influence of the frequency of the applied electric field square waves on lifecycle, three batches of identical DET specimens with free-expanding electrode configuration (with hole diameter $\phi = 20mm$ and electrode diameter $\phi_e = 20mm$) have been tested, with the electric loading as square wave electric field waveform with 50 % duty cycle, $100MV/m$ amplitude and the following frequencies:

- 0.2 Hz (for the first batch);
- 0.5 Hz (for the second batch);
- 1 Hz (for the third batch).

The obtained experimental lifetime data are reported in Fig. 5.21a. Comparison of the obtained with the Weibull CDF fitting is instead reported in Fig. 5.21b. As introduced in Chapter 3, the fitting of the experimental data considering different frequencies is performed on each of the three batches independently with the two-parameter Weibull model Eq. 3.17. The corresponding Weibull parameters estimated from the data fitting procedure are listed in Table 5.3.

As Fig. 5.21b shows, though the characteristic life N_c of each batch are different from each other, the confidence curves for lifecycles at different percentile are highly overlapped. This means the lifetime seems to exhibit a weak dependence on the electrical loading frequency; which is in contrary with the standard Weibull model that is described in normal time unit: it indeed indicates that the failure probability does not strongly correlate with the time for which the specimen is kept electrically active (that is, electrically stressed), but rather with the number of times it switches from active to inactive and vice-versa. Thus Eq. 3.16 and Eq. 3.17 do not convey the same information and it is not straight-forward to pass from one form to the other, Eq. 3.19 is indeed not suitable for describing lifetime for styrenic DET specimens. The postulate that describing the lifetime in unit of cycle might be more suitable for DET system.

This result suggests that charging and discharging phases may have a major effect in damage accumulation. In particular, since the presence of inevitable Joule heating caused by current during charging and discharging due to the non-negligible resistance of the DET electrodes, the degradation in the DET specimen which leads to final breakdown may be driven prominently by thermal effects rather than by electromechanical, electronic or partial discharge.

From a lifetime testing perspective, this result also indicates the significance of testing the specimens in laboratory condition with frequency higher than those used in operative conditions, for accelerating the lifetime tests to reduce testing times and costs. While the obtained lifetime characteristics are still viable since the frequency might have minor effect on the fatigue characteristic.

As regards the shape parameter β, Table 5.3 show that there seems no specific relationship between β and the operation frequency. Additional tests including a larger number of specimens are needed in exploring the correlation between the rate of failure and the operating frequency.

	Weibull parameters	
Frequencies [Hz]	N_C	β
0.2	9497	1.45
0.5	7055	2.46
1	6666	1.57

Table 5.3. Fitted parameters for model Eq. 3.17 based on the obtained lifetime results from electrical loading frequency tests.

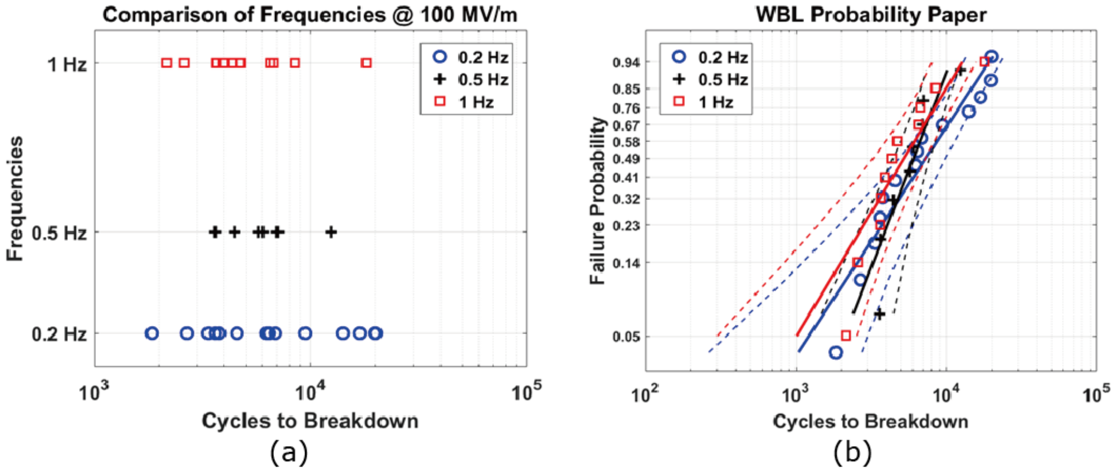

Figure 5.21. Lifetime results obtained from electrical loading frequency tests and the fitted distribution models plotted in: (a) log scale of lifetime; (b) Weibull probability paper, with 95% confidence interval in lifetime as dashed lines, the fitted Weibull model as the straight lines and the obtained lifetime data as different markers.

5.4.4 Lifetime vs specimen size tests

Knowledge about the correlation between lifetime characteristics and DET specimen size is necessary for assessing the scalability of the technology and predicting lifespan of full-scale service DETs from results obtained on small-size DET specimens tested in limited laboratory spaces.

To investigate this aspect, DET specimens with free-expanding electrode configuration and different sizes are prepared and tested with square wave electric field waveform featuring 50 % duty cycle, 100 MV/m amplitude and 1 Hz frequencies.

So far, due to the lack of materials and associated equipment, only preliminary results have been obtained for this kind of tests:

- Only two different frame hole sizes ϕ have been considered, 25 mm and 50 mm, with the corresponding free expanding electrode sizes ϕ_e being 20 mm and 40 mm.
- For the larger size ($\phi = 50mm$) only 4 specimens have been tested.

Although the amount of failure data and the variety of specimen sizes are not statistically sufficient to be fitted with good accuracy to any reliability distribution models, the obtained results are still reported in Fig. 5.22. and have been fitted separately for each batch according to the two-parameter Weibull model Eq. 3.17: though the theoreitical size scaling has been introduced in Chapter 3, the exact correlation still needs to be verified. The fitted Weibull models and the corresponding parameters are presented in Fig. 5.22b. and Table 5.4.

Despite the limited number of tested specimens, it is quite clear that the lifetime increases with the increase of specimen size.

This observation is rather counterintuitive. In fact, since the electrical degradation and breakdown is generally dependent on the weakest point on the material, it is expected that electrical breakdown is more likely to occur in large size specimens due to the higher probability to have defects with larger volumes, surfaces and thicknesses.

As a possible explanation, the ease of manually manufacturing larger styrenic DET specimens may have helped to improve the overall quality of the specimens (namely, more uniform electrode layer, better electrode boundary conditions etc.).

In the future, more extensive tests are going to be performed to explore the correlation between lifecycle and size.

Diameter size [mm]	Weibull parameters	
	N_C	β
25	4508	5
50	14342	2.61

Table 5.4. Fitted parameters for model Eq. 3.17 based on the obtained lifetime results from specimen size tests.

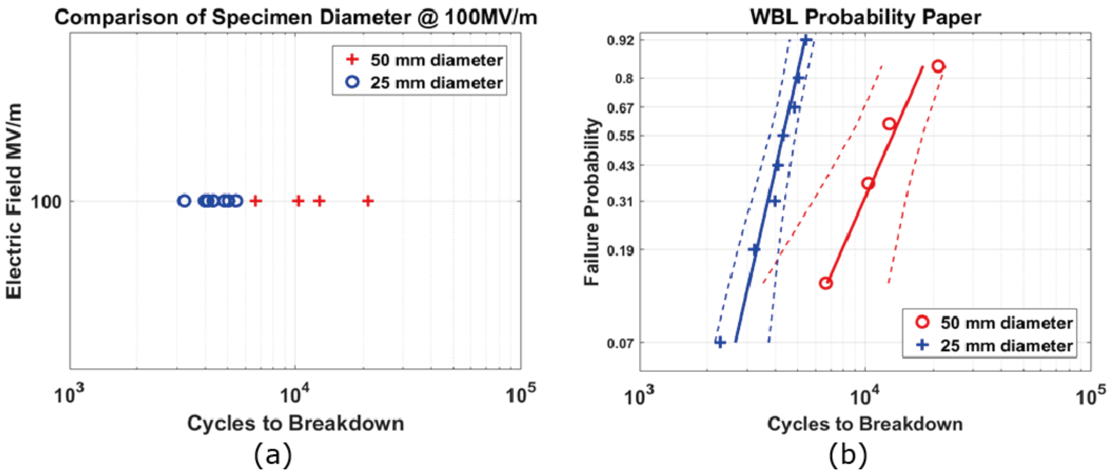

Figure 5.22. Lifetime results obtained from specimen size tests and the fitted distribution models plotted in: (a) log scale of lifetime; (b) Weibull probability paper, with 95% confidence interval in lifetime as dashed lines, the fitted Weibull model as the straight lines and the obtained lifetime data as different markers.

5.5 Results on silicone elastomer

The results reported here for the silicone DET specimens are very promising but only preliminary. At the time of this writing some tests are still ongoing and new tests are being started to investigate this more in depth. During the experimental campaign, some of the tests have been interrupted due to the unexpected failure behaviors that have been observed on a number of silicone DET specimens prepared according to the procedure describe before.

Results on specimens with free-expanding mechanical constraint (ϕ_e = 20mm) under different electric loading amplitudes are shown in Fig. 5.23 with logarithmic scale of lifetime. As can be observed from the figures, several trials with different number of specimens and different electric field amplitudes have been made. Most of the specimens failed and some of them are still under testing.

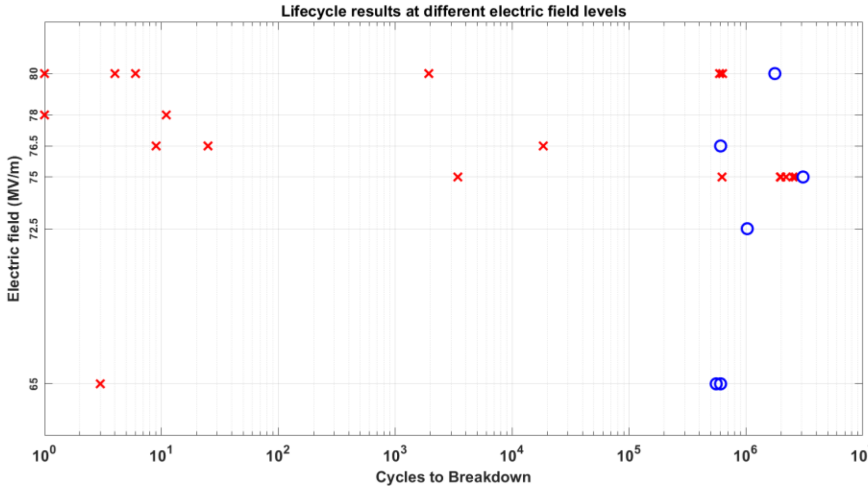

Figure 5.23. Lifetime results of silicone DET specimens so far, presented in log scale in lifetime and linear scale for electric field level. Red cross indicates specimen failure, while circle indicates survived specimens (multiple specimens can have same position as one circle).

Fig. 5.23 shows a clear gap around 10^5 cycles. This gap indicates that silicone DET specimens either lasted near or more than millions of cycles or failed within several thousands of cycles. Possible explanation for this behavior is that the produced silicone DET specimens might not be sufficiently consistent. The inconsistency might due to either the manufacturing procedure, which is inherited from larger size applications (107mm from [21]), or the considered silicone material. From the figure, a gap seems to exist around 10^2 cycles, but since the plotting is in logarithmic scale of lifetime, the gap at 10^5 cycles is much more significant.

Upon observing the failed specimens, three types of specimens have been observed as shown in Fig. 5.24, with red circles indicating the location of breakdown points. In particular:

- Fig. 5.24a represents a silicone DET specimen with lifetime lower than 10^5 cycles. As it can be observed, the additional area of the upper electrode which is responsible for connecting electrodes to copper strips (hence the main circuit) is patterned poorly and an early failure is expected, which is due to the irregular electric field that is likely to be generated in this imperfect region. The breakdown point is also located in this region, though not so obvious to be recognized.

- Fig. 5.24b represents another silicone DET specimen with lifetime lower than 10^5 cycles. The specimen seems fine regarding to the printed electrode pattern, but it still suffers from an early failure. The breakdown point is located again in the additional connection area.
- Fig. 5.24c represents a specimen with lifetime greater than 10^5 cycles. The electrodes seem fine, and the breakdown point is located at the border of the electrode but not in the additional connection area. The breakdown point is clearer to be observed: a melted point is located at the center of the breakdown spot and the surrounding silicone material has become opaque.

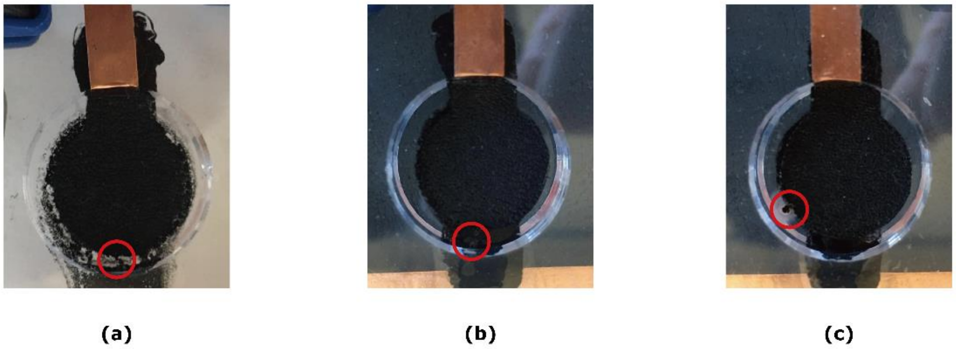

Figure 5.24. Examples of three types of failed silicone DET specimens (all have been tested under similar electric field amplitude), red circles indicate the breakdown points: (a) early failure with bad printing; (b) early failure with not-obvious imperfection; (c) good specimen lasted more than two million cycles and failed.

The poor patterning in the connection area might be due to not-sufficiently stirred electrode mixture or to an excessively slow curing process that prevent the electrode mixture to bond adequately to the dielectric substrate. When the electrode is cured and dried, not enough carbon black is left in this region. The inconsistent conductivity in this zone is likely to generate an irregular electric field, thus leading to an early failure. However, the quality of the electrode is not easy to verify, since as it is shown in Fig. 5.24b, the specimen seems fine but also has an early failure. For a good specimen which has lasted more than 10^5 cycles, the plainness of the breakdown point might indicate that the breakdown is indeed due to the fatigue or degradation mechanisms: the weak point has been stressed sufficiently to change the material properties in the surrounding area.

To verify this observation, six brand-new specimens on two batches are tested firstly under electric field of $65MV/m$ for 50000 cycles; then, those that have survived are tested with an electric field of $80MV/m$ which is in the breakdown range of ELASTOSIL® silicone in unstretched state. One of the six specimen failed immediately with $65MV/m$; for the remaining five specimens, one has failed below 10^5 cycles under $80MV/m$; the rest four has lasted more than 10^5 cycles and the results are shown in Fig. 5.25. This attempt confirms that: 1) there is indeed quality difference among the specimens even on the same batch; 2) the 'bad' specimens are not likely to last longer than 10^5 cycles, but the breakdown electric field levels for the 'bad' specimens are not necessary the same; 3) the 'good' specimens can last easily over 10^5 cycles.

Removing specimens with lifecycles lower than 10^5 (considered as 'bad' specimens) provides Fig. 5.25. Although these data are much less than those available for the styrenic rubber specimens, some statistical analysis can still be done.

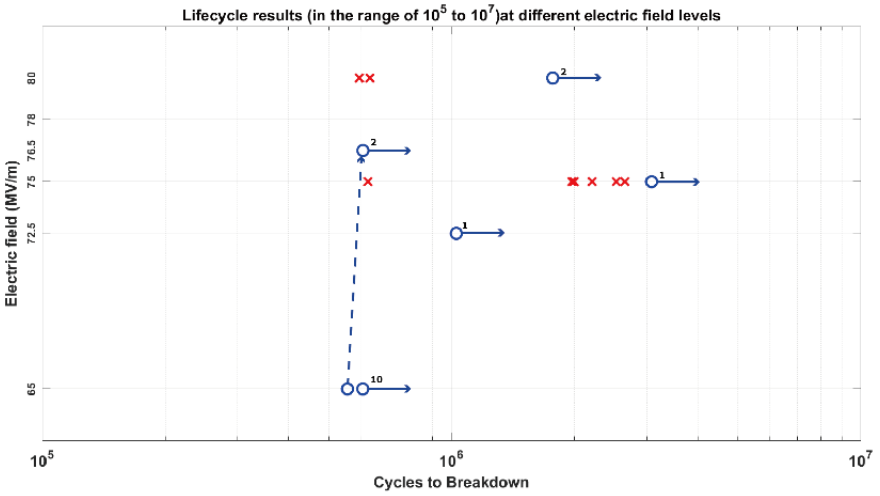

Figure 5.25. Lifetime results of silicone DET specimens greater than 10^5. Red cross indicates failure, circle with right arrow indicates right censored (still alive to date) specimens, small number near the circle indicates how many specimens under the same condition, dotted arrow indicates a change on the applied electric field amplitude.

For the tests conducted at electric loading amplitude of $75MV/m$ (thus, for a DET operating at an energy density larger than $300J/kg$ from [21]), the corresponding Weibull fitting results are shown in Table 5.5 and Fig. 5.26. This test is still ongoing thus the result data is considered as singly-censored. As it can be seen in the figure, the proposed Weibull model can still describe the lifetime characteristic for silicone specimens. From Table 5.5, the estimated distribution model has a characteristic lifetime of more than 2.2 million cycles. This is a remarkable number in the aspect of both performance and durability for DET systems.

Weibull parameters

N_C	β
2204200	3.76

Table 5.5. Fitted parameters for model Eq. 3.17 based on the obtained lifetime results from specimen size tests.

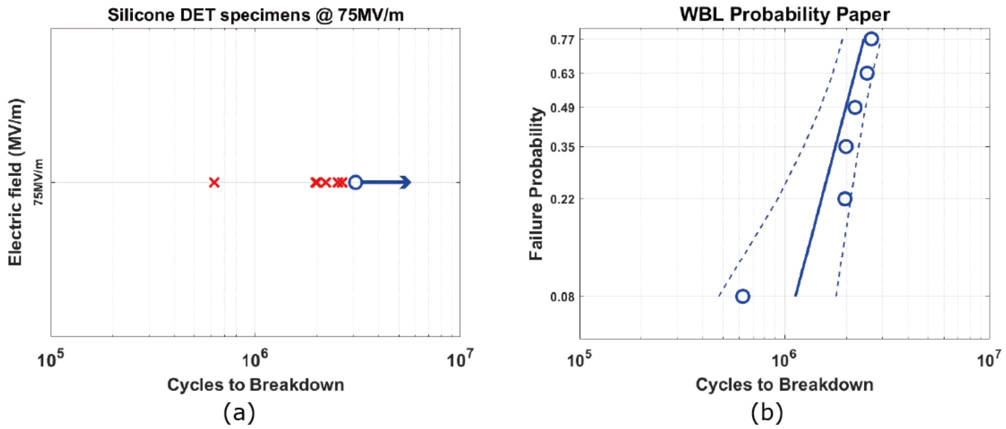

Figure 5.26. Lifetime results for silicone specimens tested under $75MV/m$ and the fitted distribution models plotted in: (a) log scale of lifetime, red crosses indicate failed specimens, circle with arrow indicates the still-alive one; (b) Weibull probability paper, with 95% confidence interval in lifetime as dashed lines, the fitted Weibull model as the straight lines and the obtained lifetime data as circle.

Chapter 6

Conclusion

As DET technology becomes more and more popular, comprehensive understanding on the characteristics of DE materials and lifetime characteristic of DET system are valuable information and worth exploring. So far, there are only a few proposed standards or routines for characterizing DET properties, and even less for DET reliability. In this work, an experimental study has been performed to compare the electromechanical characteristics of several DE materials, and explore the lifetime characteristics of DET systems. Experimental set-ups and methodologies have been designed and implemented based on existing approaches from related fields. Series of tests have been conducted and the obtained results have shown a number of interest insights. We hope that these results can be beneficial for optimizing DET designs, such as suitable choice between different DE materials and compliant electrodes, performance/reliability trade-off etc.

6.1 Electromechanical characterization and comparison for three DE materials

For characterizing DE materials, experimental set-up and procedure have been designed and implemented based on existing standards IEC 60243-1, IEC 62539, ASTM D149, ASTM D257 and ASTM D150. Results have been obtained for three popular DE materials: styrenic rubber, THERABAND YELLOW 11726; natural rubber, OPPO BAND GREEN 8003; acrylic tape, VHB 4905 by 3M.

The obtained electrical characterization results for the three DE materials have shown that:

1) Dielectric strength of the considered DE materials is indeed dependent on the level of applied equi-biaxial strain in a power law. In particular, THERABAND YELLOW 11726 behaves similar to OPPO BAND GREEN 8003 regarding the dielectric strength levels and their dependencies on the strain. THERABAND YELLOW 11726 is more resistant to

water absorption than OPPO BAND GREEN 8003 for dielectric strength. VHB 4095 has the worst dielectric strength among the three materials.

2) Electrical conductivity of the considered DE materials is dependent on the level of applied electric field in an exponential law, which confirms previous findings documented in the literature. In particular, THERABAND YELLOW 11726 has the lowest electrical conductivity among the three materials. The conductivity of OPPO BAND GREEN 8003 is again comparable to THERABAND YELLOW 11726. VHB 4095 has the largest conductivity which is over 10 times larger than conductivity of THERABAND YELLOW 11726. No significant correlation has been observed between electrical conductivity and applied pre-stretch strain, though these tests have been performed only on VHB 4095.
3) Dielectric constant seems to show a weak dependency on the applied strain. VHB 4095 has the best dielectric constant among the three DE materials. While THERABAND YELLOW 11726 has a dielectric constant similar to OPPO BAND GREEN 8003.

The obtained mechanical characterization results for the three DE materials have shown that:

1) Testing strain rate has limited influence on the mechanical response for all the three DE materials in both large and intermediate stroke ranges.
2) Gent-Gent model is capable to describe the observed stretch-stress behavior for all the three DE materials quite accurately. Thus, this model can be a promising candidate to be used in control algorithms and design of DET applications.
3) As OPPO BAND GREEN 8003 is stretched with large strokes, which are close to its rupture strength limit, the mechanical hysteresis loss will increase significantly. The material becomes softer after reaching the maximum deformation level and during the returning to the initial condition. In this case, the returning trajectory on stretch-stress plane cannot be described by the Gent-Gent model.
4) In intermediate stroke case, OPPO BAND GREEN 8003 has the lowest hysteresis loss.

The obtained results for dielectric properties of the three considered DE materials agree mostly with results existing in the literature. Discrepancies between the measured dielectric constant in this work and those in the literature can also be explained, as elaborated in section 4.2.4. Hence, the utilized methodology can indeed correctly measure the associated properties for DE materials. The adoption of a same experimental procedure for the characterization of the three different DE materials makes it possible to compare their performances in a more credible and consistent manner.

Comparing the testing results acquired on the three considered DE materials, one can find that:

1) Though VHB 4095 has the largest dielectric constant among the three DE materials, it suffers from relatively large current leakage and low dielectric strength.
2) OPPO BAND GREEN 8003 performs similar to THERABAND YELLOW 11726 but is rather sensitive to humidity and stroke range.
3) THERABAND YELLOW 11726 has decent dielectric strength and no obvious flaw, hence it can be a promising DE material. Thus, in the lifetime characterization experiments, DET specimens based on THERABAND YELLOW 11726 have been considered.

6.2 Lifetime characterization on DET specimens based on two DE materials

Based on existing practices in power cable industry and accelerated-testing research field, experimental procedures and test benches have been developed for characterizing the lifetime behavior of DET systems. The proposed experimental set-up and procedure can operate autonomously and have already been in operation for more than 1000 hours without encountering any problems. DET specimens based on two DE materials (styrenic rubber, THERABAND YELLOW 11726 and silicone elastomer, ELASTOSIL® 2030) have been prepared and tested under different conditions for thoroughly analyzing the lifetime behavior.

In particular, for styrenic DET specimens, the obtained lifetime results have shown that:

1) Weibull distribution model (in time unit of energy conversion cycle) fits generally well with the obtained lifetime results. Since Weibull model is a well-studied area in stochastic field, the associated theoretical or practical conclusions and methods are available for further exploration on the lifetime performances and reliability prediction of DET systems.
2) The applied electric field amplitude affects dominantly the lifetime behavior of DET systems. The relationship between the applied electric field amplitude and characteristic lifetime α is indeed following the inverse power law introduced in [45].
3) The test results on different electrode configurations emphasize the local enhancement of electrical stress around the boundary of electrode. The discontinuity and singularity at the

boundary of electrode might be a prominent cause in the degradation process of DET systems.

4) Lifetime characterization of DET systems might be better described in terms of number of cycles rather than in terms of elapsed time. This implies that the degradation process of a DET system might be due to the thermal effects that occur during the charging and discharging phases within the operating cycles.
5) The results obtained in this work during the testing of specimens with different sizes are not statistically enough and more experimentation focused on this subject should be conducted in the future.

The overall lifetime for styrenic DET specimens is in the range of 10^4 cycles under an electric field level of around $100MV/m$, which is only adequate for low-cost disposable systems. Since this type of material is not originally designed for DET application, the dielectric property and material quality might not be a priority during its production. This motivates the limited lifetime measured on this material and leaves significant space for improvement in case cleaner processes are used for its manufacturing. Nonetheless, tests on styrenic DET specimens which consider additional electric field levels and specimen sizes still provide a significant understanding on DET reliability and failure and will be continued in the future works.

The commercial silicone film ELASTOSIL® 2030, which is specifically designed and manufactured for DET applications, exhibited far better performances than the THERABAND YELLOW 11726.

Although the tests on silicone DET specimens are only preliminary and still undergoing, the following observations can already be drawn:

1) Printing quality of the silicone-based electrodes highly affects the lifetime behavior of DET systems. The blade-casting procedure should be improved to avoid ‘bad’ specimens.
2) For good silicone DET specimens, the obtained lifetime is very promising: the characteristic lifetime is about 2.2 million cycles for energy densities larger than $300J/kg$.
3) Locations of breakdown points on silicone DET specimens reflect again the local enhancement at the boundary or irregular area of electrodes.

Though ELASTOSIL® 2030 has shown potential to be utilized in practical DET applications, the manufacture procedure of DET specimens should be significantly improved, especially the printing of compliant electrodes based on the same silicone matrix. The considered improvement methods include electrode-dielectric bonding via low pressure oxygen plasma and electrode deposition via ink-jet printing. Electromechanical characterization on ELASTOSIL® 2030 film should also be conducted to assess its performance against those of other DE materials. An experimental set-up will be developed in future works for lifetime characterization on specimens under both electrical and mechanical loadings, to verify their combined effect as in practical applications. The applied electrical and mechanical loadings will be based on practical working conditions experienced in inflatable DET generators for wave energy harvesting [21].

References

[1] M. Wissler and E. Mazza, “Mechanical behavior of an acrylic elastomer used in dielectric elastomer actuators,” *Sensors and Actuators A: Physical*, vol. 134, no. 2, pp. 494–504, 2007.

[2] F. B. Madsen, A. E. Daugaard, S. Hvilsted, and A. L. Skov, “The Current State of Silicone-Based Dielectric Elastomer Transducers,” *Macromolecular rapid communications*, vol. 37, no. 5, pp. 378–413, 2016.

[3] R. Kaltseis *et al.*, “Natural rubber for sustainable high-power electrical energy generation,” *RSC Advances*, vol. 4, no. 53, pp. 27905–27913, 2014.

[4] M. Giousouf and G. Kovacs, “Dielectric elastomer actuators used for pneumatic valve technology,” *Smart Materials and Structures*, vol. 22, no. 10, p. 104010, 2013.

[5] K. Flittner, M. Schlosser, and H. F. Schlaak, “Dielectric elastomer stack actuators for integrated gas valves,” in *Electroactive Polymer Actuators and Devices (EAPAD) 2011*, 2011, vol. 7976, p. 79761K.

[6] R. Heydt, R. Kornbluh, J. Eckerle, and R. Pelrine, “Sound radiation properties of dielectric elastomer electroactive polymer loudspeakers,” in *Smart Structures and Materials 2006: Electroactive Polymer Actuators and Devices (EAPAD)*, 2006, vol. 6168, p. 61681M.

[7] M. Matysek, P. Lotz, and H. F. Schlaak, “Tactile display with dielectric multilayer elastomer actuators,” in *Electroactive Polymer Actuators and Devices (EAPAD) 2009*, 2009, vol. 7287, p. 72871D.

[8] S. Shian, R. M. Diebold, and D. R. Clarke, “Tunable lenses using transparent dielectric elastomer actuators,” *Opt Express*, vol. 21, no. 7, pp. 8669–8676, Apr. 2013.

[9] F. Carpi, G. Frediani, S. Turco, and D. De Rossi, “Bioinspired tunable lens with muscle-like electroactive elastomers,” *Advanced Functional Materials*, vol. 21, no. 21, pp. 4152–4158, 2011.

[10] H. R. Choi *et al.*, “Soft actuator for robotic applications based on dielectric elastomer: quasi-static analysis,” in *Proceedings 2002 IEEE International Conference on Robotics and Automation (Cat. No.02CH37292)*, Washington, DC, USA, 2002, vol. 3, pp. 3212–3217.

[11] K. Jung, K. J. Kim, and H. R. Choi, “A self-sensing dielectric elastomer actuator,” *Sensors and Actuators A: Physical*, vol. 143, no. 2, pp. 343–351, May 2008.

[12] G. Rizzello, D. Naso, A. York, and S. Seelecke, “A self-sensing approach for dielectric elastomer actuators based on online estimation algorithms,” *IEEE/ASME Transactions on Mechatronics*, vol. 22, no. 2, pp. 728–738, 2017.

[13] T. A. Gisby, B. M. O’Brien, and I. A. Anderson, “Self sensing feedback for dielectric elastomer actuators,” *Applied Physics Letters*, vol. 102, no. 19, p. 193703, 2013.

[14] G. Rizzello, D. Naso, A. York, and S. Seelecke, “Self-sensing in dielectric electro-active polymer actuator using linear-in-parametes online estimation,” in *Mechatronics (ICM), 2015 IEEE Int. Conf*, 2015, pp. 300–306.

[15] R. Pelrine *et al.*, “Dielectric elastomers: generator mode fundamentals and applications,” in *Smart Structures and Materials 2001: Electroactive Polymer Actuators and Devices*, 2001, vol. 4329, pp. 148–157.

[16] P. Brochu, W. Yuan, H. Zhang, and Q. Pei, "Dielectric elastomers for direct wind-to-electricity power generation," in *ASME 2009 Conference on Smart Materials, Adaptive Structures and Intelligent Systems*, 2009, pp. 197–204.

[17] P. Jean *et al.*, "Standing wave tube electro active polymer wave energy converter," in *Electroactive Polymer Actuators and Devices (EAPAD) 2012*, 2012, vol. 8340, p. 83400C.

[18] R. Vertechy, G. P. P. Rosati, and M. Fontana, "Reduced model and application of inflating circular diaphragm dielectric elastomer generators for wave energy harvesting," *Journal of Vibration and Acoustics*, vol. 137, no. 1, p. 011004, 2015.

[19] G. Moretti, M. Fontana, and R. Vertechy, "Parallelogram-shaped dielectric elastomer generators: Analytical model and experimental validation," *Journal of Intelligent Material Systems and Structures*, vol. 26, no. 6, pp. 740–751, 2015.

[20] G. Moretti *et al.*, "Resonant wave energy harvester based on dielectric elastomer generator," *Smart Materials and Structures*, vol. 27, no. 3, p. 035015, 2018.

[21] G. Moretti, M. Righi, R. Vertechy, and M. Fontana, "Fabrication and test of an inflated circular diaphragm dielectric elastomer generator based on pdms rubber composite," *Polymers*, vol. 9, no. 7, p. 283, 2017.

[22] R. Kornbluh, A. Wong-Foy, R. Pelrine, H. Prahlad, and B. McCoy, "Long-lifetime all-polymer artificial muscle transducers," *MRS Online Proceedings Library Archive*, vol. 1271, 2010.

[23] F. Carpi, D. De Rossi, R. Kornbluh, R. E. Pelrine, and P. Sommer-Larsen, *Dielectric elastomers as electromechanical transducers: Fundamentals, materials, devices, models and applications of an emerging electroactive polymer technology*. Elsevier, 2011.

[24] S. J. A. Koh, C. Keplinger, T. Li, S. Bauer, and Z. Suo, "Dielectric elastomer generators: How much energy can be converted?," *IEEE/ASME Transactions on mechatronics*, vol. 16, no. 1, pp. 33–41, 2011.

[25] S. Kawabata, "Fracture and mechanical behavior of rubber-like polymers under finite deformation in biaxial stress field," *Journal of Macromolecular Science, Part B*, vol. 8, no. 3–4, pp. 605–630, 1973.

[26] X. Zhao and Z. Suo, "Theory of dielectric elastomers capable of giant deformation of actuation," *Physical review letters*, vol. 104, no. 17, p. 178302, 2010.

[27] J. Zhu, H. Stoyanov, G. Kofod, and Z. Suo, "Large deformation and electromechanical instability of a dielectric elastomer tube actuator," *Journal of Applied Physics*, vol. 108, no. 7, p. 074113, 2010.

[28] X. Zhao, W. Hong, and Z. Suo, "Electromechanical hysteresis and coexistent states in dielectric elastomers," *Physical review B*, vol. 76, no. 13, p. 134113, 2007.

[29] S. Shian, J. Huang, S. Zhu, and D. R. Clarke, "Optimizing the electrical energy conversion cycle of dielectric elastomer generators," *Advanced Materials*, vol. 26, no. 38, pp. 6617–6621, 2014.

[30] R. Vertechy, M. Fontana, G. R. Papini, and D. Forehand, "In-tank tests of a dielectric elastomer generator for wave energy harvesting," in *Electroactive Polymer Actuators and Devices (EAPAD) 2014*, 2014, vol. 9056, p. 90561G.

[31]R. Pelrine *et al.*, "Dielectric elastomer artificial muscle actuators: toward biomimetic motion," in *Smart Structures and Materials 2002: Electroactive Polymer Actuators and Devices (EAPAD)*, 2002, vol. 4695, pp. 126–138.

[32] G BERSELLI, R VERTECHY, G VASSURA, and V PARENTI CASTELLI, “Design of a single-acting constant-force actuator based on dielectric elastomers,” *JOURNAL OF MECHANISMS AND ROBOTICS*, vol. 1, no. 3, pp. 031007.1-031007.7, 2009.

[33] G. Rizzello, D. Naso, A. York, and S. Seelecke, “Modeling, identification, and control of a dielectric electro-active polymer positioning system,” *IEEE Transactions on Control Systems Technology*, vol. 23, no. 2, pp. 632–643, 2015.

[34]G. Kofod, M. Paajanen, and S. Bauer, “New design concept for dielectric elastomer actuators,” in *Smart Structures and Materials 2006: Electroactive Polymer Actuators and Devices (EAPAD)*, 2006, vol. 6168, p. 61682J.

[35] G. Berselli, R. Vertechy, G. Vassura, and V. Parenti-Castelli, “Optimal synthesis of conically shaped dielectric elastomer linear actuators: Design methodology and experimental validation,” *IEEE/ASME Transactions on Mechatronics*, vol. 16, no. 1, pp. 67–79, 2011.

[36] H. Godaba, J. Li, Y. Wang, and J. Zhu, “A Soft Jellyfish Robot Driven by a Dielectric Elastomer Actuator,” *IEEE Robotics and Automation Letters*, vol. 1, no. 2, pp. 624–631, Jul. 2016.

[37] G. Buchberger, B. Mayrhofer, B. Jakoby, W. Hilber, and S. Bauer, “Dynamic capacitive extensometry setup for in-situ monitoring of dielectric elastomer actuators,” in *Instrumentation and Measurement Technology Conference (I2MTC), 2012 IEEE International*, 2012, pp. 75–80.

[38] M. Matysek, H. Haus, H. Moessinger, D. Brokken, P. Lotz, and H. F. Schlaak, “Combined driving and sensing circuitry for dielectric elastomer actuators in mobile applications,” in *Electroactive Polymer Actuators and Devices (EAPAD) 2011*, 2011, vol. 7976, p. 797612.

[39] B. O’Brien, J. Thode, I. Anderson, E. Calius, E. Haemmerle, and S. Xie, “Integrated extension sensor based on resistance and voltage measurement for a dielectric elastomer,” in *Electroactive Polymer Actuators and Devices (EAPAD) 2007*, 2007, vol. 6524, p. 652415.

[40] S. M. Cadwell, R. A. Merrill, C. M. Sloman, and F. L. Yost, “Dynamic fatigue life of rubber,” *Industrial & Engineering Chemistry Analytical Edition*, vol. 12, no. 1, pp. 19–23, 1940.

[41] G. J. Lake and P. B. Lindley, “The mechanical fatigue limit for rubber,” *Journal of Applied Polymer Science*, vol. 9, no. 4, pp. 1233–1251, 1965.

[42] G. J. Lake, “Mechanical fatigue of rubber,” *Rubber Chemistry and Technology*, vol. 45, no. 1, pp. 309–328, 1972.

[43] W. V. Mars and A. Fatemi, “A literature survey on fatigue analysis approaches for rubber,” *International Journal of fatigue*, vol. 24, no. 9, pp. 949–961, 2002.

[44] W. V. Mars and A. Fatemi, “Factors that affect the fatigue life of rubber: a literature survey,” *Rubber Chemistry and Technology*, vol. 77, no. 3, pp. 391–412, 2004.

[45] L. A. Dissado and J. C. Fothergill, *Electrical degradation and breakdown in polymers*, vol. 9. IET, 1992.

[46] W. B. Nelson, *Accelerated testing: statistical models, test plans, and data analysis*, vol. 344. John Wiley & Sons, 2009.

[47] Yi Chen, Lorenzo Agostini, Marco Fontana, and Rocco Vertechy, “On the Lifetime Performances of Dielectric Elastomer Transducers Under Constant Electric-Stress Loading,” in *paper #a55273*, Vienna, Austria, 2018.

[48] Yi Chen, Lorenzo Agostini, Giacomo Moretti, Marco Fontana, and Rocco Vertechy, “On the lifetime performances of a styrenic rubber membrane for dielectric elastomer transducers,” in *paper #SMASIS2018-8143*, San Antonio, Texas, 2018.

[49] J.-S. Plante and S. Dubowsky, “Large-scale failure modes of dielectric elastomer actuators,” *International journal of solids and structures*, vol. 43, no. 25–26, pp. 7727–7751, 2006.

[50] F. Carpi *et al.*, “Standards for dielectric elastomer transducers,” *Smart Materials and Structures*, vol. 24, no. 10, p. 105025, 2015.

[51] A. Tröls *et al.*, “Stretch dependence of the electrical breakdown strength and dielectric constant of dielectric elastomers,” *Smart Materials and Structures*, vol. 22, no. 10, p. 104012, 2013.

[52] C. Chiang Foo, S. Cai, S. Jin Adrian Koh, S. Bauer, and Z. Suo, “Model of dissipative dielectric elastomers,” *Journal of Applied Physics*, vol. 111, no. 3, p. 034102, Feb. 2012.

[53] T. A. Gisby, S. Q. Xie, E. P. Calius, and I. A. Anderson, “Leakage current as a predictor of failure in dielectric elastomer actuators,” in *Electroactive Polymer Actuators and Devices (EAPAD) 2010*, 2010, vol. 7642, p. 764213.

[54] G. Kofod, P. Sommer-larsen, R. Kornbluh, and R. Pelrine, “Actuation response of polyacrylate dielectric elastomers,” *Journal of Intelligent Material Systems and Structures*, pp. 787–793, 2003.

[55] M. Wissler and E. Mazza, “Electromechanical coupling in dielectric elastomer actuators,” *Sensors and Actuators A: Physical*, vol. 138, no. 2, pp. 384–393, Aug. 2007.

[56] D. E. Woolley, “Edge correction in calculation of dielectric constant,” *Journal of Testing and Evaluation*, vol. 39, no. 2, pp. 140–149, 2010.

[57] R. Vertechy, M. Fontana, G. Stiubianu, and M. Cazacu, “Open-access dielectric elastomer material database,” in *Electroactive Polymer Actuators and Devices (EAPAD) 2014*, 2014, vol. 9056, p. 90561R.

[58] E. Pucci and G. Saccomandi, “A note on the Gent model for rubber-like materials,” *Rubber chemistry and technology*, vol. 75, no. 5, pp. 839–852, 2002.

[59] A. N. Gent, “A New Constitutive Relation for Rubber,” *Rubber Chemistry and Technology*, vol. 69, no. 1, pp. 59–61, Mar. 1996.

[60] T. Beda, “Modeling hyperelastic behavior of rubber: A novel invariant-based and a review of constitutive models,” *Journal of Polymer Science Part B: Polymer Physics*, vol. 45, no. 13, pp. 1713–1732, 2007.

[61] A. N. Gent and A. G. Thomas, “Forms for the stored (strain) energy function for vulcanized rubber,” *Journal of Polymer Science*, vol. 28, no. 118, pp. 625–628, Apr. 1958.

[62] Z. Zhang *et al.*, “New silicone dielectric elastomers with a high dielectric constant,” in *Modeling, Signal Processing, and Control for Smart Structures 2008*, 2008, vol. 6926, p. 692610.

[63] X. Zhang, M. Wissler, B. Jaehne, R. Breonnimann, and G. Kovacs, “Effects of crosslinking, prestrain, and dielectric filler on the electromechanical response of a new silicone and comparison with acrylic elastomer,” in *Smart Structures and Materials 2004: Electroactive Polymer Actuators and Devices (EAPAD)*, 2004, vol. 5385, pp. 78–87.

[64] F. Carpi and D. D. Rossi, “Improvement of electromechanical actuating performances of a silicone dielectric elastomer by dispersion of titanium dioxide powder,” *IEEE Transactions on Dielectrics and Electrical Insulation*, vol. 12, no. 4, pp. 835–843, 2005.

[65] D. Wang, X. Zhang, J.-W. Zha, J. Zhao, Z.-M. Dang, and G.-H. Hu, “Dielectric properties of reduced graphene oxide/polypropylene composites with ultralow percolation threshold,” *Polymer*, vol. 54, no. 7, pp. 1916–1922, 2013.

[66] C. Ramirez, F. M. Figueiredo, P. Miranzo, P. Poza, and M. I. Osendi, “Graphene nanoplatelet/silicon nitride composites with high electrical conductivity,” *Carbon*, vol. 50, no. 10, pp. 3607–3615, 2012.

[67] G. Kofod *et al.*, “Compliant electrodes: solutions, materials and technologies,” *Dielectric Elastomers as Electromechanical Transducers*, pp. 69–76, 2011.

[68] E. T. Thostenson, Z. Ren, and T.-W. Chou, “Advances in the science and technology of carbon nanotubes and their composites: a review,” *Composites science and technology*, vol. 61, no. 13, pp. 1899–1912, 2001.

[69] M. H. Al-Saleh and U. Sundararaj, “A review of vapor grown carbon nanofiber/polymer conductive composites,” *Carbon*, vol. 47, no. 1, pp. 2–22, 2009.

[70] B. Li and W.-H. Zhong, “Review on polymer/graphite nanoplatelet nanocomposites,” *Journal of materials science*, vol. 46, no. 17, pp. 5595–5614, 2011.

[71] S. Rosset and H. R. Shea, “Flexible and stretchable electrodes for dielectric elastomer actuators,” *Applied Physics A*, vol. 110, no. 2, pp. 281–307, 2013.

[72] T. Vu-Cong, C. Jean-Mistral, and A. Sylvestre, “Impact of the nature of the compliant electrodes on the dielectric constant of acrylic and silicone electroactive polymers,” *Smart Materials and Structures*, vol. 21, no. 10, p. 105036, 2012.